DEVELOPMENT OF NOVEL ELECTROLYTE AND ANODE MATERIALS FOR INTERMEDIATE TEMPERATURE SOLID OXIDE FUEL CELL

by

Özge Yaraşan

B.S., Chemistry, Middle East Technical University, 2010

Submitted to the Institute for Graduate Studies in
Science and Engineering in partial fulfillment of
the requirements for the degree of
Master of Science

Graduate Program in Chemistry

Boğaziçi University

2014

To my dad…

Muzaffer Yaraşan

ACKNOWLEDGMENTS

To begin with, I would like to gratefully acknowledge the invaluable supervision of Assist. Prof. Oktay Demircan during this thesis project. It would not be possible to finish this work without his assistance, support and patience. He has been an inspiration for me as a researcher and as a person with an understanding and positive attitude. It was a pleasure to work with him.

I also would like to thank my thesis committee members Assoc. Prof Selmiye Alkan Gürsel and Assis. Prof. Bülent Akgün for sparing their valuable time and reviewing my dissertation.

I wish to thank my laboratory partners; Ayşenur Eslem Kısa for her constant help and support at every part of my project, Can, Aktan and Kübra for bringing fun and so much energy to our lab. I wish to acknowledge the help provided by my so-called lab partners Elif Kılıç İyilik and Aladdin Köksal who supported me when I was alone at the beginning of this project and I really appreciate their goodwill and friendship. Many thanks to the nice friends and staff that I have met in chemistry department and the valuable academicians that inspired me and gave me a different point of view.

I also want to express my gratitude to the people out of this department, my close friends that helped me to get over the hard times and encourged me to go on. I deeply value their companionship.

Lastly, I would like to express my special thanks to my family, especially my father. He is a unique man who raised me up by himself and dedicated his life to me. Without his support and care it wouldn't be possible to get to reach this point. I owe thanks to my sister for her support and guidance througout my life. She has been a role model for me and always encouraged me to continue my studies. Many thanks to my aunts for giving me love and courage. I am grateful to my family for everything they have done..

ABSTRACT

DEVELOPMENT OF NOVEL ELECTROLYTE AND ANODE MATERIALS FOR INTERMEDIATE TEMPERATURE SOLID OXIDE FUEL CELL

Solid oxide fuel cells (SOFC) are energy conversion devices by transforming the chemical energy of fuel into more usable electrical energy at high temperatures. Their higher efficiency and fuel flexibility make them a promising candidate for energy production in various fields. However, the new materials should be developed in order to decrease the material cost and lower the operating temperatures of SOFC systems. SOFC system consists of three main components, an anode, electrolyte and cathode. This study mainly focuses on manufacturing novel electrolyte and anode materials for SOFC. The potential electrolyte material, 20 % Gadolinium doped Ceria (GDC) has higher ionic conductivity compared to conventional electrolyte material 8 % Yttria stabilized Zirconia (YSZ), but GDC has relatively higher electrical conductivity which is undesirable for an electrolyte material. Doping GDC with other metals can improve its properties as an electrolyte or an anode. In this study, Titanium, Vanadium and Manganese is doped to GDC and also Vanadium is doped to Ceria only. According to Four Probe measurements and EIS (Electrochemical Impedance Spectroscopy), 1 % Vanadium doped Ceria has higher ionic and lower electrical conductivity values so that it can be used as an electrolyte for an intermediate temperature SOFC. Additional study was on impregnation of Vanadium and Manganese metals on the anode side of the commercial Nickel-YSZ (Ni-YSZ) anode, YSZ electrolyte, and Lantanum Strontium Manganese (LSM) cathode fuel cells. Power density of the fuel cell increased 25 % after Vanadium impregnation, and the power density increased 145 % increased after Manganese impregnation. Manganese impregnation on the anode side has a significant impact on the performance of a SOFC.

ÖZET

ORTA SICAKLIKTA ÇALIŞAN YAKIT PİLLERİ İÇİN YENİ ELEKTROLİT VE ANOT MALZEMELERİNİN GELİŞTİRİLMESİ

Katı oksit yakıt hücreleri (KOYH) yüksek sıcaklıklarda, yakıtın kimyasal enerjisini daha kullanışlı elektrik enerjisine ceviren, enerji dönüşüm cihazlarıdır. Yüksek verimlilikleri ve kullanılan yakıtların çeşitliliği ile enerji üretimi için gelecek vaat eden bir teknolojidir. Buna rağmen, maliyetli bir teknoloji olmakla beraber, çalışma sıcaklığını düşürmek için yeni materyaller geliştirilmelidir. KOYH sistemleri üç ana parçadan olusur, bunlar anot, elektrolit ve katotdur. Bu çalışmanın odak noktası ise, yeni elektrolit ve anot malzemeleri gelistirilmesi ve üretilmesidir. Geleneksel elektrolit materyali olan %8 Yitriya eklenmiş Zirkonya (YSZ) ile kıyasla, potansiyel elektrolit materyali olan %20 Gadolinyum eklenmiş Seryum oksitin (GDC) daha fazla elektronik iletkenliği vardır. GDC'ye farklı metallerin eklenmesi sayesinde elektrolit ve anot özellikleri geliştirilebilir. Bu çalışmada Titanyum, Vanadyum ve Mangan metalleri GDC'ye eklenmiştir, ayrıca Vanadyum sadece Seryum oksite eklenmiştir. Dört nokta iletkenlik testi ve Elektrokimyasal İmpedans Spektroskopisi (EIS) sonuçlarına göre %1 Vanadyum eklenmiş Seryum oksitin daha yüksek iyonik ve daha düşük elektronik iletkenlik değeri olduğu bulunmuştur. Buna bağlı olarak, orta sıcaklıkta çalışan KOYH için bu maddenin elektrolit olarak kullanılabileceği düşünülmektedir. Bir başka çalışma da Vanadyum ve Mangan metallerinin, ticari Nikel-YSZ (Ni-YSZ) anot, YSZ elektrolit, Lantanum Strontiyum Mangan (LSM) katot disklerinin anot tarafına damlatma yoluyla eklenmesidir. Çıkan sonuçları özetlemek gerekirse, hücreye Vanadyum eklendikten sonra hücrenin performansındaki güç yoğunluğu % 25 oranında artmıştır, Mangan eklendikten sonra da % 145 oranında artış olmıştur. Anot tarafına Mangan eklenmesinin KOYH sisteminin performansına önemli ölçüde etkisi vardır.

TABLE OF CONTENTS

LIST OF FIGURES

LIST OF TABLES

LIST OF ACRONYMS/ABBREVIATIONS

SOFC	Solid Oxide Fuel Cell
PEMFC	Proton Exchange Membrane Fuel Cell
AFC	Alkaline Fuel Cell
DMFC	Direct Methanol Fuel Cell
PAFC	Phosphoric Acid Fuel Cell
MCFC	Molten Carbonate Fuel Cell
GDC	Gadolinium Doped Ceria
YSZ	8% mole Yittria Stabilized Zirconium
30TİGDC	30% mole Titanium Doped Gadolinium-Ceria Oxide
5MnGDC	5% mole Manganese Doped Gadolinium-Ceria Oxide
2VGDC	2% mole Vanadium Doped Gadolinium-Ceria Oxide
1VDC	1% Vanadium Doped Gadolinium-Ceria Oxide
TPB	Triple Phase Boundry
IT-SOFC	Intermediate Temperature Solid Oxide Fuel Cell
LSCM	Lantanum Strontium Chromium Manganese Oxide
LZO	Lantanum Zirconium Oxide
TEC	Thermal Expansion Coefficient
SSC	Samarium Strontium Cobalt Oxide
LSM	Lantanum Strontium Manganese Oxide
LSCF	Lantanum Strontium Cobalt Ferrite Oxide
BSCF	Barium Strontium Cobalt Ferrite Oxide
PSC	Pyridium Strontium Cobalt Oxide
XRD	X-ray diffraction Spectroscopy
IR	Infrared Spectroscopy
SEM	Scanning Electron Microscopy

TEM	Transmission Electron Microscopy
XPS	X-Ray Photoelectron Spectroscopy
EIS	Electrochemical Impedance Spectroscopy
ω	Angular Frequency
ϕ	Phase Difference
V (ω)	Alternating Voltage
j (ω)	Alternating Current
V_m	Direct Voltage
I_m	Direct Current
Z_{im}	Imaginary Impedance
Z_{real}	Real Impedance
R_b	Bulk Resistance
R_p	Polarization Resistance
LSV	Linear Sweep Voltammetry
NiYSZ	Nickel-Yttria Stabilizaed Zirconia
σ	Conductivity
CHR	Chronopotentiometry
O3	3% Oxygen
O10	10% Oxygen
O20	20% Oxygen

1. INTRODUCTION

1.1. Fuel Cell

The living on Earth highly depends on energy sources. Within a century the primary energy sources, coal, oil and natural gas will deplete so there is a huge amount of research on renewable energy sources. Fuel cells are efficient energy conversion devices that use chemical energy to produce electricity. Unlike combustion engines, fuel cells convert electrochemical energy directly into electrical energy and are not limited to Carnot-cycle[1]. As a result of this, the fuel cell efficiency can be up to the theoretical efficiency value of 83% [1]. Various kinds of fuel can be used like natural gas, methanol, hydrogen etc. Depending on the fuel used in the fuel cell, it is environmental friendly technology compared to the other conventional systems.

Fuel cells exhibit much better efficiencies than batteries, at the same time being lighter and having longer lifetimes [2]. Proton exchange membrane (PEM) fuel cells are mostly used for transportation as they require short warming up and cooling down times. Although use of hydrogen is an environmentally friendly technology, using it in vehicles is a long-term process due to its cost to build its infrastructure. From this reason liquid fuels like petrol or methanol will be utilized in shorter term instead of hydrogen. For large-scale applications like power plants, SOFCs offer high efficiency namely %80 which is higher than conventional systems [3]. In addition because of their modularity, fuel cells are available for small scale, stand alone, remote applications. Generally, there is a quest for fuel cells in applications where there is a need for continuous and high quality power supplies. Some examples to these applications are information technology companies, airports, hospitals where there is a tendency to pay higher prices for these systems to save the valuable information with the uninterrupted power supply [3]. Other applications are auxiliary power units (APU) in vehicles, military applications, space applications, electric bicycles, boats, wheelchairs and etc.

1.2. History

The discovery of the fuel cell dates back to 1839 when Sir William Grove demonstrated the reversibility of electrolytic water splitting by building a fuel cell using a liquid electrolyte [4]. Later on in 1899 Nernst discovered the solid oxide electrolyte and presented that certain oxides gained high conductivity by doping with other oxides.

The development accelerated in early 1960s when they were used in American space program called 'Apollo Program'. In the 1980s according to the focus on environmental pollution and the need for higher efficiency in the utilization of fossil fuels, the fuel cell development grew up and reached to a new level. Mainly two types of fuel cells, SOFC and PEM fuel cells are commercialized in recent years and used in various application fields [3]. However there are some obstacles that hinder the fuel cells to achieve a widespread application. These challenges are material cost, durability and fuel storage. Additional research topics are catalytic activity and conductivity of anodes and cathodes and compatibility to each other.

1.3. Types of Fuel Cells

There are mainly six types of fuel cells, which are named after their electrolyte materials [5]. As shown in Table 1.1, these six types of fuel cells are different from each other in terms of working temperature, efficiency, fuel, and application area. The advantages and drawbacks of fuel cell systems are determined by their type and application. The operating temperature has effects on design and efficiency of the fuel cell, the materials used and the type of fuel that may be used. PEMFC, AFC, PAFC are low temperature fuel cells which utilize pure hydrogen as fuel. H^+ or OH^- ions are the dominant ionic current carriers in the cell [2]. MCFC and SOFC operate at higher temperatures so various kinds of fuels can be used like hydrocarbons or alcohol. These fuels need a reforming step to obtain hydrogen from hydrocarbon species [6]. However, high temperatures enable oxidation of hydrocarbons, so the fuels can be utilized directly in case

of MCFC and SOFC [7]. Therefore, the cost of the system decreased dramatically and overall efficiency is increased [7].

Table 1.1. Types of fuel cells.

Low-temperature Fuel Cells				**High-Temperature Fuel Cells**		
	DMFC Direct methanol fuel cell	**PEMFC** Proton exchange fuel cell	**AFC** Alkaline fuel cell	**PAFC** Phosphoric acid fuel cell	**MCFC** Molten carbon fuel cell	**SOFC** Solid oxide fuel cell
Electrolyte	Proton conducting membrane	Proton conducting membrane	Caustic potash solution	Concentrated phosphoric acid	Molten carbonate	Ceramic
Temperature range	<100 ºC	<100 ºC	<100 ºC	~200 ºC	~650 ºC	800 ºC-1000 ºC
Fuel	Methanol	Hydrogen	Hydrogen	Hydrogen	Natural gas, coal	Natural gas, coal
Power ranges	Watts/kilo watts	Watts/kilo watts	Watts/kilo watts	Kilowatts	Kilowatts/megawatts	Kilowatts/megawatts
Application areas	Vehicles, small appliances	Vehicles, small generators, domestic supply	Space	Block type heat and power stations	Power plants, combined heat and power	Power plants, combined heat and power

Although, high operating temperature is advantageous while working with hydrocarbons, it can also cause rapid degradation of the cell materials [8]. Expensive heat-resistant materials should be used and the startup time of the cell will be slower at high temperatures. As a result, reducing the operating temperature is a major research area of solid oxide fuel cells [7-9]. One of the major challenges related with lowering the operating temperature is the significant increase of the electrolyte resistance. In order to reduce the operation temperature, two approaches are widely applied to lower the resistance of dense electrolyte membranes, either by decreasing the traditional YSZ (8 mole% Y_2O_3-ZrO_2) electrolyte thickness or using alternative materials of higher ionic conductivity at lower temperatures [10]. Moreover, usage of a novel electrode material with high performance is equally essential for both strategies.

1.4. Solid Oxide Fuel Cell

Solid oxide fuel cell (SOFC) produces electricity directly by converting the chemical energy of the fuel oxidation to electrical energy. Wide range of fuels can be used due to not only the high working temperature but also the oxidant (O^{2-}) transport via electrolyte material. SOFC has a ceramic electrolyte that carries oxide ions between 600-1000ºC. Researchers aim to develop SOFC's operating at intermediate temperature range (450-700ºC) [5] in order to decrease the input energy, operating costs and start-up time [5]. On the other hand, activation polarization lessens with the effect of high temperature so the cell losses are dominated by internal cell ohmic resistance through the electrolyte, electrodes, and cell interconnects.

1.4.1. Components and Working Mechanism

The cell mainly consists of three components: anode, electrolyte, and cathode. In anode, fuel is oxidized by anode catalyst, and then it combines with oxide ion (O^{-2}) coming from the electrolyte (Equation 1.1).

$$O^{-2} + H_2 \rightarrow H_2O + 2e^- \quad (1.1)$$

In cathode oxygen reduction in air takes place (Equation 1.2).

$$½\ O_2 + 2e^- \rightarrow O^{-2} \quad (1.2)$$

Between anode and cathode there is a thin ceramic electrolyte layer and this layer conducts oxide ions from cathode to anode. The components and working mechanism of the SOFC are demonstrated in Figure 1.1.

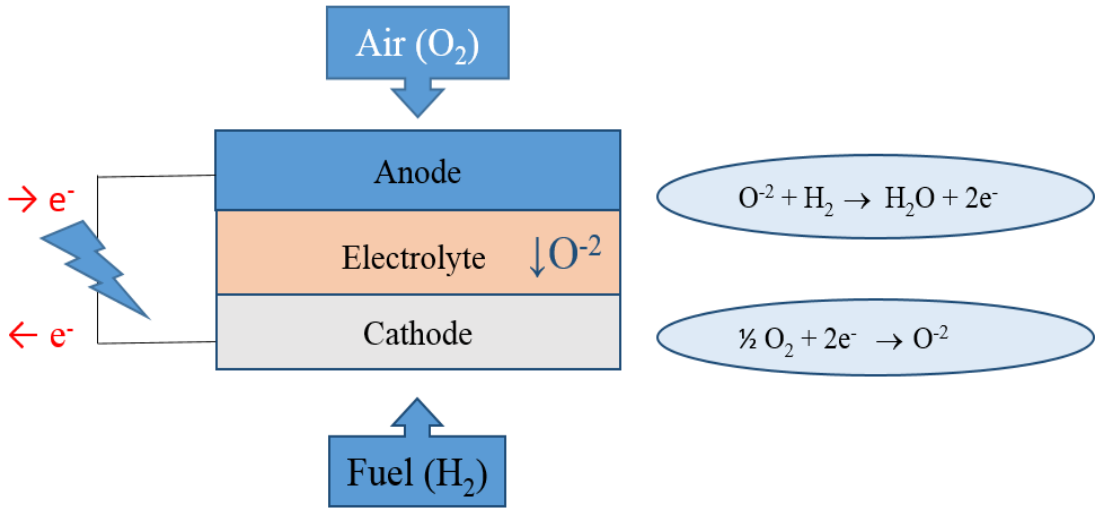

Figure 1.1. Components and working mechanism of fuel cell.

The oxidation reaction at anode occurs at sites named triple phase boundaries (TPB). The electrolyte which carries oxide ions, the anode as an oxidation catalyst and the fuel (gas phase) meet at TPB. As the length of TPB increases, the efficiency of the cell increases. Therefore, the electrolyte and anode material is mixed together with certain amounts in order to increase the TPB length.

1.4.2. Advantages and Disadvantages of SOFC

SOFC have many advantages compared to the conventional energy conversion systems like high efficiency, modularity, flexibility of fuel, noiseless operation and very low levels of SO_x and NO_x emissions [9-11]. Due to their high operation temperature (800–1000 ºC), any kind of hydrocarbon fuels can be used within the cell without an external reformer [11]. However, there are some obstacles that hinder SOFCs entering the energy market due to material issues and fabrication costs [12]. Yet, it is not only an economically competitive technology because of expensive materials, but also the difficulties due to maintaining stability at high temperatures [12]. Ni based conventional anode materials are relatively cheap, but when hydrocarbons are used as fuel, they deposit carbon at their surface which lowers the fuel oxidation, thus, lowers the cell efficiency [13-15]. Sulfur poisoning is a similar problem with the use of hydrocarbons so hydrogen sulfide should be

filtered from the effluent fuel gas [16]. Hydrogen gas does not yield any of these problems and it is an excellent fuel choice for an SOFC, but there are availability, cost and storage problems for hydrogen as fuel. Hydrogen production depends mainly on fossil fuels (coal, natural gas and petroleum), which also yield infrastructure costs [4].

1.4.3. Electrolytes

The electrolyte conducts O^{-2} ions via oxygen deficient sites in the structure. These sites are created by doping a suitable oxide material into the other. An ideal electrolyte should have little or no conduction to prevent current leakage and also should be chemically and mechanically (*e.g.* thermal expansion) compatible with other fuel cell components. The most common and optimized solid electrolyte material used in solid oxide fuel cells is 8 mole % yttria (Y_2O_3) doped zirconia (ZrO_2) called yttria stabilized zirconia (YSZ). Yttria stabilizes the conductive cubic fluorite phase and increases the concentration of oxygen vacancies; therefore the ionic conductivity is enhanced. The conventional YSZ electrolyte material has some drawbacks, such as relatively low ionic conductivity, mismatch of thermal expansion coefficient with electrodes, and the tendency to react with many cathode materials [17].

In recent years, doped ceria electrolytes are accepted as a potential candidate owing to their higher ionic conductivity than that of yttria stabilized zirconia (YSZ) at intermediate temperatures. $Gd_{0.20}Ce_{0.80}O_{2-\partial}$ (GDC) is widely used as electrolyte material [18]. However, among all the dopants for ceria, Samaria is known to provide the highest conductivity enhancement, especially the high ionic conductivity at intermediate temperatures [19].

Another electrolyte material is lanthanum strontium gallium magnesium oxide (LSGM) [20]. In addition, bismuth oxide-based materials and metal doped bismuth vanadium oxides have high ionic conductivities at low temperatures but suffer from high chemical reactivity, low mechanical strength and instability in reducing environments. The materials with the general formula of $Ln_{10}Si_6O_{27}$ where Ln is a rare earth metal are also potential electrolyte candidate, although the high reactivity of silicates could be a potential problem.

1.4.4. Anodes

SOFC anode material should be electrically conductive, porous and should possess high catalytic activity toward fuel oxidation reaction. The anode is often the layer that provides the mechanical support to the cell. The conventional anode material is Nickel-YSZ cermet [21]. Ni acts as both catalyst and conductor, while YSZ offers the oxygen ion conductivity, increases the length of TPB and adjusts the coefficient of thermal expansion (CTE). NiYSZ anodes show high electrochemical performance in H_2 as fuel. On the other hand, they suffer from carbon deposition and sulfur poisoning in hydrocarbon fuels and Ni particles agglomerate [15]. As carbon deposition on Ni lowers the anode performance, some alternatives have been offered to overcome this issue such as using excess steam in the fuel stream, using copper instead of nickel in the cermet and the development of novel anode materials [22].

Ceria (CeO_2) is a mixed ionic/ conductive material; therefore, it is suitable as an anode material [23]. Ceria is accepted as the redox couple of Ce^{+3}/Ce^{+4} which results in morphological changes and adds electrically conductivity. The use of ceria often prevents carbon deposition and promotes hydrocarbon oxidation [19]. At the same time, ceria-based anodes without any metallic component display quite a poor performance; even when current collectors of Au ink and Pt paste are used [24]. Gadolinium-doped ceria (GDC) has become popular in recent years owing to its high ionic conductivity at intermediate temperatures [25].

Materials such as Cu/CeO_2-YSZ are developed to avoid carbon deposition, since Cu has low catalytic activity for coke formation [26]. However, their performance and thermal stability is low because of low melting point of copper thus alloys of Cu are tested. Cu-Ni alloys showed remarkable properties for direct utilization of methane in SOFC [27].

Cu-Co based anodes showed an improved performance in H_2 and butane (n-C_4H_{10}) at 800ºC [28]. The anodes based on Cu-Fe/CeO_2-YSZ are prepared by wet impregnation method has good catalytic activity in H_2 and n-C_4H_{10} fuels [29].

Lanthanum based anodes such as $(La_{0.75}\ Sr_{0.25})Cr_{0.5}Mn_{0.5}O_3$ (LSCM) are another group of anode materials which are stable, resistant to coking and has suitable CTE, but the conductivity and catalytic activity is low for efficient use as an SOFC anode material at intermediate temperatures [30].

1.4.5. Cathodes

An ideal SOFC cathode should have conductivity both ionically and electrically, high catalytic activity for oxygen reduction, close thermal expansion coefficient (CTE) with other materials, chemical compatibility with other materials and be stable at SOFC temperature range. Perovskite materials have been widely used as cathode materials in SOFCs [31]. The conventional cathode material is a composite of Sr-doped $LaMnO_3$ (LSM) and yttria-stabilized zirconia (YSZ). A disadvantage of this material is that it reacts with YSZ at high temperatures and forms $La_2Zr_2O_7$ (LZO) layer so sintering temperature should be adjusted [32]. A widely studied cathode material is strontium and cobalt doped lanthanum ferrate, $La_{0.8}Sr_{0.2}Fe_{0.8}Co_{0.2}O_{3-\partial}$ (LSCF), which displays high ionic conductivity as cobalt based cathode material [33]. Another choice of cathode material is samarium strontium cobaltate; $Sm_{0.5}Sr_{0.5}CoO_3$ (SSC) [34]. $Ba_{0.5}Sr_{0.5}Co_{0.8}Fe_{0.2}O_{3-\partial}$ (BSCF) is an alternative cathode material for intermediate temperature range [35]. Compared to LSCF-based and SSC-based cathodes, the cell with a BSCF cathode exhibits a much lower interfacial polarization resistance at low temperatures [36]. Another material is $Pr_{0.7}Sr_{0.3}CoO_{3-\delta}$ (PSC) that is a promising cathode material candidate for IT-SOFC applications due to its high electrical conductivity and power density [37].

1.5. Material Characterization

1.5.1. X-Ray Diffraction (XRD)

X-ray diffraction is an analytical technique, which can give information about the Bragg reflections related with the crystal structure. A crystal structure is built of layers which resembles to a semi-transparent mirror. X-rays with a certain wavelength can be

reflected between these planes such that the angle of reflection is equal to the angle of incidence. This behavior is called ‘diffraction’ and it is described by Bragg’s Law (Equation 1.3)

$$2d\sin\theta = n\lambda \quad (1.3)$$

When Bragg’s Law is satisfied, constructive interference of diffracted X-ray beams occur and a ‘Bragg reflection’ will be caught by a detector scanning at this angle. The inter-layer spacing of atoms in the crystal structure is determined by the positions of these reflections. Peak intensities give information about the amount of X-ray scattering that contribute to that reflection. Analysis of the diffraction pattern allows the identification of phases within a given sample, thus it provides information about the crystallinity of a sample.

1.5.2. Raman Spectroscopy

Raman spectroscopy is a spectroscopic technique used to provide information about vibrational, rotational, and other low-frequency modes in a system. The technique involves shining a monochromatic light source (i.e. laser) on a sample and detecting the scattered light like inelastic scattering, or Raman scattering. The laser light interacts with molecular vibrations, phonons or other excitations in the system, at the end the energy of the laser photons are shifted up or down. The shift in energy gives information about the vibrational modes in the system that can be used for sample identification. A similar technique is infrared (IR) spectroscopy, which gives complementary information about the samples. The main difference between Raman and IR spectroscopy is that Raman has a dispersive working principle whereas IR has a transmissive working principle. The blackbody radiation interacts with the detector of IR at high temperature range so it is not possible to use IR for SOFC applications.

1.5.3. Scanning Electron Microscopy (SEM)

The scanning electron microscope (SEM) is a microscopy technique that uses a focused beam of accelerated high-energy electrons to generate a variety of signals at the surface of solid specimens. The electron beam is focused in a fine probe and scanned with the help of scanning coils across the surface of the sample. Electromagnetic radiation is emitted by every scanned point and selected parts of the radiation (like secondary or backscattered electrons) are collected by the detector. The signals resulting from electron-sample interactions reveal information about the sample including external morphology (texture), chemical composition, and crystalline structure of materials making up the sample. In most applications, data are collected over a selected area of the surface of the sample, and a 2-dimensional image is generated. Resolution which is better than 1 nanometer can be achieved by SEM.

1.5.4. Transmission Electron Microscopy (TEM)

Transmission electron microscopy (TEM) is a microscopy technique in which a high voltage beam of electrons are emitted by a cathode and then focused by electromagnetic lenses into a very thin beam. The electron beam transmits through the specimen that is going to be studied. An image is formed from the interaction of the electrons transmitted through the specimen. The resulting image is magnified and focused onto an imaging device, such as a fluorescent screen, on a layer of photographic film, or to be detected by a sensor such as a CCD camera.

Transmission electron microscopes produce two-dimensional, black and white images. They are capable of imaging at a significantly higher resolution than light microscopes, due to the small de Broglie wavelength of electrons. This enables the instrument's user to observe fine detail which is thousands of times smaller than the smallest resolvable object in a light microscope.

1.5.5. X-Ray Photoelectron Spectroscopy (XPS)

X-ray photoelectron spectroscopy (XPS) is a surface-sensitive quantitative spectroscopic technique that gives information about the elemental composition, empirical formula, chemical state and electronic state of the elements that exist within a material. XPS spectra are obtained by irradiating a material with a beam of X-rays while simultaneously measuring the kinetic energy and number of photoelectrons that are emitted. The binding energies of the electrons can be calculated from their kinetic energies. The calculation of the kinetic energies by photoelectric effect is shown in Equation 1.4.

$$KE = h\nu - BE - Q_s \quad (1.4)$$

Where *hv* is the energy of the photon, BE is the binding energy of the atomic orbital from which the electron originates, and Q_s is the spectrometer work function. From the binding energy and intensity of a photoelectron peak, the elemental identity, chemical state, and quantity of an element are determined. Samples are kept in high vacuum conditions, however a new area of development is ambient-pressure XPS, in which samples are analyzed at pressures of a few tens of millibar.

1.5.6. Electrochemical Techniques

1.5.6.1. Electrochemical Impedance Spectroscopy (EIS). Electrochemical impedance is defined as the response of an electrochemical system (cell) to an applied potential. An AC potential is applied to the electrochemical cell at constant overpotential and then the resulting current is measured through the cell. An alternating voltage, ΔV (ω), is imposed at constant overpotential of the cell and the response is measured in terms of an alternating current, Δj (ω) as shown in Equation 1.5 and Equation 1.6.

$$\Delta V(\omega, t) = V_m \cdot e^{-i\omega t} \quad (1.5)$$

$$\Delta j(\omega, t) = I_m \cdot e^{-i(\omega t + \phi)} \quad (1.6)$$

In the equations above, t is the time, V_m and I_m are the magnitudes for voltage and current respectively, ω is the angular frequency, and ϕ is the phase difference between the voltage and the current. The impedance, Z, is defined as;

$$Z(\omega) = \Delta V(\omega, t) / \Delta j(\omega, t) = (V_m / I_m) \, . \, e^{i\phi} \tag{1.7}$$

By using the Euler equation (Equation 1.8),

$$e^{i\phi} = \cos\phi + i \sin\phi \tag{1.8}$$

The impedance would be:

$$Z(\omega) = Z_{re}(\omega) + Z_{im}(\omega) \tag{1.9}$$

In which,

$$Z_{re}(\omega) = \text{real}\,(Z) = |Z| \, . \cos\phi \tag{1.10}$$

$$Z_{im}(\omega) = \text{imag}\,(Z) = |Z| \, . \sin\phi \tag{1.11}$$

$$|Z| = V_m / I_m = (Z_{re2} + Z_{im2})^{1/2} \tag{1.12}$$

$$\tan\phi = Z_{im}(\omega) / Z_{re}(\omega) \tag{1.13}$$

There are several ways to plot an EIS graph, one of them is Nyquist plot (Figure 1.2). y-axis is Z_{im} which is the capacitance while x-axis is Z_{real} which is the resistance of the system.

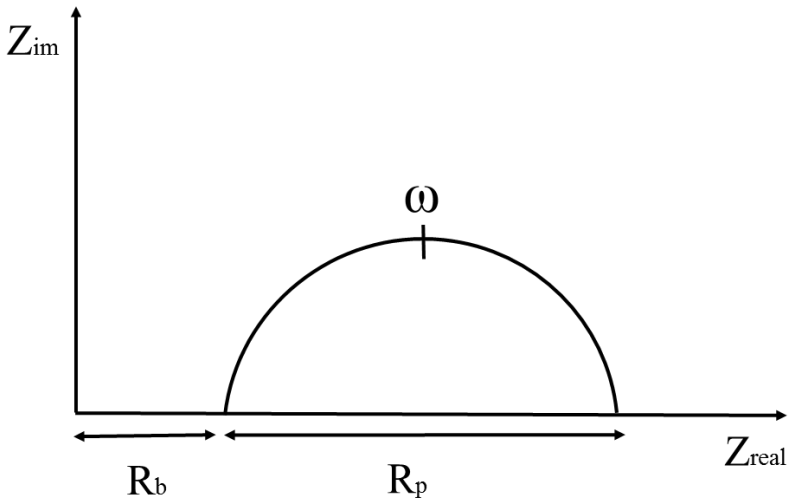

Figure 1.2. EIS graph.

Generally, left side of the graph is the high frequency part in which charge transfer reactions dominate. Right side of the graph is the low frequency part in which the chemical reactions dominate. Bulk resistance, R_b is the ohmic resistance, which is mainly the electrolyte resistance and is present at high frequency domain of the impedance spectroscopy. Polarization resistance, R_p involves the resistance derived from chemical reactions at the electrodes of the cell and is related with the overpotential losses. The point at the maximum imaginary impedance value is called relaxation frequency (ω) which reveals information about the rate of the reactions taking place. Several arcs can be present in a Nyquist plot, which indicates that there are more than one relaxation frequencies and different chemical processes. An efficient working cell should have low values of $\mathbf{R_b}$ and R_p which means that the resistances caused by electrolytes and electrodes are minimum.

1.5.6.2. Linear sweep voltammetry (LSV). There are some parameters in an electrochemical system that lowers an operating cell efficiency; these parameters are called polarizations. Polarization is a voltage loss or overpotential, which hinders the electrochemical processes in a cell. There are three types of polarizations, ohmic polarization, concentration polarization, and activation polarization. The ohmic contribution derives from resistance to electron and ion flows in the materials, and is generally dominated by the electrolyte resistance. Concentration polarization is caused by the resistance to mass transport through the electrodes and interfaces and is generally largest at the cathode. Activation polarization is the voltage drop due to slowest rate determining step of the reactions. In order to investigate the polarization characteristic of the working electrode, a certain potential that is called overpotential is applied between the working and the reference electrode.

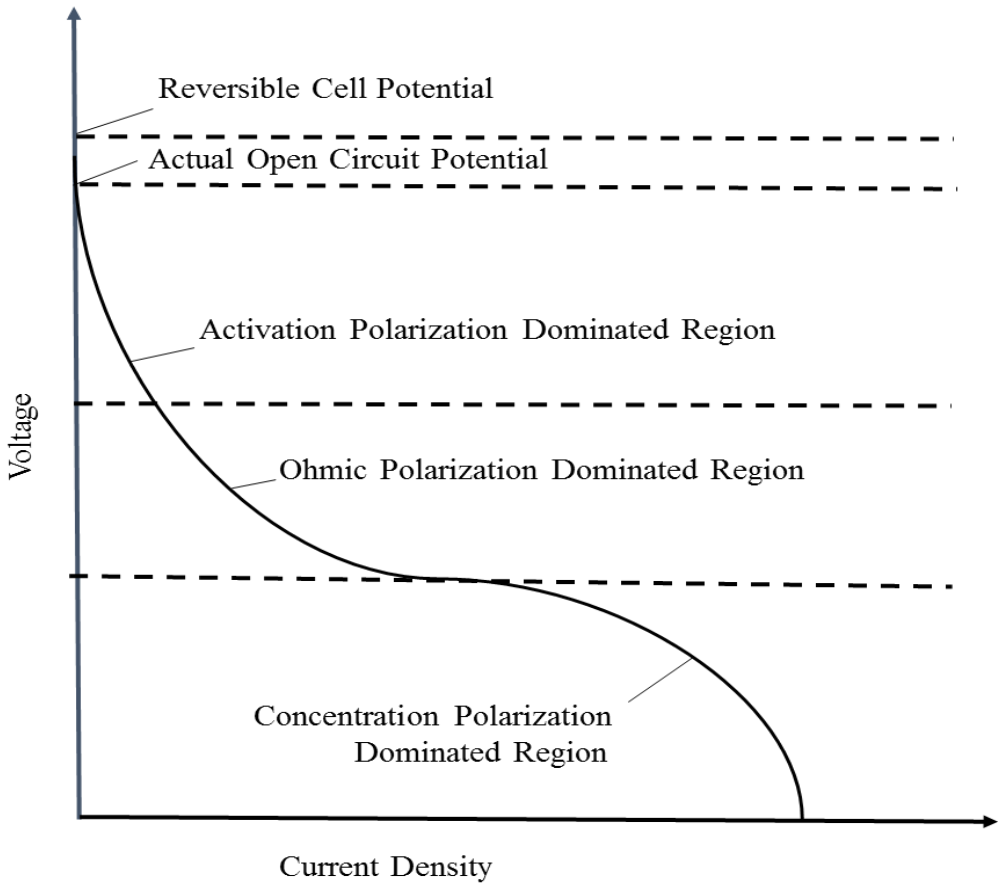

Figure 1.3**.** Polarization curve for a fuel cell with regions dominated by various kinds of losses.

A positive potential indicates an anodic overpotential, while a negative potential indicates a cathodic overpotential. In situ characterization of a fuel cell can be achieved by measurement of current and voltage of the cell. Linear sweep voltammetry and electrochemical impedance spectroscopy are the two techniques that are used for cell characterization.

Linear sweep voltammetry is a voltammetric method where the current at a working electrode is measured as the potential between the working electrode and a reference electrode is altered in time. In LSV measurements the current response is plotted as a function of voltage rather than time.

The resistance is calculated from the slope of the line at certain ranges.

$$R=V/I \tag{1.14}$$

The power density can be calculated by the multiplication of current and the voltage values.

$$P=I \times V \tag{1.15}$$

Linear sweep voltammetry is affected by the rate of electron transfer reactions, the chemical reactivity of the species and the voltage scan rate.

1.5.6.3 Chronopotentiometry. In this technique, constant current is applied to the working electrode and electrical conductivity of the species is calculated and the activation energies for electrical conductivity is measured. By using ohm equation (Equation 1.16), resistance of the system can be found. The resistance is equal to the multiplication of electrical resistivity and the length between the wires where the current is applied, divided by area (Equation 1.17). The conductivity is the reciprocal of the resistivity and therefore depends on the length between the wires, resistance of the system and area (Equation 1.18, 1.19) When the conductivity value is placed in Arrhenius equation (Equation 1.20) and arranged by dividing with temperature and taking the logarithm of both sides (Equation 1.21.), the resulting equation (Equation 1.22) is used for plotting the voltage vs time graph (Figure 1.4.) From the slope of the line. the activation energy of the samples can be calculated.

$$R=V/I \quad (1.16)$$

$$R=\rho L/A \quad (1.17)$$

$$\sigma=1/\rho \quad (1.18)$$

$$\sigma= 1/R \times L/A \quad (1.19)$$

$$\sigma \times T = \sigma_o \times e^{(-E_a/k_B T)} \quad (1.20)$$

$$\sigma = \sigma_o/T \times e^{(-E_a/k_B T)} \quad (1.21)$$

$$\log \sigma = \log \sigma_o/T - E_a/k_B T \quad (1.22)$$

where R is the resistance of the system, V is the voltage, I is the current, ρ is the resistivity, σ is the conductivity, k_B is Boltzman constant, L is length between two wires and A is the area (width of the bar x thickness of the bar)

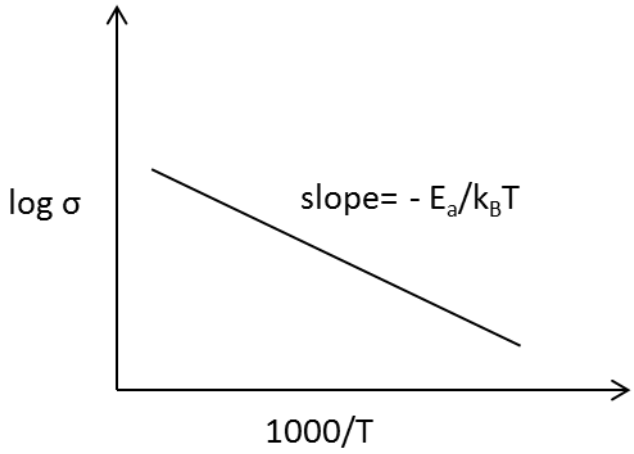

Figure 1.4. Arrhenius plot.

1.6. Aim of the Study

The aim of this study is to develop novel electrolyte and anode materials for a better SOFC operating at intermediate temperature range (400-600°C). Sol-gel method is used to synthesize different metal oxides by doping different metals (Manganese, Titanium and Vanadium) to % 20 Gadolinium doped Ceria (GDC). These materials are optimized by doping them with different metals and proportions. The reason why GDC is selected for synthesis is its properties as a mixed conductor, i.e. both electrically and ionically. Therefore, GDC is a suitable material for anode and electrolyte layers of a fuel cell.

An ideal electrolyte has a negligible electric conductivity, however, the redox couple Ce^{+3}/Ce^{+4} increases the electric conductivity of Ceria. If electric conductivity of GDC is decreased when doped with other metals, then it can be a better electrolyte material. Another parameter for an ideal electrolyte is its ionic conductivity. This property is investigated by electrochemical analysis for the doped Ceria based materials. In the light of these results, the synthesized materials can be used either as an electrolyte or an anode material for SOFC systems. Novel cathode materials are being developed at the same time in another project. The effect of the impregnation of Vanadium and Manganese metals to

the commercial SOFC operating at 800ºC is also investigated to address the questions about poisoning on NiYSZ anodes.

The effect of the impregnation on the performance of the cell is measured by electrochemical impedance spectroscopy (EIS) and linear sweep voltammetry (LSV), detecting the resistance and current of the system respectively. Better SOFCs operating with higher power densities can be achieved with this simple method.

Hence, the aim of this project is to manufacture a novel SOFC system operating at intermediate temperature range by developing new electrolyte and anode materials.

2. EXPERIMENTAL

2.1. Synthesis Methods and Materials

The chemicals that are used in sol gel synthesis and the binders are ordered from the manufacturers Alfa Aesar and Sigma Aldrich. The commercial solid oxide fuel cells and LSM-YSZ composite cathode paste is obtained from the company Fuel Cell Materials. The anode supported cells were 20mm in diameter with the Ni-YSZ anode, YSZ electrolyte and LSM cathode. The electrolyte thickness of the cell is 10 micrometer. The golden wires used in the electrodes are 0.25mm in diameter and are obtained from Alfa Aesar. The golden conductor paste is received from the company Heraeus.

2.2. Instrumentation

Electrochemical Impedance Spectroscopy (EIS) and electrochemical performance test are carried out by GAMRY Referance 600 Potentiostat/Galvanostat instrument. X-Ray Diffraction(XRD) analysis are conducted with Rigaku D/MAX-Ultima+/PC X-ray Diffraction instrument at Boğaziçi University Advanced Technologies Research and Development Center. Raman Spectroscopy is used to analyze the samples used as fuel cell materials and the measurements are done with Renishaw InVia Raman Microscope with 532 nm laser at Boğaziçi University Advanced Technologies Research and Development Center.

2.3 Synthesis of SOFC anode and electrolyte materials

The synthesis procedure for anode and electrolyte materials is citrate nitrate auto-combustion, also called sol-gel method. Generally, the nitrates of the metals are dissolved in distilled water in separate beakers and then mixed together. Citric acid is added as a

complexant with 2/1 mole ratio and ethylene glycol is added for homogenous gel formation. The overall solution is immersed in oil bath at 80 C^o and evaporated until all the water is gone with continuous stirring. A sticky gel is obtained as a product and the gel is transferred to a high temperature crucible to be ignited at 900 C^o for 2 hours after gradual heating. The resulting powder is characterized by using XRD.

Different metals are added to Gadolinium doped Ceria (GDC) like Vanadium, Titanium and Manganese. These metals are added at different ratios to GDC and replaced with Cerium proportionally. It is assumed that the oxide conductivity of the doped GDC will be improved by this method, therefore better electrolyte materials will be obtained for SOFC operations.

The metals are doped with different proportions:

- Manganese is doped with % 0,5, 1, 2, 3, 4, 5, 10, 15, 20, 25, 30, 50 mole proportions to GDC. The product is Manganese doped Gadolinium-Cerium oxide (MnGDC).

- Titanium is doped with % 0.5, 1, 2, 3, 4, 5, 10, 15, 20, 25, 30, 40, 50 mole proportions to GDC. The product is Titanium doped Gadolinium-Cerium oxide (TiGDC).

- Vanadium is doped with % 1, 2, 3, 4, 5, 10 mole proportions to GDC. The product is Vanadium doped Gadolinium-Cerium oxide (VGDC).

- Vanadium is doped with %1, 2, 3, 4 mole proportions to Ceria. The product is Vanadium doped Ceria (VDC).

After synthesis the products are sintered, meaning that they are heated gradually to a certain temperature to get rid of the side products and form the perovskite structure. VDC, VGDC and TiGDC is sintered according to Figure 2.1. First the samples are heated up to 400°C with the rate of 1°C/min and dwell time is 1 hour, then they are heated up to 700°C

with the rate of 0.3°C/min and dwell time is 1 hour. After this step, the samples are heated to 900°C with the rate of 0.5°C, dwell time is 2 hours and finally cooled to room temperature with the rate of 1°C.

MnGDC is sintered according to Figure 2.2. First the samples are heated up to 400°C with the rate of 0.5°C/min and dwell time is 1 hour, then they are heated up to 700°C with the rate of 0.5°C/min and dwell time is 1 hour. After this step, the samples are heated to 900°C with the rate of 1°C, dwell time is 2 hours and finally cooled to room temperature with the rate of 1°C.

As can be seen, VDC, VGDC and TiGDC sintering is slower than MnGDC sintering. The reason is that the starting materials Vanadium (III) acetyl acetonate ($V(C_5H_7O_2)_3$) and Potassium bis (oxalato) oxotitanate (IV) dihydrate (K_2 ($TiO(C_2O_4)_2$).$2H_2O$) contain carbon oxides so they should be evolved at a slower rate during sintering.

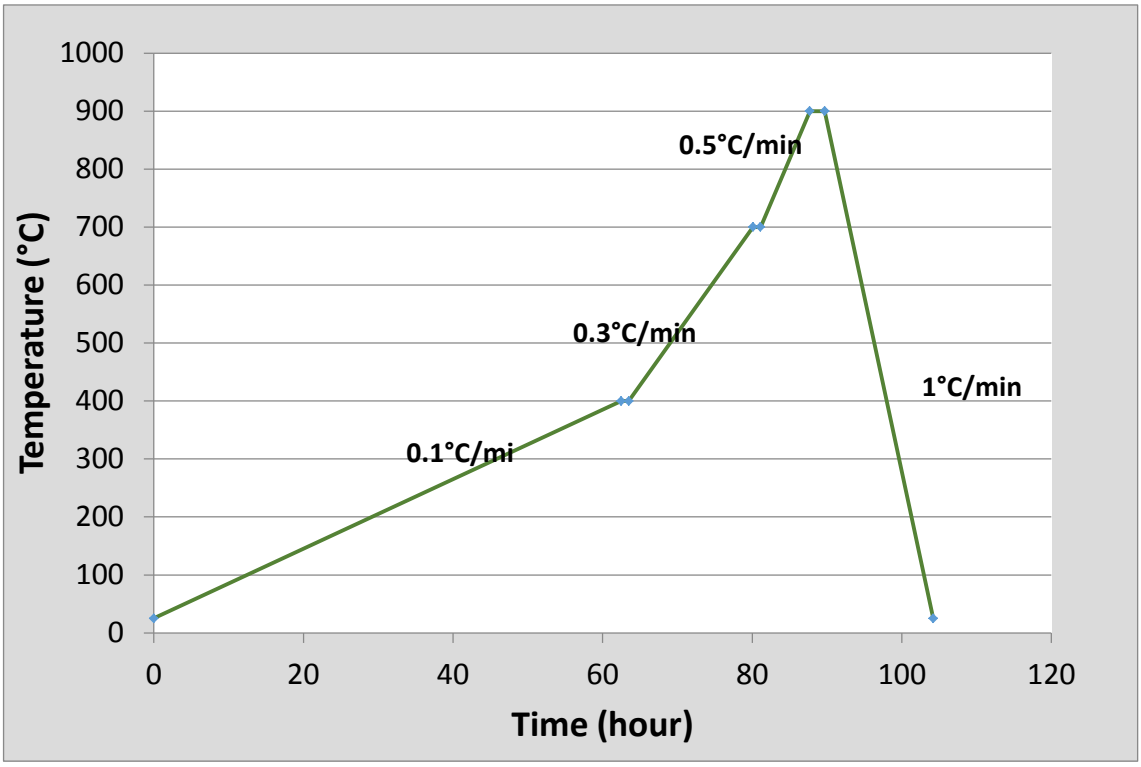

Figure 2.1. VDC, VGDC, TiGDC sintering graph.

0.5 gr 1 % (mole) Vanadium doped Gadolinium-Cerium oxide (1VGDC) synthesis: 1.239 gr ($2.26x10^{-3}$ mole) Cerium (IV) ammonium nitrate ($(NH_4)_2Ce(NO_3)_6$), 0.259 gr ($5.75x10^{-4}$ mole) Gadolinium (III) nitrate six hydrate ($Gd(NO_3)_3.6H_2O$), 0.010 gr ($2.86x10^{-5}$ mole) Vanadium (III) acetyl acetonate ($V(C_5H_7O_2)_3$) and 1.202 gr ($5.72x10^{-3}$ mole) citric acid ($C_6H_8O_7.H_2O$) is dissolved in 20 ml distilled water. Then 1.0 mL ($1.74x10^{-2}$ mole) ethylene glycol ($C_2H_6O_2$) is added and all the water is evaporated inside the oil bath at 80ºC. A gel is formed and it is transferred to a high temperature crucible and sintered. The resulting powders are characterized by XRD.

0.5 gr 2 % (mole) Vanadium doped Gadolinium-Cerium oxide (2VGDC) synthesis: 1.230 gr ($2.24x10^{-3}$ mole) Cerium (IV) ammonium nitrate ($(NH_4)_2Ce(NO_3)_6$), 0.258 gr ($5.72x10^{-4}$ mole) Gadolinium (III) nitrate six hydrate ($Gd(NO_3)_3.6H_2O$), 0.020 gr ($2.86x10^{-5}$ mole) Vanadium (III) acetyl acetonate ($V(C_5H_7O_2)_3$) and 1.215 gr ($5.78x10^{-3}$ mole) citric acid ($C_6H_8O_7.H_2O$) is dissolved in 20 ml distilled water. Then 1.0 mL ($1.74x10^{-2}$ mole) ethylene glycol ($C_2H_6O_2$) is added and all the water is evaporated inside the oil bath at 80ºC. A gel is formed and it is transferred to a high temperature crucible and sintered. The resulting powders are characterized by XRD.

0.5 gr 3 % (mole) Vanadium doped Gadolinium-Cerium oxide (3VGDC) synthesis: 1.221 gr ($2.22x10^{-3}$ mole) Cerium (IV) ammonium nitrate ($(NH_4)_2Ce(NO_3)_6$), 0.261 gr ($5.78x10^{-4}$ mole) Gadolinium (III) nitrate six hydrate ($Gd(NO_3)_3.6H_2O$), 0.030 gr ($8.68x10^{-5}$ mole) Vanadium (III) acetyl acetonate ($V(C_5H_7O_2)_3$) and 1.209 gr ($5.75x10^{-3}$ mole) citric acid ($C_6H_8O_7.H_2O$) is dissolved in 20 ml distilled water. Then 1.0 mL ($1.74x10^{-2}$ mole) ethylene glycol ($C_2H_6O_2$) is added and all the water is evaporated inside the oil bath at 80ºC. A gel is formed and it is transferred to a high temperature crucible and sintered. The resulting powders are characterized by XRD.

0.5 gr 4 % (mole) Vanadium doped Gadolinium-Cerium oxide (4VGDC) synthesis: 1.211 gr ($2.21x10^{-3}$ mole) Cerium (IV) ammonium nitrate ($(NH_4)_2Ce(NO_3)_6$), 0.262 gr ($5.81x10^{-4}$ mole) Gadolinium (III) nitrate six hydrate ($Gd(NO_3)_3.6H_2O$), 0.040 gr ($1.16x10^{-4}$ mole) Vanadium (III) acetyl acetonate ($V(C_5H_7O_2)_3$) and 1.221 gr ($5.81x10^{-3}$ mole) citric acid

($C_6H_8O_7.H_2O$) is dissolved in 20 ml distilled water. Then 1.0 mL ($1.74x10^{-2}$ mole) ethylene glycol ($C_2H_6O_2$) is added and all the water is evaporated inside the oil bath at 80ºC. A gel is formed and it is transferred to a high temperature crucible and sintered. The resulting powders are characterized by XRD.

0.5 gr 5 % (mole) Vanadium doped Gadolinium-Cerium oxide (5VGDC) synthesis: 1.201 gr ($2.19x10^{-3}$ mole) Cerium (IV) ammonium nitrate ($(NH_4)_2Ce(NO_3)_6$), 0.263 gr ($5.84x10^{-4}$ mole) Gadolinium (III) nitrate six hydrate ($Gd(NO_3)_3.6H_2O$), 0.050 gr ($1.46x10^{-4}$ mole) Vanadium (III) acetyl acetonate ($V(C_5H_7O_2)_3$) and 1.228 gr ($5.84x10^{-3}$ mole) citric acid ($C_6H_8O_7.H_2O$) is dissolved in 20 ml distilled water. Then 1.0 mL ($1.74x10^{-2}$ mole) ethylene glycol ($C_2H_6O_2$) is added and all the water is evaporated inside the oil bath at 80ºC. A gel is formed and it is transferred to a high temperature crucible and sintered. The resulting powders are characterized by XRD.

0.5 gr 10 % (mole) Vanadium doped Gadolinium-Cerium oxide (10VGDC) synthesis: 1.151 gr ($2.10x10^{-3}$ mole) Cerium (IV) ammonium nitrate ($(NH_4)_2Ce(NO_3)_6$), 0.271 gr ($6.05x10^{-4}$ mole) Gadolinium (III) nitrate six hydrate ($Gd(NO_3)_3.6H_2O$), 0.104 gr ($3.06x10^{-4}$ mole) Vanadium (III) acetyl acetonate ($V(C_5H_7O_2)_3$) and 1.260 gr ($6.14x10^{-3}$ mole) citric acid ($C_6H_8O_7.H_2O$) is dissolved in 20 ml distilled water. Then 1.0 mL ($1.74x10^{-2}$ mole) ethylene glycol ($C_2H_6O_2$) is added and all the water is evaporated inside the oil bath at 80ºC. A gel is formed and it is transferred to a high temperature crucible and sintered. The resulting powders are characterized by XRD.

0.5 gr 1 % (mole) Vanadium doped Cerium oxide (1VDC) synthesis: 1.584 gr ($2.92x10^{-3}$ mole) Cerium (IV) ammonium nitrate ($(NH_4)_2Ce(NO_3)_6$), 0.010 gr ($2.92x10^{-5}$ mole) Vanadium (III) acetyl acetonate ($V(C_5H_7O_2)_3$) and 1.226 gr ($5.84x10^{-3}$ mole) citric acid ($C_6H_8O_7.H_2O$) is dissolved in 15 ml distilled water. Then 1.0 mL ($1.74x10^{-2}$ mole) ethylene glycol ($C_2H_6O_2$) is added and all the water is evaporated inside the oil bath at 80ºC. A gel is formed and it is transferred to a high temperature crucible and sintered. The resulting powders are characterized by XRD.

0.5 gr 2 % (mole) Vanadium doped Cerium oxide (2VDC) synthesis: 1.576 gr ($2.88x10^{-3}$ mole) Cerium (IV) ammonium nitrate ($(NH_4)_2Ce(NO_3)_6$), 0.020 gr ($5.84x10^{-5}$ mole) Vanadium (III) acetyl acetonate ($V(C_5H_7O_2)_3$) and 1.232 gr ($5.88x10^{-3}$ mole) citric acid ($C_6H_8O_7.H_2O$) is dissolved in 15 ml distilled water. Then 1.0 mL ($1.74x10^{-2}$ mole) ethylene glycol ($C_2H_6O_2$) is added and all the water is evaporated inside the oil bath at 80ºC. A gel is formed and it is transferred to a high temperature crucible and sintered. The resulting powders are characterized by XRD.

0.5 gr 3 % (mole) Vanadium doped Cerium oxide (3VDC) synthesis: 1.569 gr ($2.86x10^{-3}$ mole) Cerium (IV) ammonium nitrate ($(NH_4)_2Ce(NO_3)_6$), 0.030 gr ($8.85x10^{-5}$ mole) Vanadium (III) acetyl acetonate ($V(C_5H_7O_2)_3$) and 1.240 gr ($5.90x10^{-3}$ mole) citric acid ($C_6H_8O_7.H_2O$) is dissolved in 15 ml distilled water. Then 1.0 mL ($1.74x10^{-2}$ mole) ethylene glycol ($C_2H_6O_2$) is added and all the water is evaporated inside the oil bath at 80ºC. A gel is formed and it is transferred to a high temperature crucible and sintered. The resulting powders are characterized by XRD.

0.5 gr 4 % (mole) Vanadium doped Cerium oxide (4VDC) synthesis: 1.560 gr ($2.84x10^{-3}$ mole) Cerium (IV) ammonium nitrate ($(NH_4)_2Ce(NO_3)_6$), 0.040 gr ($2.92x10^{-5}$ mole) Vanadium (III) acetyl acetonate ($V(C_5H_7O_2)_3$) and 1.246 gr ($5.93x10^{-3}$ mole) citric acid ($C_6H_8O_7.H_2O$) is dissolved in 15 ml distilled water. Then 1.0 mL ($1.74x10^{-2}$ mole) ethylene glycol ($C_2H_6O_2$) is added and all the water is evaporated inside the oil bath at 80ºC. A gel is formed and it is transferred to a high temperature crucible and sintered.

0.5 gr 1 % (mole) Manganese doped Gadolinium-Cerium oxide (1MnGDC) synthesis: 1.239 gr ($2.26x10^{-3}$ mole) Cerium (IV) ammonium nitrate ($(NH_4)_2Ce(NO_3)_6$), 0,258 gr ($5.70x10^{-4}$ mole) Gadolinium (III) nitrate six hydrate ($Gd(NO_3)_3.6H_2O$), 0.008 gr ($1.46x10^{-5}$ mole) Manganese (II) nitrate six hydrate ($MnN_2O_6.6H_2O$) and 1.202 gr ($5.74x10^{-3}$ mole) citric acid ($C_6H_8O_7.H_2O$) are dissolved in 15 mL distilled water. Then 1 mL ($1.74x10^{-2}$ mole) ethylene glycol ($C_2H_6O_2$) is added and all the water is evaporated inside the oil bath

at 80 ^{o}C. A gel is formed and the resulting gel is transferred to a high temperature crucible and sintered.

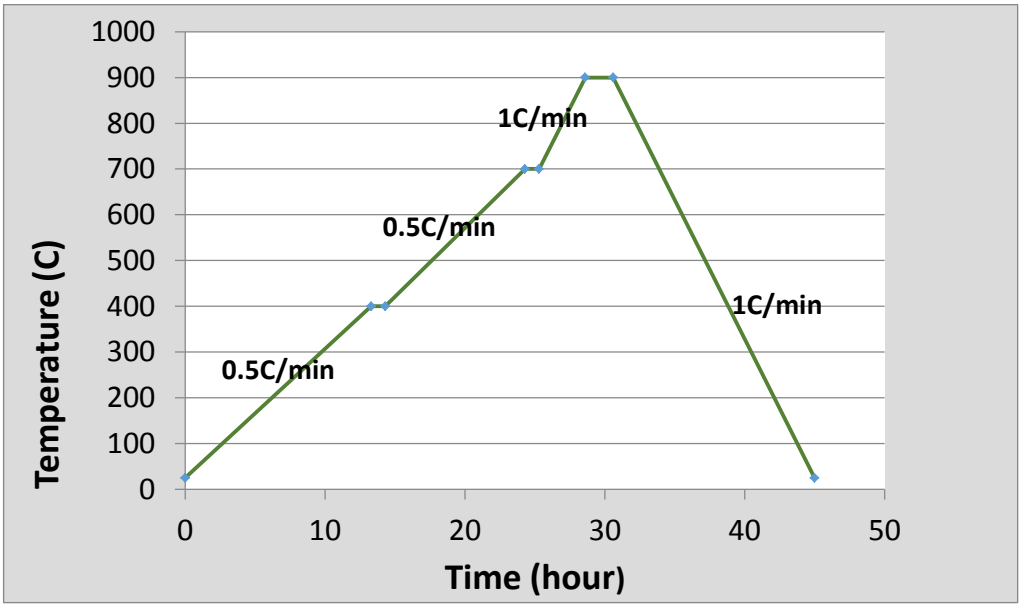

Figure 2.2. MnGDC sintering graph.

0.5 gr 3 % (mole) Manganese doped Gadolinium-Cerium oxide (3MnGDC) synthesis: 1.220 gr ($2.22x10^{-3}$ mole) Cerium (IV) ammonium nitrate ($(NH_4)_2Ce(NO_3)_6$), 0,261 gr ($5.78x10^{-4}$ mole) Gadolinium (III) nitrate six hydrate ($Gd(NO_3)_3.6H_2O$), 0.025 gr ($8.6x10^{-5}$ mole) Manganese (II) nitrate six hydrate ($MnN_2O_6.6H_2O$) and 1.215 gr ($5.78x10^{-3}$ mole) citric acid ($C_6H_8O_7.H_2O$) are dissolved in 15 mL distilled water. Then 1 mL ($1.74x10^{-2}$ mole) ethylene glycol ($C_2H_6O_2$) is added and all the water is evaporated inside the oil bath at 80 ^{o}C. A gel is formed and the resulting gel is transferred to a high temperature crucible and sintered.

0.5 gr 5 % (mole) Manganese doped Gadolinium-Cerium oxide (5MnGDC) synthesis: 1.200 gr ($2.19x10^{-3}$ mole) Cerium (IV) ammonium nitrate ($(NH_4)_2Ce(NO_3)_6$), 0,260 gr

($5.84x10^{-4}$ mole) Gadolinium (III) nitrate six hydrate ($Gd(NO_3)_3.6H_2O$), 0.042 gr ($1.46x10^{-4}$ mole) Manganese (II) nitrate six hydrate ($MnN_2O_6.6H_2O$) and 1.227 gr ($5.84x10^{-3}$ mole) citric acid ($C_6H_8O_7.H_2O$) are dissolved in 15 mL distilled water. Then 1 mL ($1.74x10^{-2}$ mole) ethylene glycol ($C_2H_6O_2$) is added and all the water is evaporated inside the oil bath at 80 ^oC. A gel is formed and the resulting gel is transferred to a high temperature crucible and sintered.

0.5 gr 10 % (mole) Manganese doped Gadolinium-Cerium oxide (10MnGDC) synthesis: 1.149 gr ($2.09x10^{-3}$ mole) Cerium (IV) ammonium nitrate ($(NH_4)_2Ce(NO_3)_6$), 0.270 gr ($5.98x10^{-4}$ mole) Gadolinium (III) nitrate six hydrate ($Gd(NO_3)_3.6H_2O$), 0.086 gr ($2.99x10^{-5}$ mole) Manganese (II) nitrate six hydrate ($MnN_2O_6.6H_2O$) and 1.258 gr ($5.98x10^{-3}$ mole) citric acid ($C_6H_8O_7.H_2O$) are dissolved in 15 mL distilled water. Then 1 mL ($1.74x10^{-2}$ mole) ethylene glycol ($C_2H_6O_2$) is added and all the water is evaporated inside the oil bath at 80 ^oC. A gel is formed and the resulting gel is transferred to a high temperature crucible and sintered.

0.5 gr 15 % (mole) Manganese doped Gadolinium-Cerium oxide (15MnGDC) synthesis: 1.094 gr ($1.96x10^{-3}$ mole) Cerium (IV) ammonium nitrate ($(NH_4)_2Ce(NO_3)_6$), 0,277 gr ($6.14x10^{-4}$ mole) Gadolinium (III) nitrate six hydrate ($Gd(NO_3)_3.6H_2O$), 0.132 gr ($4.6x10^{-4}$ mole) Manganese (II) nitrate six hydrate ($MnN_2O_6.6H_2O$) and 1.290 gr ($6.14x10^{-3}$ mole) citric acid ($C_6H_8O_7.H_2O$) are dissolved in 15 mL distilled water. Then 1 mL ($1.74x10^{-2}$ mole) ethylene glycol ($C_2H_6O_2$) is added and all the water is evaporated inside the oil bath at 80 ^oC. A gel is formed and the resulting gel is transferred to a high temperature crucible and sintered.

0.5 gr 50 % (mole) Manganese doped Gadolinium-Cerium oxide (50MnGDC) synthesis: 0.618 gr ($1.12x10^{-3}$ mole) Cerium (IV) ammonium nitrate ($(NH_4)_2Ce(NO_3)_6$), 0,339 gr ($7.52x10^{-4}$ mole) Gadolinium (III) nitrate six hydrate ($Gd(NO_3)_3.6H_2O$), 0.539 gr ($1.88x10^{-3}$ mole) Manganese (II) nitrate six hydrate ($MnN_2O_6.6H_2O$) and 1.580 gr ($7.52x10^{-3}$ mole) citric acid ($C_6H_8O_7.H_2O$) are dissolved in 15 mL distilled water. Then 1 mL ($1.74x10^{-2}$

mole) ethylene glycol ($C_2H_6O_2$) is added and all the water is evaporated inside the oil bath at 80 ^oC. A gel is formed and the resulting gel is transferred to a high temperature crucible and sintered.

0.5 gr 1 % (mole) Titanium doped Gadolinium-Cerium oxide (1TiGDC) synthesis: 1.239 gr ($2.26x10^{-3}$ mole) Cerium (IV) ammonium nitrate ($(NH_4)_2Ce(NO_3)_6$), 0.237 gr ($5.72x10^{-4}$ mole) Gadolinium (III) nitrate six hydrate ($Gd(NO_3)_3.6H_2O$), 0.010 gr ($2.86x10^{-5}$ mole) Potassium bis (oxalato) oxotitanate (IV) dihydrate (K_2 ($TiO(C_2O_4)_2$).$2H_2O$) and 1.203 gr ($5.72x10^{-3}$ mole) citric acid ($C_6H_8O_7.H_2O$) is dissolved in 20 mL distilled water. Then 1.0 mL ($1.74x10^{-2}$ mole) ethylene glycol ($C_2H_6O_2$) is added and all the water is evaporated inside the oil bath at 80ºC. A gel is formed and it is transferred to a high temperature crucible and sintered.

0.5 gr 1 % (mole) Titanium doped Gadolinium-Cerium oxide (1TiGDC) synthesis: 1.239 gr ($2.26x10^{-3}$ mole) Cerium (IV) ammonium nitrate ($(NH_4)_2Ce(NO_3)_6$), 0.237 gr ($5.72x10^{-4}$ mole) Gadolinium (III) nitrate six hydrate ($Gd(NO_3)_3.6H_2O$), 0.010 gr ($2.86x10^{-5}$ mole) Potassium bis (oxalato) oxotitanate (IV) dihydrate (K_2 ($TiO(C_2O_4)_2$).$2H_2O$) and 1.203 gr ($5.72x10^{-3}$ mole) citric acid ($C_6H_8O_7.H_2O$) is dissolved in 20 mL distilled water. Then 1.0 mL ($1.74x10^{-2}$ mole) ethylene glycol ($C_2H_6O_2$) is added and all the water is evaporated inside the oil bath at 80ºC. A gel is formed and it is transferred to a high temperature crucible and sintered.

0.5 gr 5 % (mole) Titanium doped Gadolinium-Cerium oxide (5TiGDC) synthesis: 1.202 gr ($2.193x10^{-3}$ mole) Cerium (IV) ammonium nitrate ($(NH_4)_2Ce(NO_3)_6$), 0.264 gr ($5.85x10^{-4}$ mole) Gadolinium (III) nitrate six hydrate ($Gd(NO_3)_3.6H_2O$), 0.051 gr ($1.46x10^{-4}$ mole) Potassium bis (oxalato) oxotitanate (IV) dihydrate (K_2 ($TiO(C_2O_4)_2$).$2H_2O$) and 1.229 gr ($5.85x10^{-3}$ mole) citric acid ($C_6H_8O_7.H_2O$) is dissolved in 20 mL distilled water. Then 1.0 mL ($1.74x10^{-2}$ mole) ethylene glycol ($C_2H_6O_2$) is added and all the water is evaporated inside the oil bath at 80ºC. A gel is formed and it is transferred to a high temperature crucible and sintered.

0.5 gr 10 % (mole) Titanium doped Gadolinium-Cerium oxide (10TiGDC) synthesis: 1.153 gr ($2.70x10^{-3}$ mole) Cerium (IV) ammonium nitrate ($(NH_4)_2Ce(NO_3)_6$), 0.271 gr ($6.01x10^{-4}$ mole) Gadolinium (III) nitrate six hydrate ($Gd(NO_3)_3.6H_2O$), 0.106 gr ($3.00x10^{-4}$ mole) Potassium bis (oxalato) oxotitanate (IV) dihydrate (K_2 ($TiO(C_2O_4)_2$).$2H_2O$) and 1.263 gr ($6.01x10^{-3}$ mole) citric acid ($C_6H_8O_7.H_2O$) is dissolved in 20 mL distilled water. Then 1.0 mL ($1.74x10^{-2}$ mole) ethylene glycol ($C_2H_6O_2$) is added and all the water is evaporated inside the oil bath at 80ºC. A gel is formed and it is transferred to a high temperature crucible and sintered.

0.5 gr 20 % (mole) Titanium doped Gadolinium-Cerium oxide (20TiGDC) synthesis: 1.047 gr ($1.90x10^{-3}$ mole) Cerium (IV) ammonium nitrate ($(NH_4)_2Ce(NO_3)_6$), 0.287 gr ($6.36x10^{-4}$ mole) Gadolinium (III) nitrate six hydrate ($Gd(NO_3)_3.6H_2O$), 0.225 gr ($6.36x10^{-4}$ mole) Potassium bis (oxalato) oxotitanate (IV) dihydrate (K_2 ($TiO(C_2O_4)_2$).$2H_2O$) and 1.337 gr ($6.36x10^{-3}$ mole) citric acid ($C_6H_8O_7.H_2O$) is dissolved in 20 mL distilled water. Then 1.0 mL ($1.74x10^{-2}$ mole) ethylene glycol ($C_2H_6O_2$) is added and all the water is evaporated inside the oil bath at 80ºC. A gel is formed and it is transferred to a high temperature crucible and sintered.

0.5 gr 25 % (mole) Titanium doped Gadolinium-Cerium oxide (25TiGDC) synthesis: 0.988 gr ($1.80x10^{-3}$ mole) Cerium (IV) ammonium nitrate ($(NH_4)_2Ce(NO_3)_6$), 0.296 gr ($6.55x10^{-4}$ mole) Gadolinium (III) nitrate six hydrate ($Gd(NO_3)_3.6H_2O$), 0.290 gr ($8.19x10^{-4}$ mole) Potassium bis (oxalato) oxotitanate (IV) dihydrate (K_2 ($TiO(C_2O_4)_2$).$2H_2O$) and 1.378 gr ($6.55x10^{-3}$ mole) citric acid ($C_6H_8O_7.H_2O$) is dissolved in 20 mL distilled water. Then 1.0 mL ($1.74x10^{-2}$ mole) ethylene glycol ($C_2H_6O_2$) is added and all the water is evaporated inside the oil bath at 80ºC. A gel is formed and it is transferred to a high temperature crucible and sintered.

0.5 gr 30 % (mole) Titanium doped Gadolinium-Cerium oxide (30TiGDC) synthesis: 0.927 gr ($1.69x10^{-3}$ mole) Cerium (IV) ammonium nitrate ($(NH_4)_2Ce(NO_3)_6$), 0.305 gr ($6.76x10^{-4}$

mole) Gadolinium (III) nitrate six hydrate ($Gd(NO_3)_3.6H_2O$), 0.359 gr ($1.01x10^{-3}$ mole) Potassium bis (oxalato) oxotitanate (IV) dihydrate (K_2 ($TiO(C_2O_4)_2$).$2H_2O$) and 1.420 gr ($6.76x10^{-3}$ mole) citric acid ($C_6H_8O_7.H_2O$) is dissolved in 20 mL distilled water. Then 1.0 mL ($1.74x10^{-2}$ mole) ethylene glycol ($C_2H_6O_2$) is added and all the water is evaporated inside the oil bath at 80ºC. A gel is formed and it is transferred to a high temperature crucible and sintered.

0.5 gr 50 % (mole) Titanium doped Gadolinium-Cerium oxide (50TiGDC) synthesis: 0.635 gr ($1.15x10^{-3}$ mole) Cerium (IV) ammonium nitrate ($(NH_4)_2Ce(NO_3)_6$), 0.348 gr ($7.72x10^{-4}$ mole) Gadolinium (III) nitrate six hydrate ($Gd(NO_3)_3.6H_2O$), 0.683 gr ($1.93x10^{-3}$ mole) Potassium bis (oxalato) oxotitanate (IV) dihydrate (K_2 ($TiO(C_2O_4)_2$).$2H_2O$) and 1.623 gr ($7.72x10^{-3}$ mole) citric acid ($C_6H_8O_7.H_2O$) is dissolved in 20 mL distilled water. Then 1.0 mL ($1.74x10^{-2}$ mole) ethylene glycol ($C_2H_6O_2$) is added and all the water is evaporated inside the oil bath at 80ºC. A gel is formed and it is transferred to a high temperature crucible and sintered.

0.5 gr 30 % (mole) Titanium doped Gadolinium-Cerium oxide (30TiGDC) synthesis: 0.927 gr ($1.69x10^{-3}$ mole) Cerium (IV) ammonium nitrate ($(NH_4)_2Ce(NO_3)_6$), 0.305 gr ($6.76x10^{-4}$ mole) Gadolinium (III) nitrate six hydrate ($Gd(NO_3)_3.6H_2O$), 0.359 gr ($1.01x10^{-3}$ mole) Potassium bis (oxalato) oxotitanate (IV) dihydrate (K_2 ($TiO(C_2O_4)_2$).$2H_2O$) and 1.420 gr ($6.76x10^{-3}$ mole) citric acid ($C_6H_8O_7.H_2O$) is dissolved in 20 mL distilled water. Then 1.0 mL ($1.74x10^{-2}$ mole) ethylene glycol ($C_2H_6O_2$) is added and all the water is evaporated inside the oil bath at 80ºC. A gel is formed and it is transferred to a high temperature crucible and sintered.

0.5 gr 50% (mole) Titanium doped Gadolinium-Cerium oxide (50TiGDC) synthesis: 0.635 gr ($1.15x10^{-3}$ mole) Cerium (IV) ammonium nitrate ($(NH_4)_2Ce(NO_3)_6$), 0.348 gr ($7.72x10^{-4}$ mole) Gadolinium (III) nitrate six hydrate ($Gd(NO_3)_3.6H_2O$), 0.683 gr ($1.93x10^{-3}$ mole) Potassium bis (oxalato) oxotitanate (IV) dihydrate (K_2 ($TiO(C_2O_4)_2$).$2H_2O$) and 1.623 gr ($7.72x10^{-3}$ mole) citric acid ($C_6H_8O_7.H_2O$) is dissolved in 20 mL distilled water. Then 1.0

mL ($1.74x10^{-2}$ mole) ethylene glycol ($C_2H_6O_2$) is added and all the water is evaporated inside the oil bath at 80ºC. A gel is formed and it is transferred to a high temperature crucible and sintered.

2.4 Vanadium/Manganese Impregnation:

The commercial solid oxide fuel cells that are obtained from Fuel Cell Materials Company are used to investigate the effects of Vanadium oxide and Manganese oxide on the performance of the conventional (Ni-YSZ/YSZ/LSM-YSZ) fuel cell. The thickest layer of the cell is the anode part so the discs are anode supported. The cathode side of the cell can be seen in Figure 2.3a and the anode side of cells can be seen in Figure 2.3b. The mixture of anode (Nickel/Nickel oxide) and electrolyte (YSZ, Yttria stabilized Zirconia) is used as a physical support (NiO/YSZ %50-50) to the cell with 0.5mm thickness. The electrolyte layer (YSZ) is applied with 10-20μm thickness on anode and finally on the electrolyte, cathode material (LSM, Lanthanum Strontium Manganese) is applied with 0.1 mm thickness.

Vanadium is impregnated on the anode side of the cell. Impregnation means that the solution of Vanadium acetyl acetonate is prepared with water and dropped gradually on the anode side. The performance of the plain disc and Vanadium impregnated disc is compared in order to observe the changes on the performance of the fuel cell. 0.1 M Vanadium oxide acetyl acetonate ($VO(acac)_2$) solution with water is prepared; then 10 drops of 0.5 mL solution are dropped on anode layer, drying the anode layer after every drop with the heat gun at 100^{o}C and 250^{o}C respectively. The porous anode layer absorbs NiO/YSZ solution and after that the anode is composed of Nickel and Vanadium. Vanadium impregnated cell is sintered; it is heated it with the rate of 0.5 ^{o}C/min to 400 ^{o}C, then with the rate of 1 ^{o}C/min to 800 ^{o}C, and then with the rate of 0.5 ^{o}C/min to 1400 ^{o}C, finally cooled with the rate of 0.5 ^{o}C/min to room temperature.

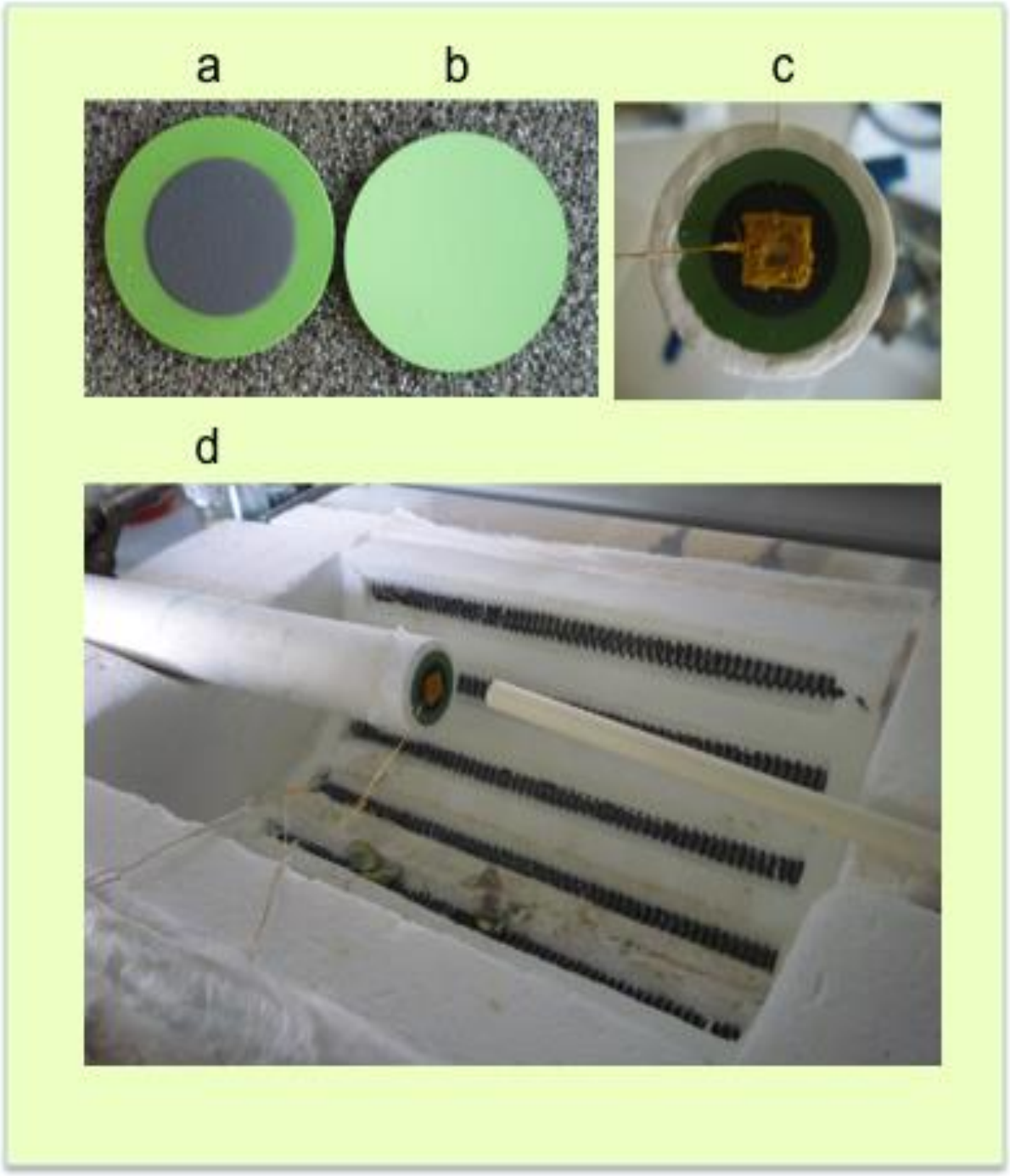

Figure 2.3. a), b) Cathode and anode side of the cell respectively, c) Sealed cell to the alumina tube with golden current collector, d) Experimental setup.

The same procedure is applied for Manganese impregnation. 0.5 gr Manganese(II) nitrate hexahydrate ($MnN_2O_6.6H_2O$) is dissolved in 10ml distilled water (0.174M) and 10 drops of the solution is dropped on the anode side of the cell. The anode side is dried after every drop with the heat gun at 100^oC and 250^oC respectively. Unlike Vanadium impregnated cell, the cell is used directly without sintering. The XRD data is taken from both Manganese and Vanadium impregnated cells to investigate the effects of impregnation on the crystal structure of Ni-YSZ anode material.

The test systems of the fuel cell can be seen in Figure 2.3c-d. On both cathode and anode side of the cell, with golden paste, current collector systems are attached. These systems are composed of golden wires and sieves. Then, the cells are attached to Alumina tubes by using Zirconia paste. The cathode side of the cell can be seen on top of the tube however the anode side is pointed inside of the tube. The fuel is flowed inside the tube and it reaches the anode while the cathode is in touch with air, getting oxygen from air. Then, the tube is placed inside the oven to be heated to 800 ºC with 1ºC/min and in order to reduce Nickel oxide to Nickel, %5 Hydrogen, %95 Nitrogen gas mixture is flowed inside the tube. At the same time air is pumped to the cathode side with the help of a vacuum pump. When the temperature reaches 800ºC, %75 Hydrogen, %25 Nitrogen gas mixture is pumped towards anode and the performance tests are done.

The performance tests are completed by using GAMRY Reference 3000 Potentiostat. The voltage is scanned while the current is measured. According to these data the potential-current and power graph is plotted. The data is compared before and after Vanadium impregnation of the cells. The efficiency of the system is analyzed by using electrochemical methods. After the experiment, XRD results are taken from the anode side of the cell (Figure 2.4).

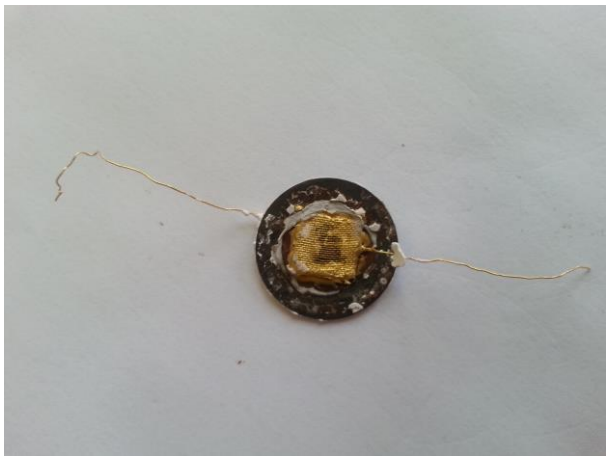

Figure 2.4. Mn impregnated disc anode side taken out of the test tube.

2.5 Van Der Pauw-Four Probe/Conductivity Measurements

The Van Der Pauw is a technique used to measure the resistivity of a sample. The pellets of the samples are prepared as can be seen in Figure 4.5. Golden wires are attached from four sides of the pellet symmetrically. From two arbitrary sides voltage is applied by the potentiostat and current is obtained from the other sides. By dividing voltage values to current values, resistance can be found. In addition, this method provides information about the conductivity of the sample. Conductivity of the sample has a vital importance for us because it determines whether the material is suitable to be used as an anode material or not. Anode materials should be both electrically and ionically conductive, therefore if our sample is conductive then it can be used as an anode material. If it is not, then it is a good candidate as an electrolyte material because an ideal electrolyte possesses negligible conductivity. In Figure 2.5 three kinds of pellets are prepared from the synthesized powders, %10 Manganese Gadolinium doped Ceria (10MnGDC), % 30 Titanium Gadolinium doped Ceria (30TiGDC) and %1 Vanadium Gadolinium doped Ceria (1VGDC).

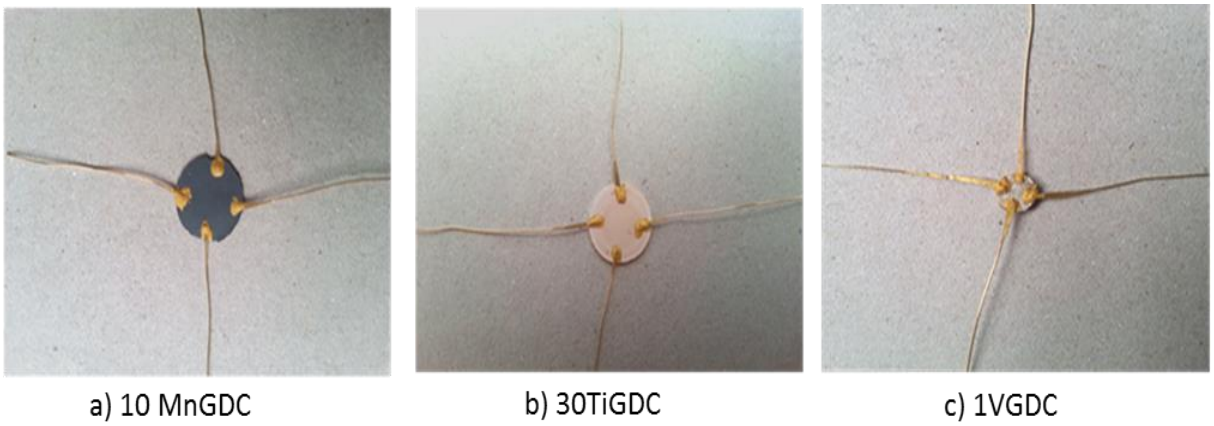

Figure 2.5. Pellets prepared for Van Der Pauw measurement.

Four Probe method is similar to Van Der Pauw method as the resistivity and conductivity of a sample is measured. The main difference between these methods is that, in Four Probe method, the dimensions of the sample are known and the conductivity is calculated according to these dimensions (Equation 2.1). In addition, Linear Sweep Voltammetry is applied for Van Der Pauw measurement whereas chronopotentiometry is applied by the potentiostat for Four Probe measurement.

$$\sigma = 1/R \times L/A \qquad (2.1)$$

Rectangular bars are pressed under 120 MPa and their dimensions are 2x0.5x0.2 cm (length x width x thickness). The thicknesses of the bars are slightly different from each other as thickness depends on the amount of the powder put in the dye. Each bar is sintered by heating them up to 1100°C with the rate of 0.5°C and the dwell time is 2 hours, then cooled to room temperature with the rate of 1°C/min. After sintering, the rectangular bars become harder and four golden wires are attached to the bars 1VDC, 2VGDC, 5MnGDC, 30TiGDC, with the conductive paste. The bars with golden wires are exhibited in Figure 2.6 b-c-d-e. In addition YSZ and GDC bars are produced with the same method from commercial powders. It should be noted that the distance between the wires are equal. The bars are heated to 500°C with the rate of 1°C in order to stick the wires properly.

Then, they are placed in oven and connected to the electrodes (Figure 2.6 f-e). The chronopotentiometry and EIS tests are carried out. From the results, conductivity and activation energies of the materials are calculated.

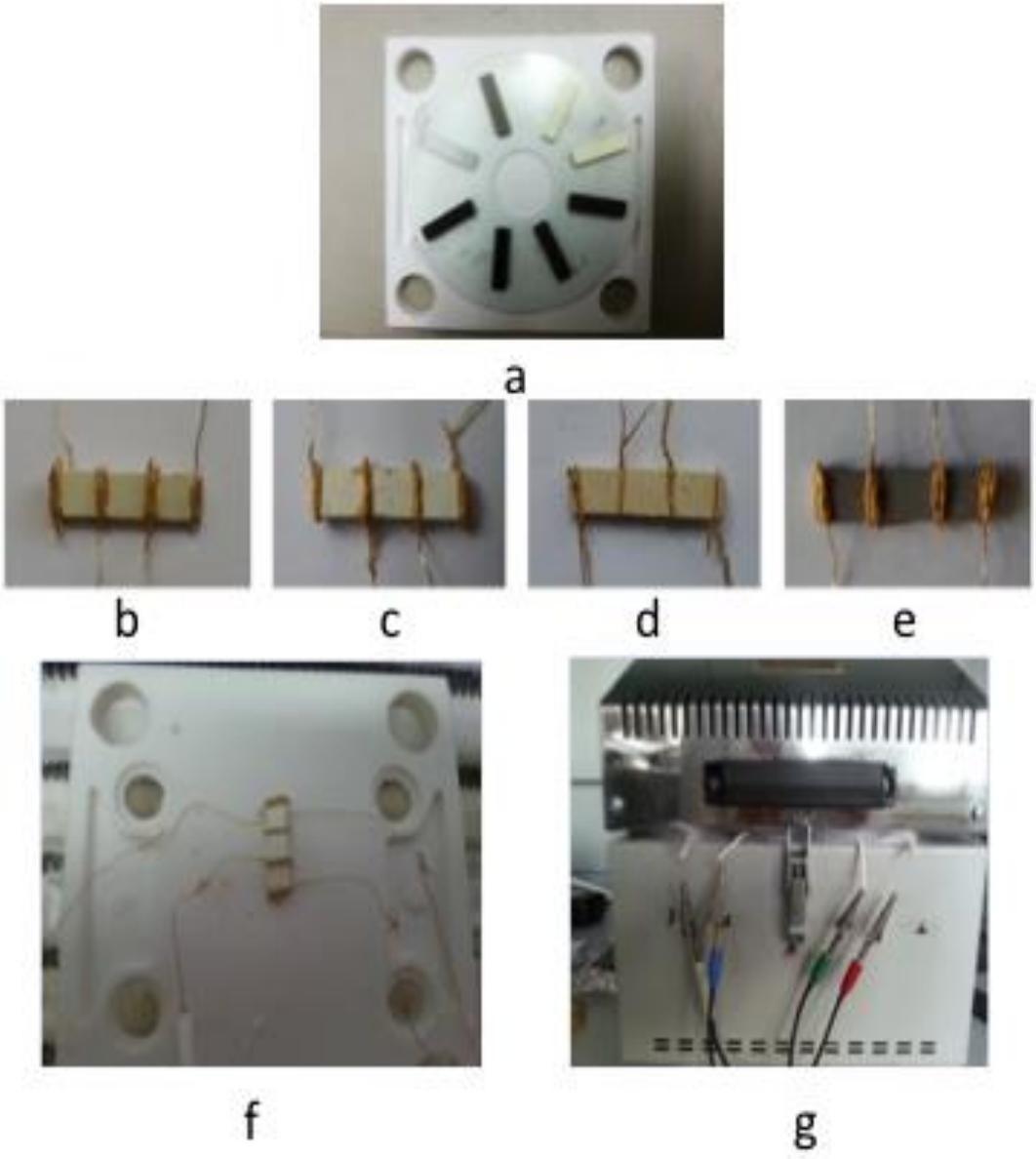

Figure 2.6 a) Sintered pellets b) 1VDC c) 2VGDC d)30TiGDC e) 5MnGDC f) Pellet attached to golden wires in the oven g) Four electrodes attached for four probe measurement.

2.6. Preparation of Symmetric Cells

The synthesized powders as well as YSZ and GDC powders are pressed under 0.2 ton and they formed pellets with 5 mm diameter and 0.3 mm thickness. They are sintered by heating up to 1100°C with the rate of 0.5°C/min and the dwell time is 2 hours. Then, they are cooled to room temperature with the rate of 1°C/min. Some pellets, like YSZ, the maximum temperature is adjusted at 1300°C because these pellets were still fragile after sintering. After this process, the cathode material Lanthanum Strontium Manganese (LSM) is applied symmetrically on both sides of the pellets by using doctor blade on the square shaped masks with 2mm edges. The symmetric cell is sintered again according to temperature program displayed in Figure 2.7. They are heated up to 400ºC with the rate of 0.2 ºC/min and the dwell time is 1 hour, then heating up to 700 ºC with the rate of 0.5 ºC and the dwell time is 1 hour. After these steps, the pellets are heated up to 1100 ºC and there, the dwell time is 12 hours, finally they are cooled to room temperature with the rate of 1ºC/min. In the end the golden wires are attached on the cathode at both sides. In Figure 2.8. a symmetric pellet is shown (a) and the pellet is sealed to the alumina tube by using zirconium ceramic paste connected to electrodes in the oven (b).

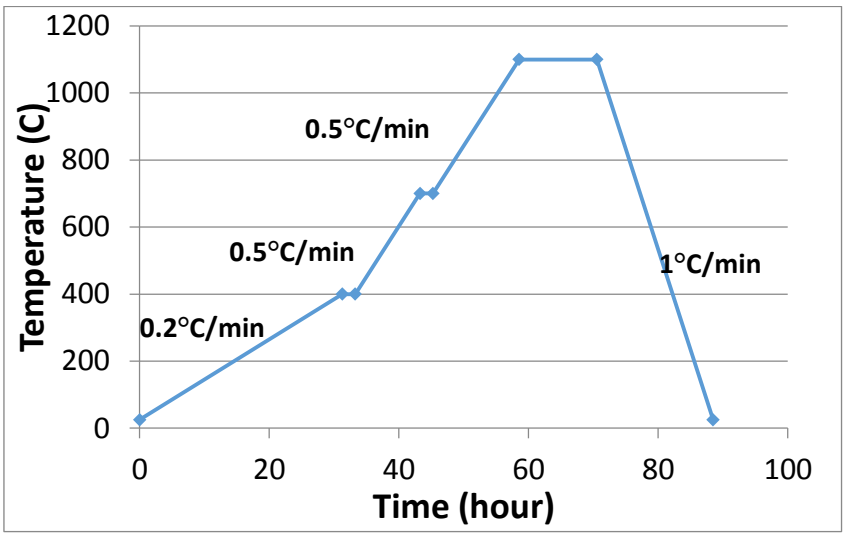

Figure 2.7. Pellet sintering graph with cathode

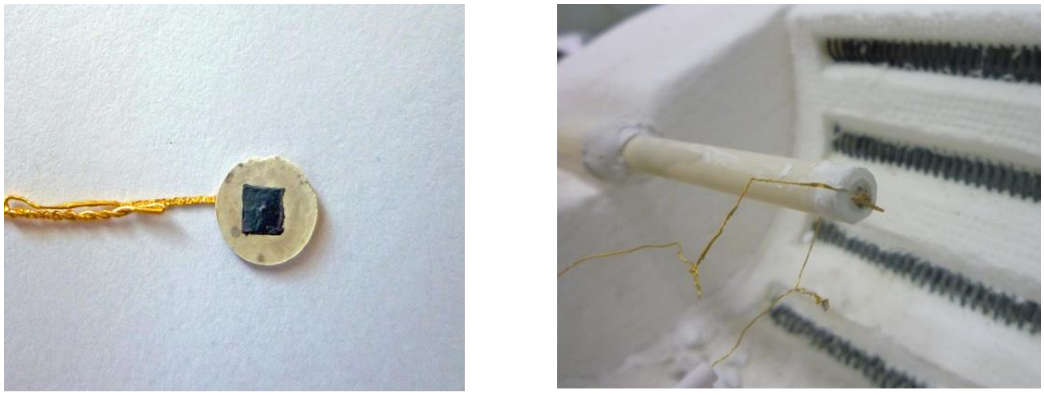

Figure 2.8. a) 1VDC pellet with golden wire attached b) 2VGDC pellet attached to electrodes in the oven.

3. RESULTS AND DISCUSSION

3.1. XRD Results

3.1.1. XRD Results of Cerium oxide Compounds

The XRD results of VGDC compounds are shown in Figure 3.1. The peaks at 28.5, 32.6, 47.5, 56.5, 59.2, 69.8 2θ indicate Cerium Oxide structure. The difference between 2VGDC (Figure 3.1.b) and 3VGDC at 25 2θ and at 32.5 2θ (Figure 3.1.c) means that Cerium Vanadium oxide is formed as a different crystal structure. It is clearly seen that this crystal structure is formed after synthesis of 10VGDC (Figure 3.1.f). When Vanadium is doped with more than %2 proportions, another crystal structure, Cerium Vanadium Oxide ($CeVO_4$), which has distinct properties from Cerium Oxide (Ce_2O_3-CeO_2) is formed. This material is not desired for a novel electrolyte material because the properties of the new crystal structure are not suitable for SOFC operations. As a result 1 VGDC and 2 VGDC are chosen for electrolyte and anode applications.

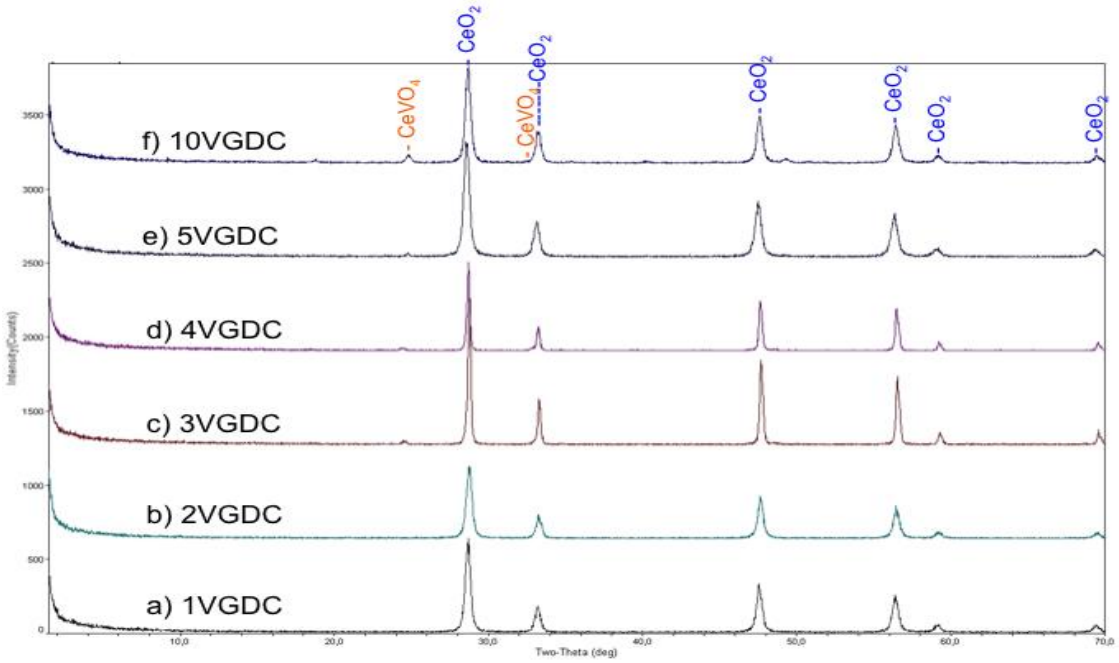

Figure 3.1. XRD results of VGDC.

The XRD results of VDC compounds are shown in Figure 3.2. The peaks at 28.5, 32.6, 47.5, 56.5, 59.2, 69.8 2θ indicate Cerium Oxide structure. The difference between 1VDC (Figure 3.2a) and 2VDC (Figure 3.2b) shows that Cerium Vanadium oxide is formed as a different crystal structure. When Vanadium is doped with more than %1 proportion, another crystal structure, Cerium Vanadium Oxide ($CeVO_4$), which has distinct properties from Cerium Oxide (Ce_2O_3-CeO_2) is formed. This material is not desired for a novel electrolyte material because the properties of the new crystal structure are not suitable for SOFC operations. As a result 1VDC is chosen for electrolyte and anode applications.

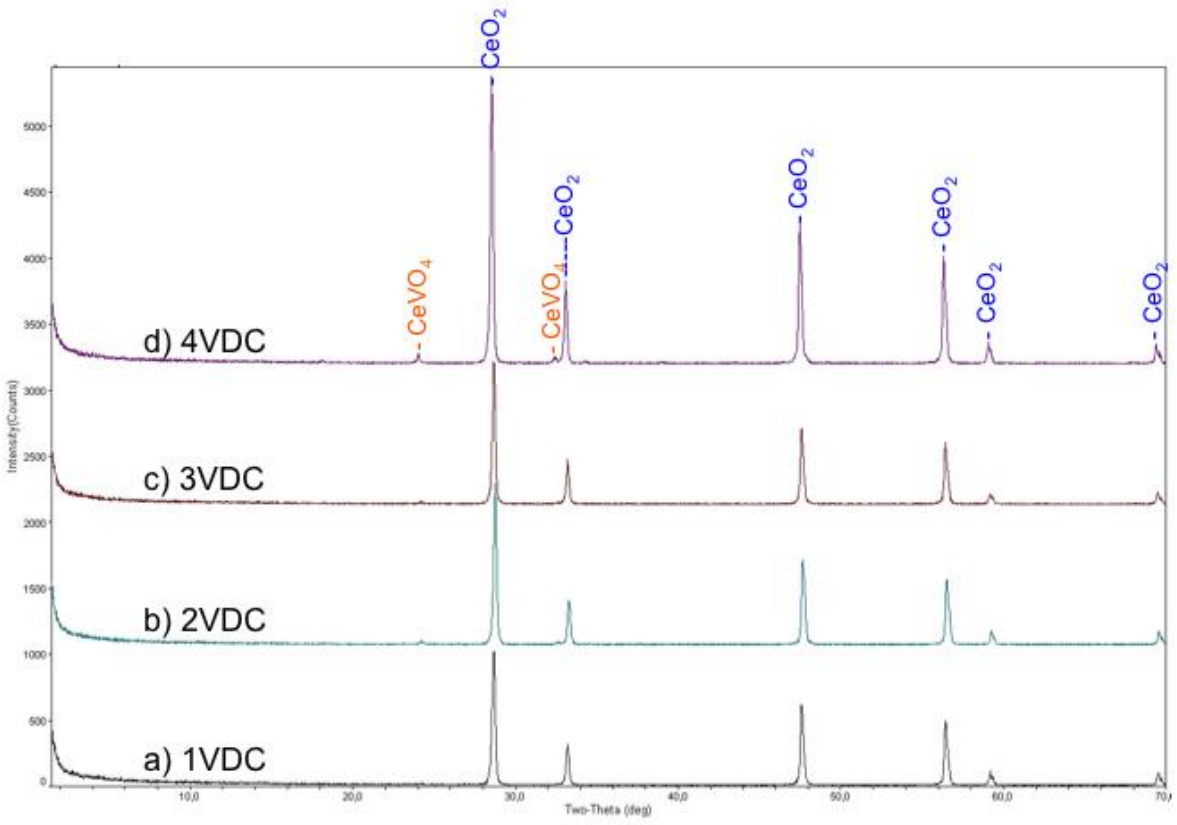

Figure 3.2. XRD results of VDC.

The XRD results of MnGDC compounds are shown in Figure 3.3. Cerium Oxide structure can be seen at the bottom. 1,3 and 5 MnGDC (Figure 3.3a, b, c) fits to this structure however 10MnGDC does not fit it due to the peaks that form at 31.5 and 59.7 2θ.

The formation is obvious at 50MnGDC (Figure 3.3f) and the peaks can be clearly observed at 31.5, 34.5, 36, 38, 43, 50.7 2θ. This indicates that Manganese oxide (MnO_x) is formed as a different crystal structure than Cerium Oxide (Ce_2O_3-CeO_2). When Manganese is doped with more than %5 proportion, another crystal layer of Manganese oxide (MnO_x) is formed. This material is not desired for a novel electrolyte material because the properties of the new crystal structure are not suitable for SOFC operations. As a result 5MnGDC and lower amount of doped MnGDC compounds are suitable for electrolyte and anode applications.

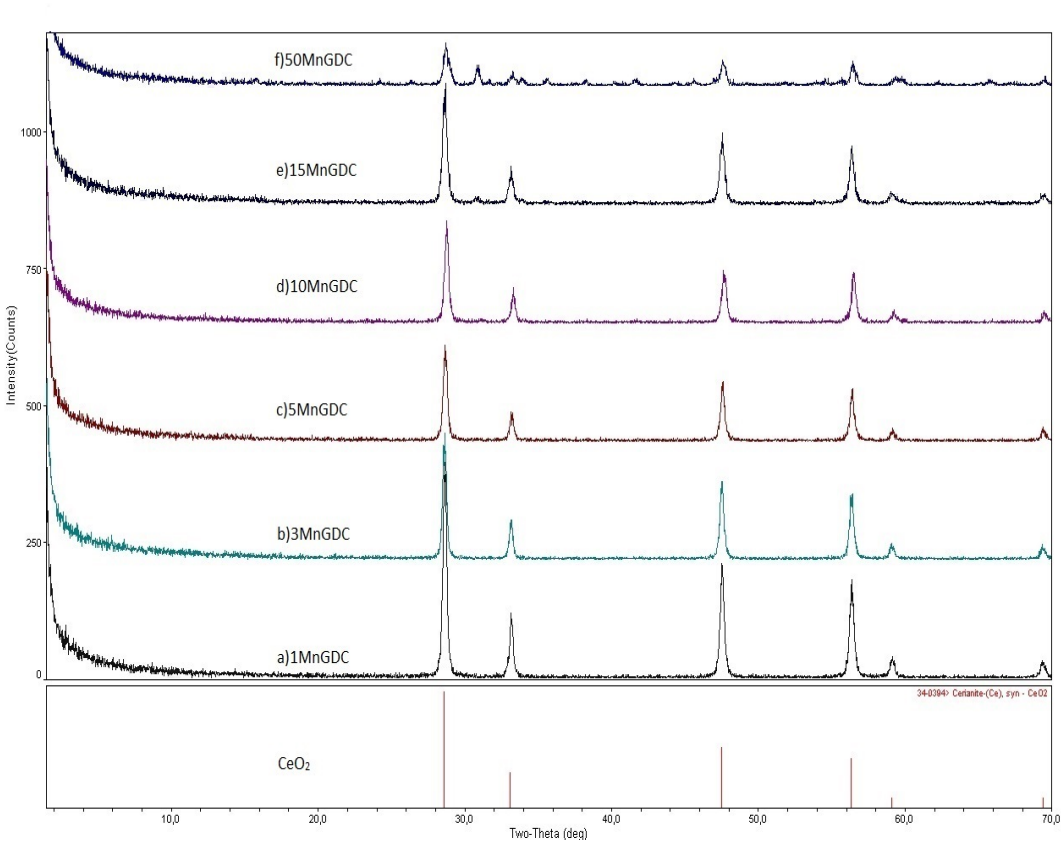

Figure 3.3. XRD results of MnGDC.

The XRD results of TiGDC compounds are shown in Figure 5.4. Cerium Oxide structure can be seen at the bottom. 1TiGDC (Figure 3.4a) has a better crystal structure than other compounds due to the sharper peaks. When 30TiGDC (Figure 3.4f) and 50TiGDC (Figure 3.4.g) are compared, 50 TiGDC has additional peaks at 4, 12, 31, 34 2θ.

This indicates that Titanium oxide is formed as a different crystal structure. When Titanium is doped with more than %30 proportions, another crystal structure, Titanium Oxide (TiO_2), which has distinct properties from Cerium Oxide (Ce_2O_3-CeO_2) is formed. This material is not desired for a novel electrolyte material because the properties of the new crystal structure are not suitable for SOFC operations. As a result 30TiGDC and lower amount of doped TiGDC compounds are chosen for electrolyte and anode applications.

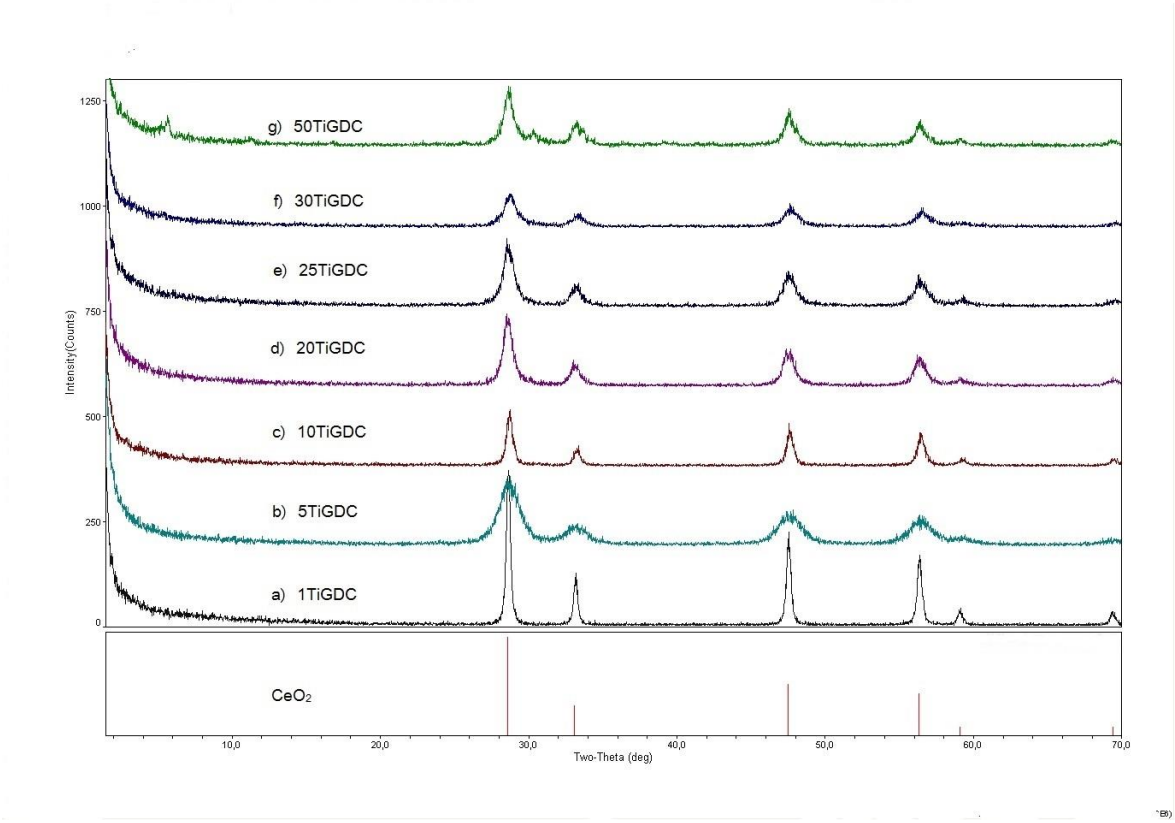

Figure 3.4. XRD results of TiGDC.

3.1.2. XRD Results of Manganese/Vanadium Impregnated SOFCs

The XRD results of Vanadium impregnated SOFC is shown in Figure 3.5. Nickel Oxide peaks are seen at 37, 43, 62 2θ, Yttria stabilized Zirconia peaks are seen at 30, 34, 35, 50, 59, 60 2θ. The sample was grinded and was in powder form so the cathode, Lanthanum Strontium Manganese peaks appeared on XRD at 23, 32, 40, 46, 58, 68 2θ. The

peaks at 28, 31, 47 2θ indicate a phase formed by Vanadium and is close to Vanadium oxide and Vanadium Yttrium oxide structure. However, these peaks could not match exactly to XRD peaks that belong to the cell and we assume that a different crystal structure is formed by Vanadium.

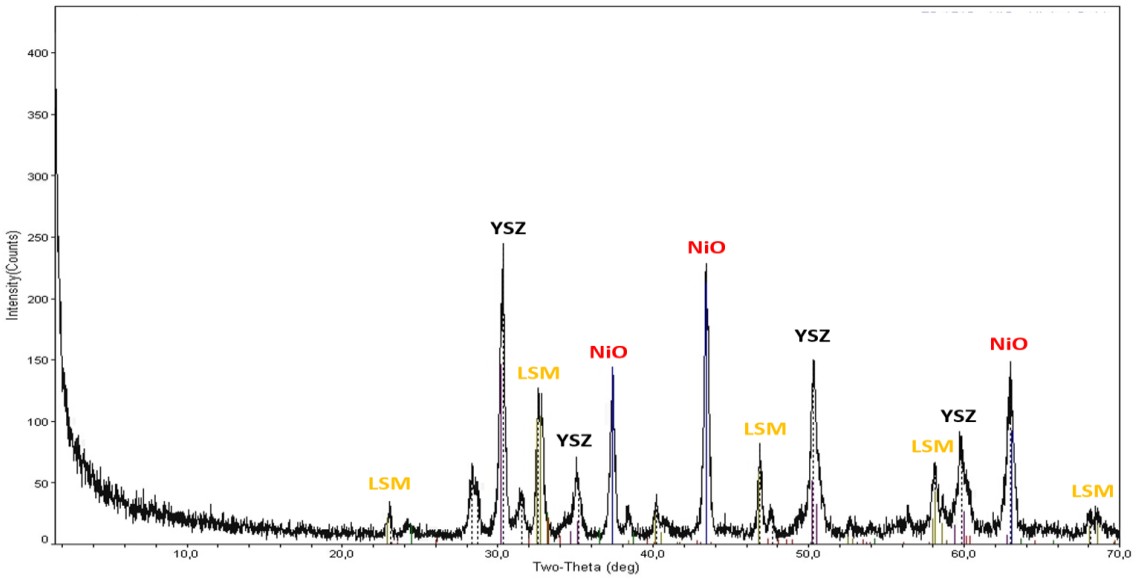

Figure 3.5. XRD Vanadium impregnated cell.

The XRD results of Manganese impregnated SOFC is shown in Figure 3.6. Nickel Oxide peaks are seen at 37, 43, 62 2θ, Yttria stabilized Zirconia peaks are seen at 30, 34, 35, 50, 59, 60 2θ and Gold peaks is seen at 38, 44 and 64 2θ. None of Manganese peaks appear on the graph, this means that there is no phase separation due to Manganese impregnation and Manganese diffused into the crystal structure of anode completely.

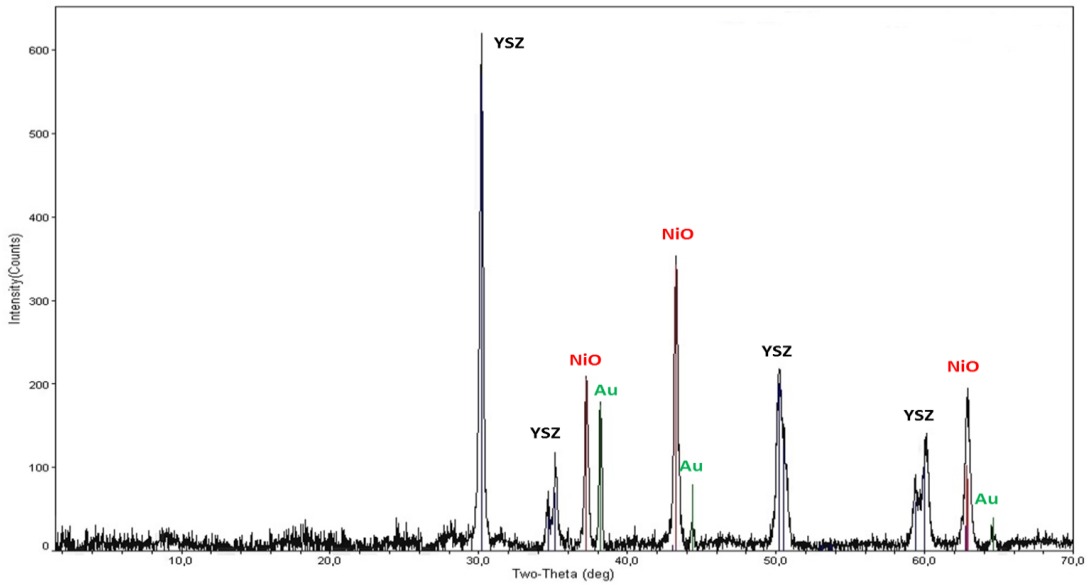

Figure 3.6. XRD results of Manganese impregnated anode cell.

3.2 Vanadium Impregnated Cells Performance Test Results:

The SOFCs with Ni-YSZ anode are used for impregnation and performance tests and voltage-current-power (V-I-P) values are obtained. Performance of fuel cell as a combination of voltage-current density and power density-current density graphs are displayed in Figure 3.7 by comparing the performances of a conventional Ni-YSZ anode cell and Vanadium impregnated cell. The maximum point on the power density curve gives us information about the performance of the cell. As it can be seen in the graph, the maximum power density of the cell without Vanadium is about 55mW/cm^2. After Vanadium is added to the anode, power density of the cell becomes 68mW/cm^2. These values prove that Vanadium enhances the cell efficiency about % 25. The reason for this improvement is that the oxide ions (O^{-2}) are bonded to Vanadium easier than Nickel. In addition, carbon deposition problem for Nickel can be solved by impregnating Vanadium to Ni-YSZ anode.

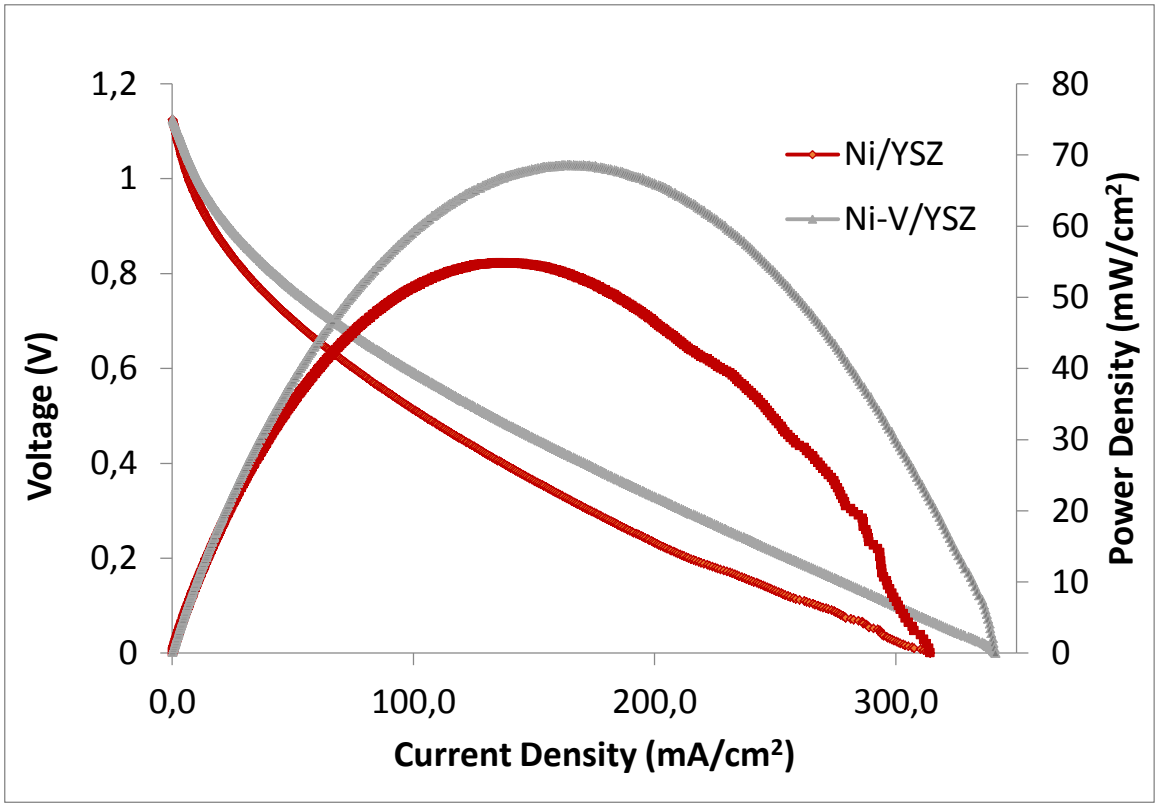

Figure 3.7. Comparison of V impregnated Ni-YSZ anode cell and Ni-YSZ anode cell in terms of voltage, current density and power density at 800°C.

Electrochemical Impedance Spectroscopy results for Vanadium impregnated cell and conventional Ni-YSZ cell without Vanadium are demonstrated in Figure 3.8. The ohmic resistances of the two cell are the same (1.5 Ω*cm^2) because cells are identical. The polarization resistance which is can be seen on the x- axis of the arc, gives us information about the mass transfer processes of each cell. It can be seen that, the polariation resistances of the cells are obviously different from each other, the cell with Vanadium has 1.24 Ω*cm^2 resistance and the cell without Vanadium has 2.20 Ω*cm^2 resistance. Impregnation of Vanadium decreases the polarization resistance of the cell, therefore, we can conclude that oxide ion transport is easier when Vanadium is added to the anode.

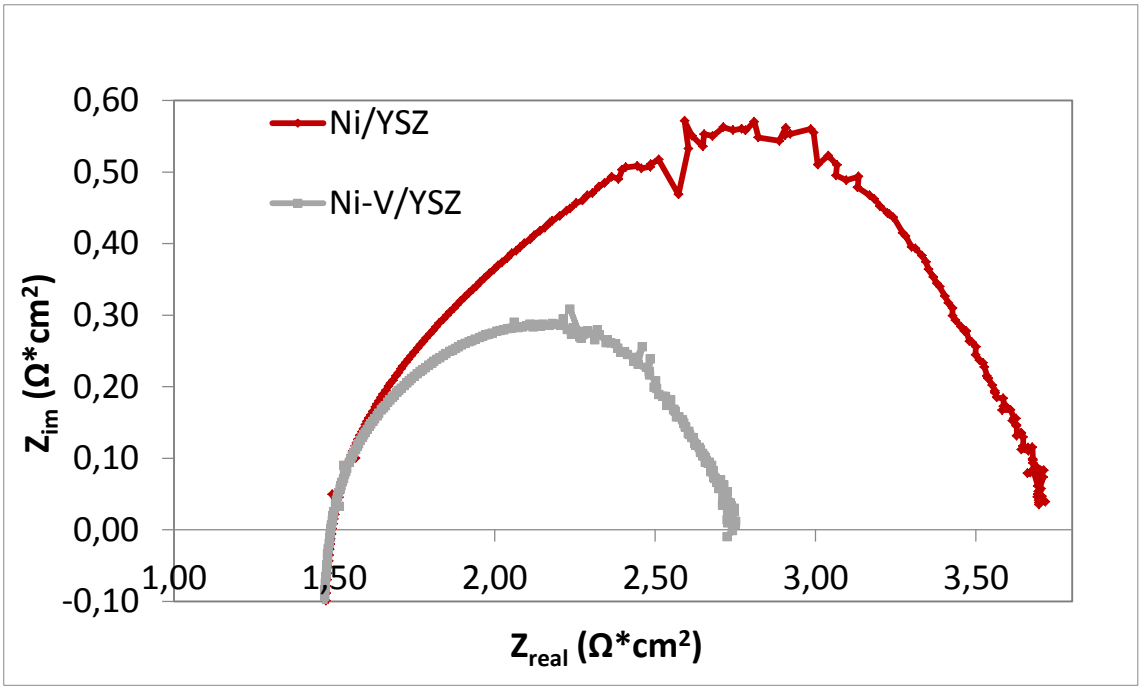

Figure 3.8. Comparison of EIS data: Ni-YSZ anode cell and Vanadium impregnated NiYSZ anode cell at OCV.

The combination of voltage-current density and power density-current density graphs of conventional Ni-YSZ anode cell and Manganese impregnated cell are shown in Figure 3.9. The maximum point on the power density curve gives us information about the performance of the cell. As it can be seen in the graph, the maximum power density of the cell without Manganese is about 73mW/cm^2. After Manganese is added to the anode, power density of the cell becomes 179mW/cm^2. These values prove that Manganese enhances the cell efficiency tremendously, about % 145. The reason for this improvement is that the oxide ions (O^{-2}) are bonded to Manganese easier than Nickel as well as electrical conductivity is enhanced due to impregnation. In addition, carbon deposition problem for Nickel can be solved by impregnating Manganese to the Ni-YSZ anode.

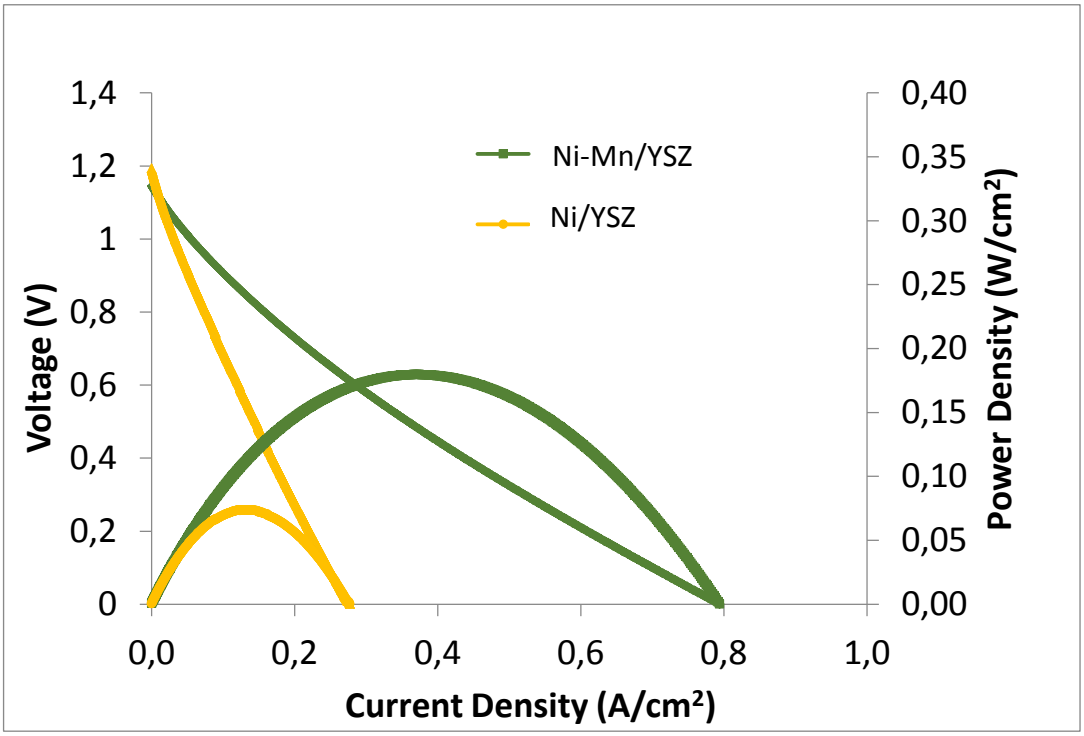

Figure 3.9. Comparison of Mn impregnated Ni-YSZ anode cell and Ni-YSZ anode cell in terms of voltage, current density and power density at 800°C.

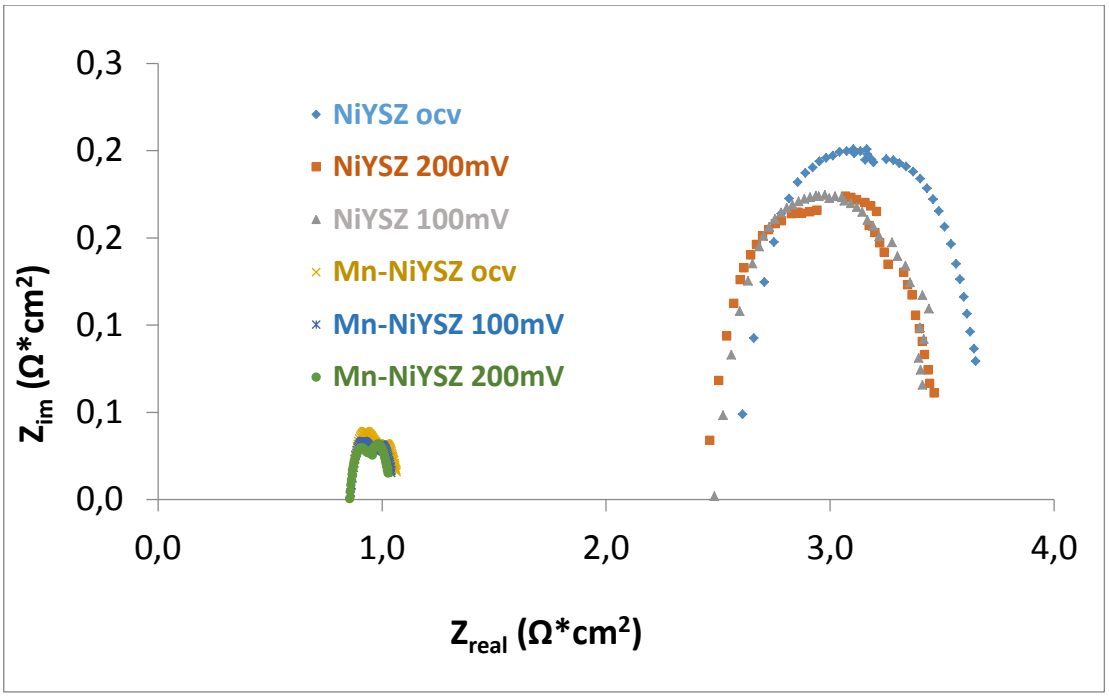

Figure 3.10. Comparison of EIS data: Mn impregnated Nİ-YSZ anode cell and NiYSZ anode cell at OCV and 100, 200 mV overpotential.

The Electrochemical Impedance Spectroscopy results for Manganese impregnated cell and conventional N,-YSZ cell without Manganese are shown in Figure 3.10. Data is taken at different overpotential values, at OCV, 100 mV and 200 mV. The ohmic resistances of the two cell are different, the cell with Manganese has 0.85 $\Omega*cm^2$ ohmic resistance whereas the conventional cell has nearly 2.5 $\Omega*cm^2$. There is a significant change in the ohmic resistance and this phenomenon indicates that there is an increase in electrical conductivity of the system. The polarization resistance which can be seen on the x- axis of the arc, gives us information about the mass transfer processes of each cell. It can be seen that, the polariation resistances of the cells are far different from each other, the cell with Manganese has 0.15 $\Omega*cm^2$ resistance and the cell without Manganese has 1 $\Omega*cm^2$ resistance on average. It should be noted that as overpotential is increased, the polarization resistance decrease which is an expected result. Overall, impregnation of Manganese enhances the electrical conductivity of the cell and Oxygen transport is easier when Manganese is added to the anode. An example from the literature is that Manganese-Nickel bimetal oxide catalysts are effective for selective catalytical reduction of NO at low temperatures. [38]. Another example is that, Nickel catalysts supported on Manganese-Cerium mixed oxides can be used Water-Gas Shift reaction [39]. Manganese is used with Cerium as a catalyst in this study and %30 Mn/Ce ratio yielded good results. Therefore, it would be beneficial if Manganese impregnation method is used on Ceria based anodes in our study for an enhancement of the performance of the cell.

3.3 Raman Results

The synthesized powders as well as GDC and YSZ are analyzed with Raman spectrometer at 532 nm. A novel SOFC from these materials will be manufactured and tested with a Raman monitoring system at high temperatures. To observe the changes at higher temperatures, these compounds are initially analyzed at room temperature. In Figure 3.11 Raman spectroscopy results of 1VDC can be seen. There is a single peak at 464 cm^{-1} which belongs to Ceria [40].

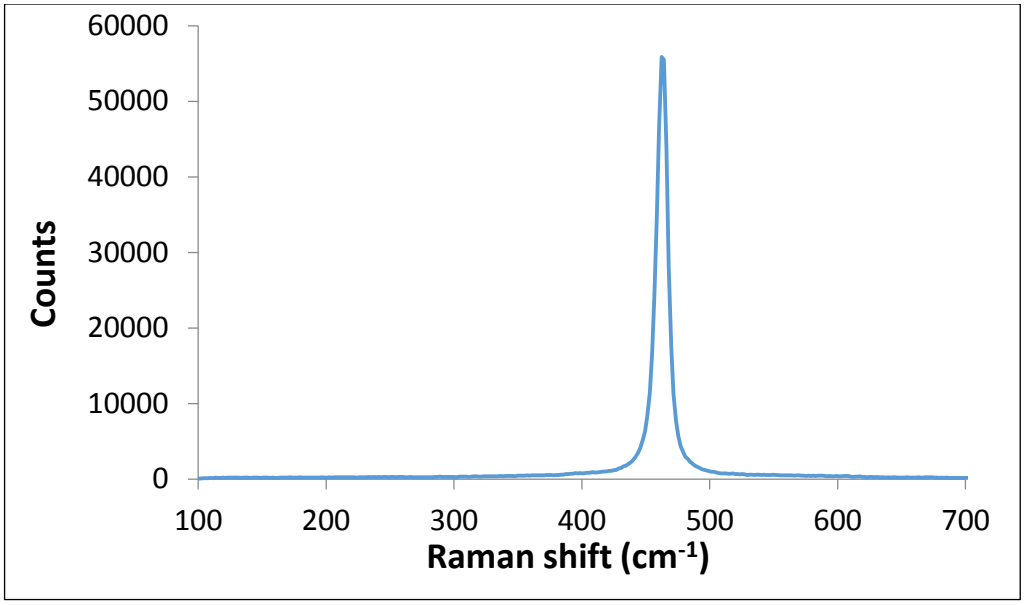

Figure 3.11. Raman spectrum of 1VDC.

In Figure 3.12 Raman spectroscopy results of 2VGDC can be seen. There are two peaks at 464 cm^{-1} and 553 cm^{-1}. GDC gives signal at 462 cm^{-1} which correlates with the literature [41] and the signal at 553 cm^{-1} Gadolinium oxide peaks.

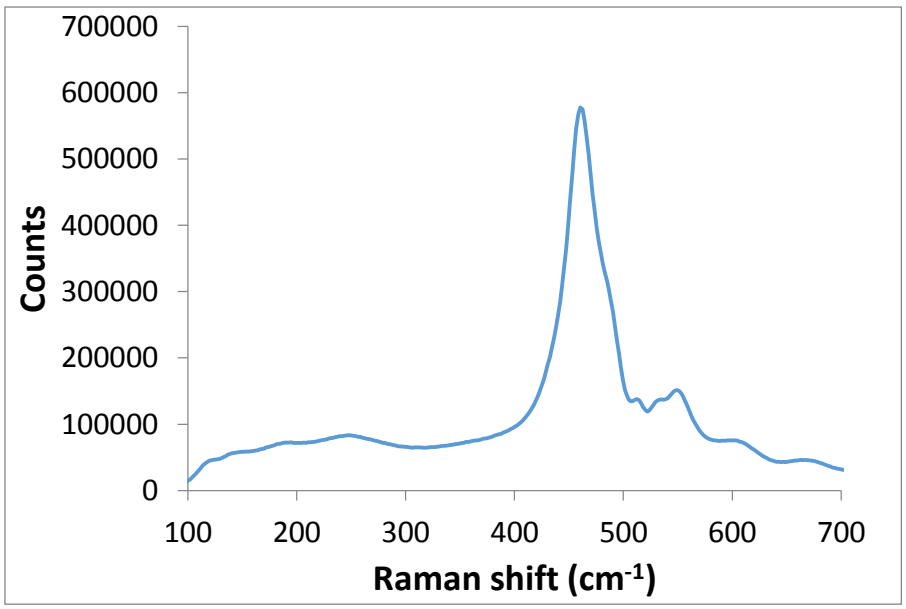

Figure 3.12. Raman spectrum of 2VGDC.

In Figure 3.13 Raman spectroscopy results of 5MnGDC can be seen. There are two peaks at 455 cm^{-1} and 590 cm^{-1}. MnGDC gives signal at 455 cm^{-1} and Gadolinium oxide gives signal at 593 cm^{-1}. There is a slight difference of the peaks from the previous measurements.

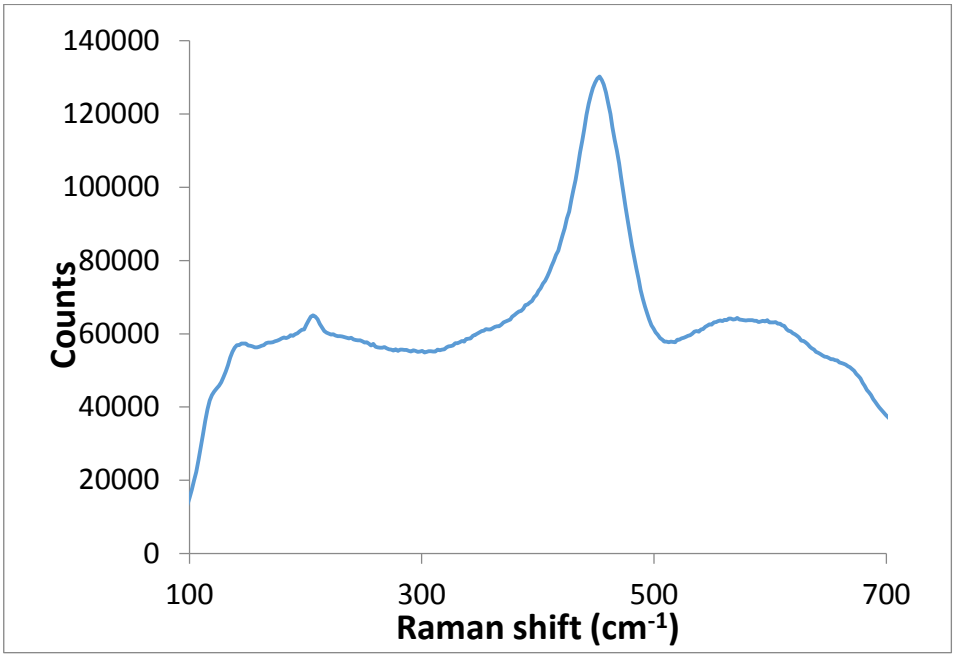

Figure 3.13. Raman spectrum of 5MnGDC.

Raman spectroscopy results of 30 TiGDC can be seen in Figure 3.14. There are two peaks at 464 cm^{-1} and 538 cm^{-1}. TiGDC gives signal at 464 cm^{-1} and Gadolinium oxide gives signal at 580 cm^{-1}.

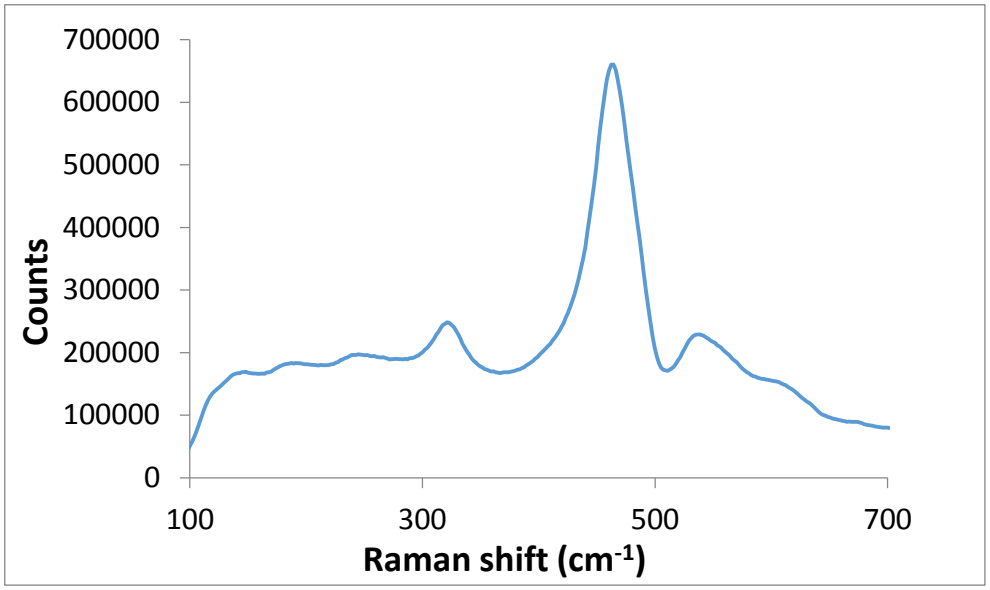

Figure 3.14. Raman spectrum of 30TiGDC.

In Figure 3.15 Raman spectroscopy results of GDC can be seen. There are three peaks at 464 cm^{-1}, 538 cm^{-1} and 490 cm^{-1}. GDC gives signal at 464 cm^{-1} and Gadolinium oxide gives signal at 544 cm^{-1}.

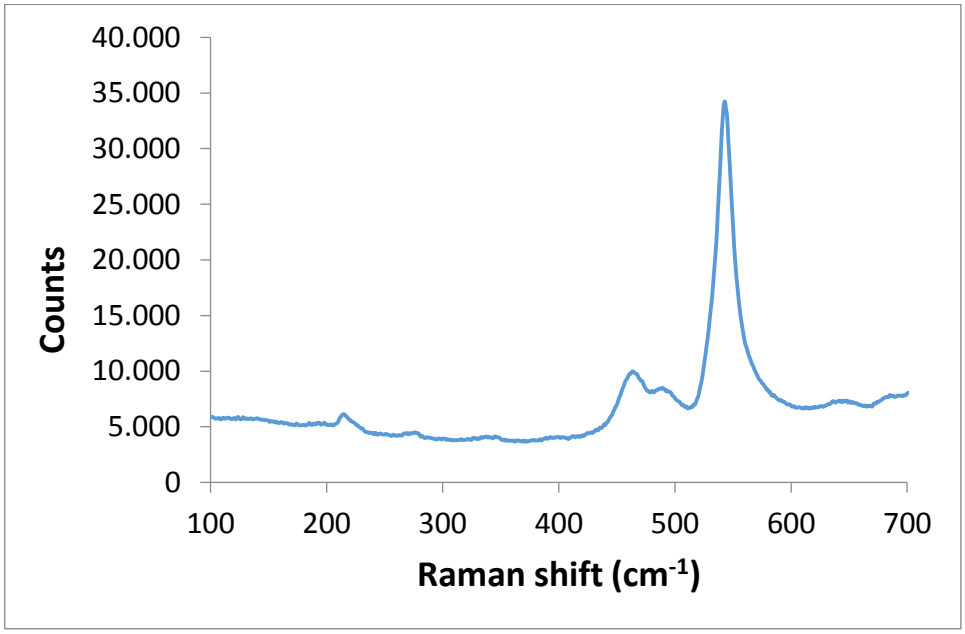

Figure 3.15. Raman spectrum of GDC.

In Figure 3.16 Raman spectroscopy results of YSZ can be seen. There are four peaks at 497 cm^{-1}, 575 cm^{-1}, 621 cm^{-1}, 984 cm^{-1}. The results are similar to the literature results [42-43].

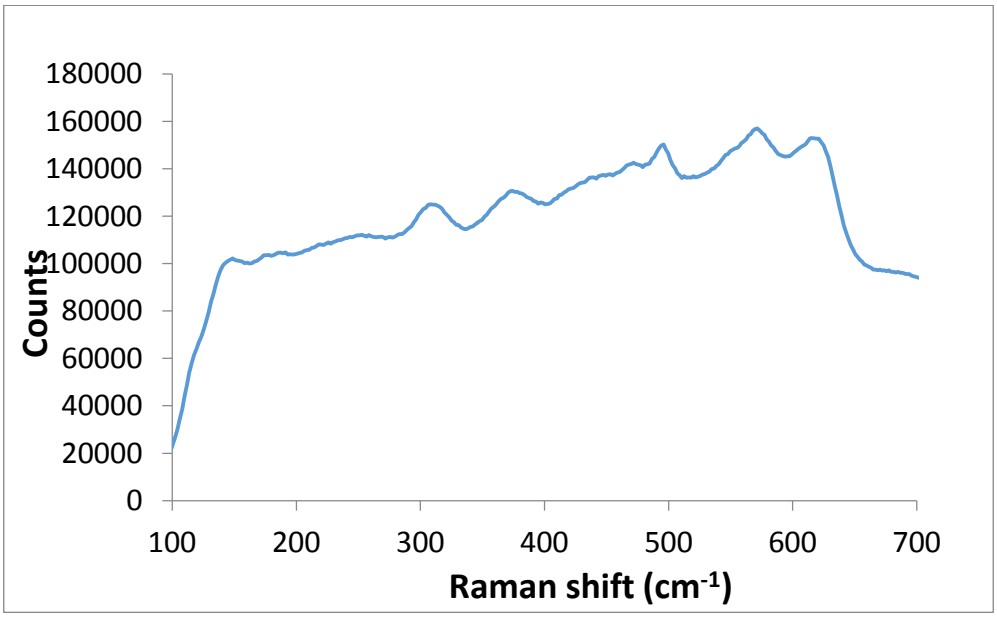

Figure 3.16. Raman spectrum of YSZ.

3.4. Electrical Conductivity Results

Two-step chronopotentiometry experiments are completed to measure the conductivity values of as prepared materials in this study. Constant current is applied from two electrodes to the sintered rectangular bars for 60 seconds. Voltage vs. time graph of YSZ (as standard SOFC electrolyte material) at 450°C, 500°C, 550 °C and 600 °C is displayed in Figure 3.17. The current value is doubled after 30 seconds while the voltage value is also doubled and it can be observed on the graph clearly. For the first 30 seconds the voltage values are 0.44 V, 0.15 V, 0.05 V, 0.025 V at 450 °C, 500 °C, 600°C respectively. For the second half, the voltage values are 0.88 V, 0.3V, 0.1 V, 0.05 V at 450 °C, 500 °C, 600°C respectively. As the temperature is increased, the voltage values decrease. The reason is that the electrical conductivity of the compound increases as the temperature is increased. Therefore, the resistance drops and can be easily calculated when applied to ohm's law (V = IxR), since the voltage value decreases when temperature is increased. The applied current differs for every compound, an electrically conductive material has low resistance and in order to obtain the voltage value, it is necessary to apply higher current (V = IxR). The other way around is also valid for a material having low electrical conductivity. YSZ is a conventional electrolyte material and has low electrical conductivity, 10^{-6} A current is applied whereas GDC is electrically more conductive than YSZ and the current that is applied is 10^{-4} A.

Electrical conductivity measurements of GDC at various temperatures (450°C, 500°C, 550 °C and 600 °C) are displayed in Figure 3.18. The current value is doubled after 30 seconds while the voltage value is also doubled and it can be observed on the graph clearly. For the first 30 seconds the voltage values are 0.57 V, 0.27 V, 0.14 V, 0.07 V at 450 °C, 500 °C, 600°C respectively. For the second half, the voltage values are 1.16 V, 0.55 V, 0.28 V, 0.15 V at 450 °C, 500 °C, 600°C respectively. As the temperature is increased, the voltage values decrease.

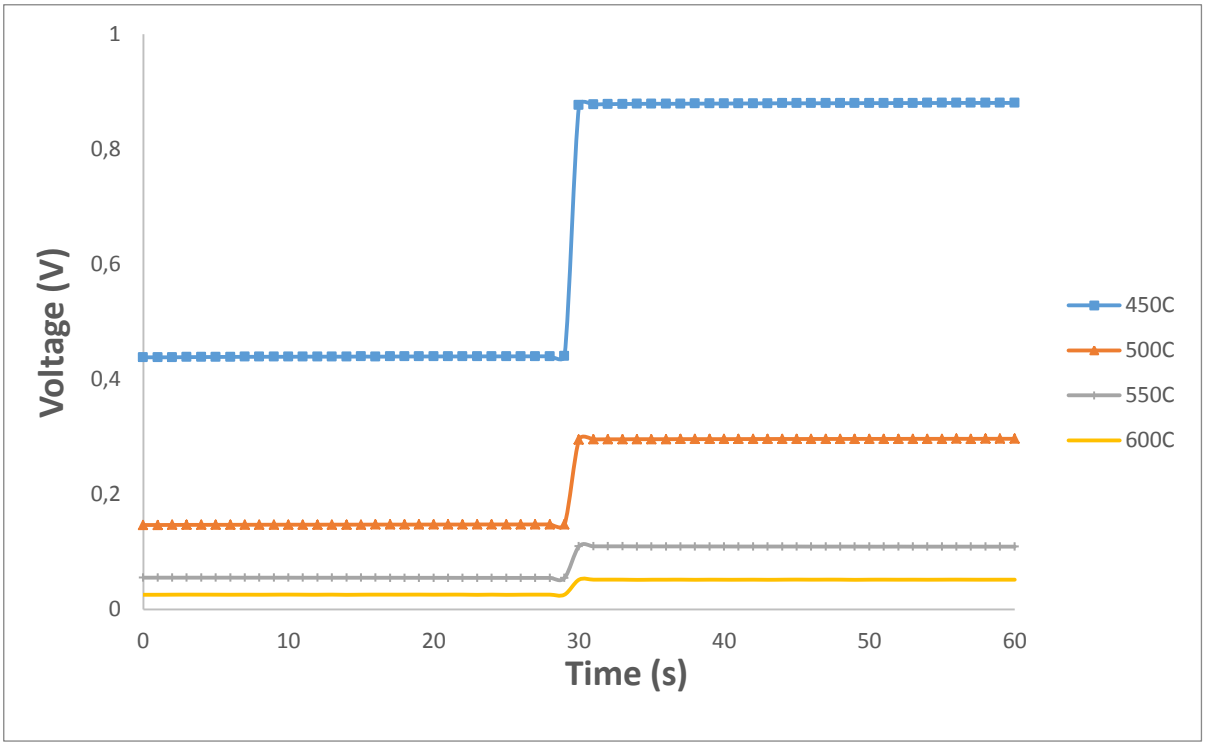

Figure 3.17. Electrical conductivity YSZ at various temperatures.

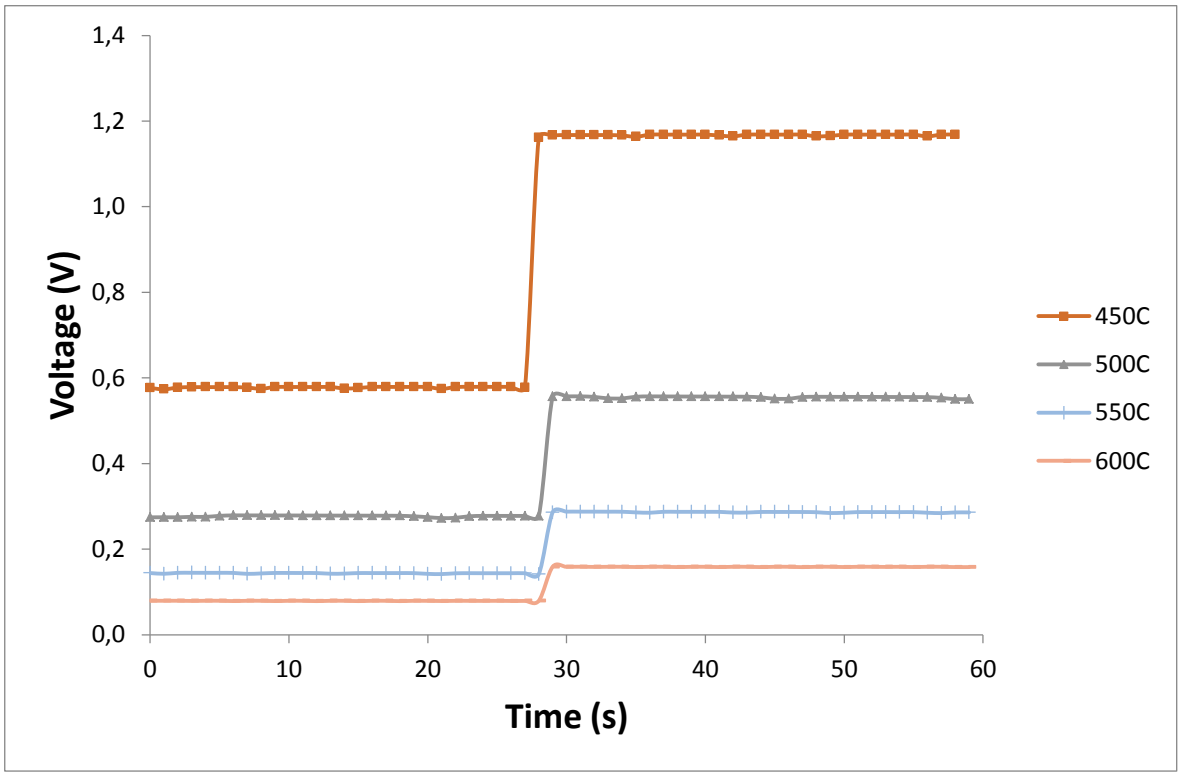

Figure 3.18. Electrical conductivity of GDC at various temperatures.

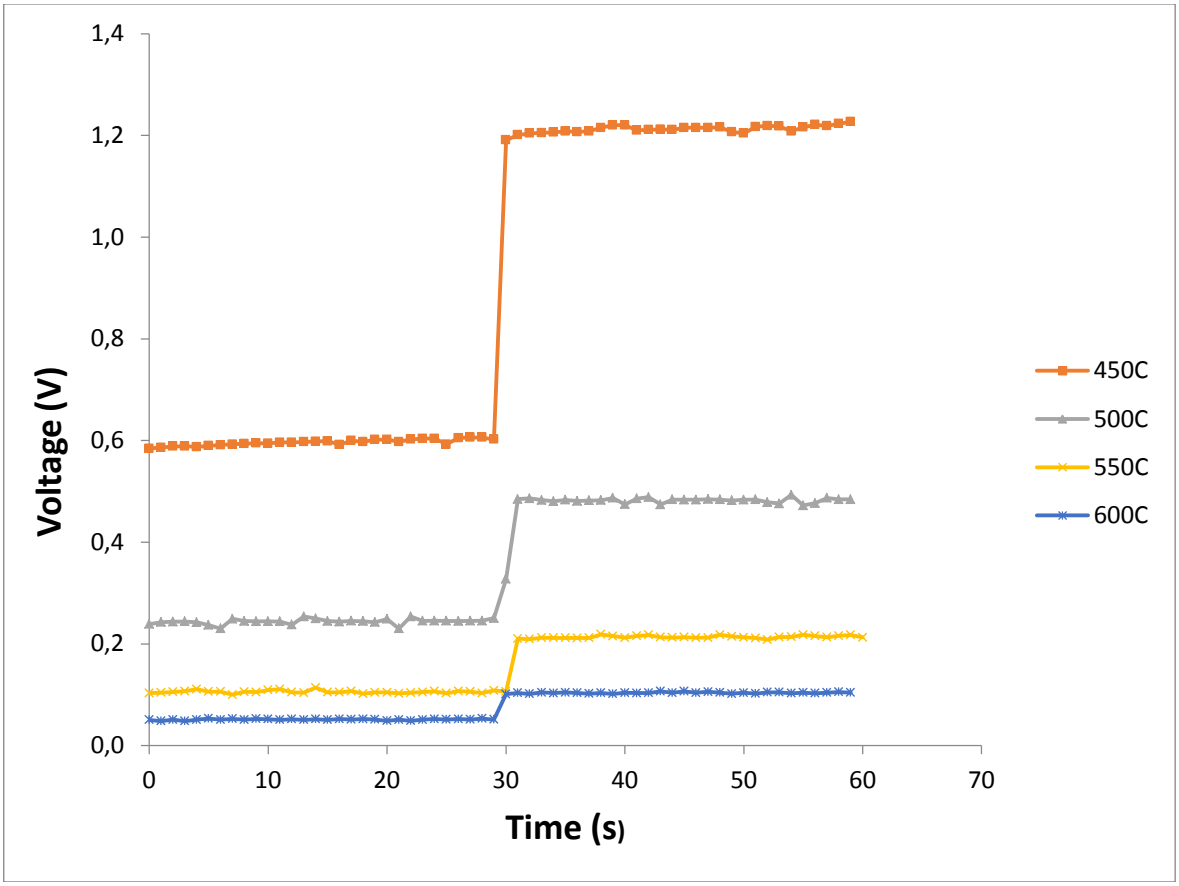

Figure 3.19. Electrical conductivity of 1VDC at various temperatures.

Electrical conductivity measurements of 1VDC at various temperatures (450°C, 500°C, 550 °C and 600 °C) are displayed in Figure 3.19. The current value is doubled after 30 seconds while the voltage value is also doubled and it can be observed on the graph clearly. For the first 30 seconds the voltage values are 0.6 V, 0.24 V, 0.1 V, 0.05 V at 450 °C, 500 °C, 600 °C respectively. For the second half, the voltage values are 1.21 V, 0.47 V, 0.21 V, 0.10 V at 450 °C, 500 °C, 600 °C respectively. As the temperature is increased, the voltage values decrease.

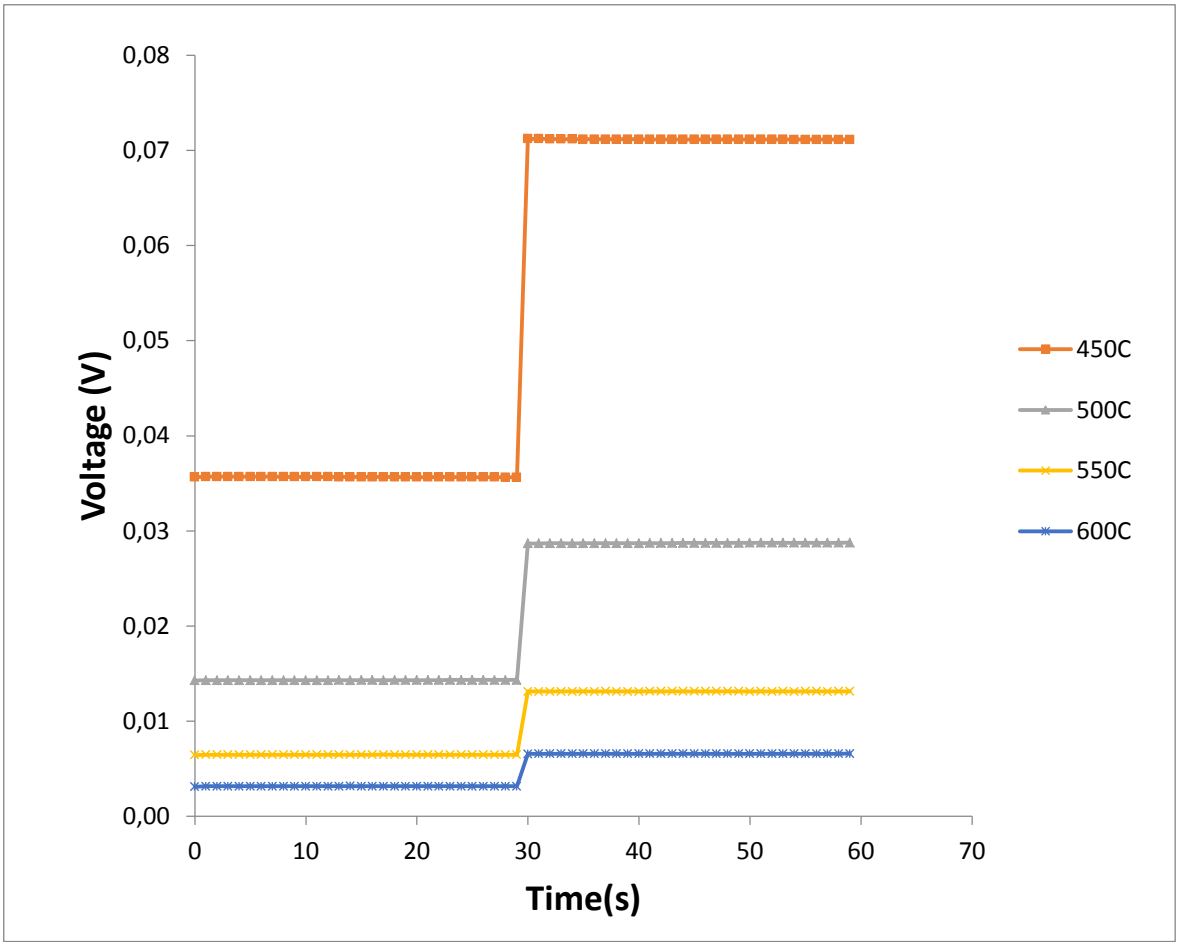

Figure 3.20. Electrical conductivity of 5MnGDC at various temperatures.

Electrical conductivity measurements of 5MnGDC at various temperatures (450°C, 500°C, 550 °C and 600 °C) are displayed in Figure 3.20. The current value is doubled after 30 seconds while the voltage value is also doubled and it can be observed on the graph clearly. For the first 30 seconds the voltage values are 0.035 V, 0.01 V, 0.006 V, 0.003 V at 450 °C, 500 °C, 600 °C respectively. For the second half, the voltage values are 0.07 V, 0.028 V, 0.013 V, 0.006 V at 450 °C, 500 °C, 600 °C respectively. As the temperature is increased, the voltage values decrease.

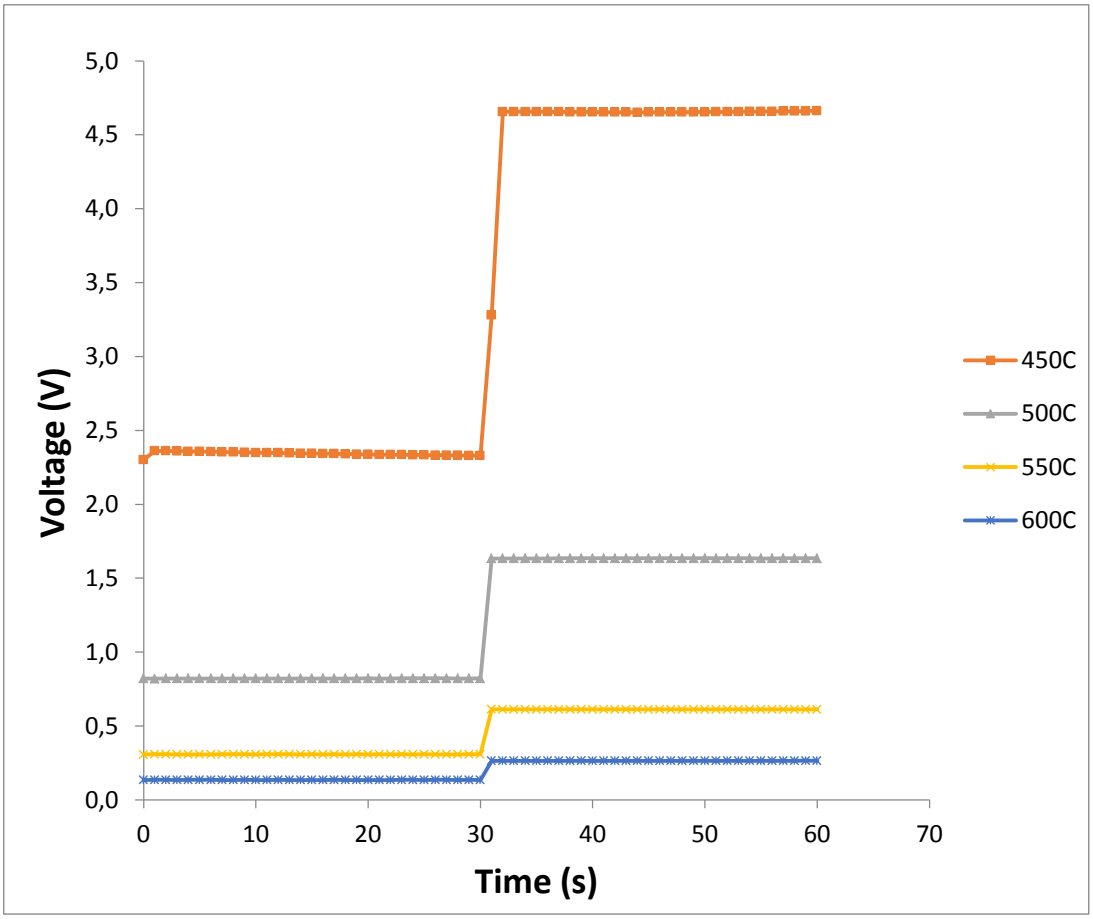

Figure 3.21. Electrical conductivity of 2VGDC at various temperatures.

Electrical conductivity measurements of 2VGDC at various temperatures (450°C, 500°C, 550 °C and 600 °C) are displayed in Figure 3.21. The current value is doubled after 30 seconds while the voltage value is also doubled and it can be observed on the graph clearly. For the first 30 seconds the voltage values are 2.24 V, 0.82 V, 0.30 V, 0.13 V at 450 °C, 500 °C, 600 °C respectively. For the second half, the voltage values are 4.66 V, 1.64 V, 0.61 V, 0.26 V at 450 °C, 500 °C, 600 °C respectively. As the temperature is increased, the voltage values decrease.

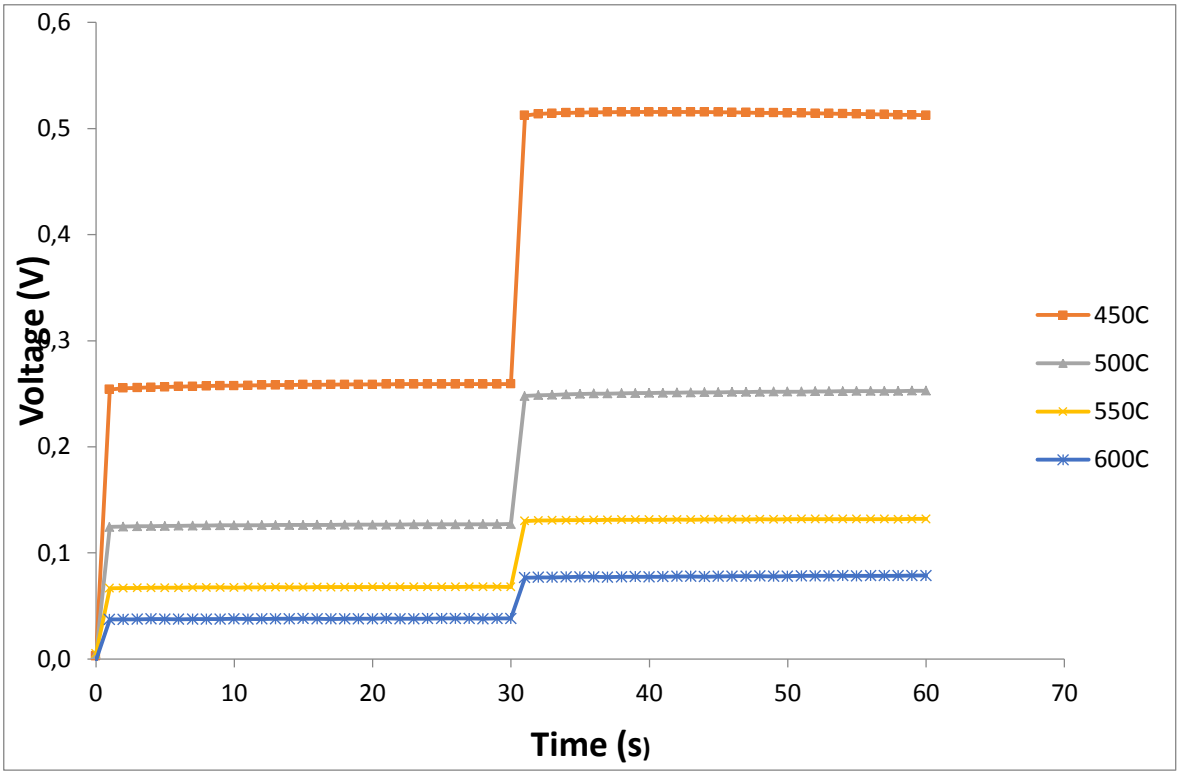

Figure 3.22. Electrical conductivity of 30TiGDC at various temperatures.

Electrical conductivity measurements of 30TiGDC at various temperatures (450°C, 500°C, 550 °C and 600 °C) are displayed in Figure 3.22. The current value is doubled after 30 seconds while the voltage value is also doubled and it can be observed on the graph clearly. For the first 30 seconds the voltage values are 1.24 V, 0.63 V, 0.42 V, 0.28 V at 450 °C, 500 °C, 550 °C and 600 °C respectively. For the second half, the voltage values are 2.V, 0.25 V, 0.13 V, 0.07 V at 450 °C, 500 °C, 600 °C respectively. As the temperature is increased, the voltage values decrease.

Table 3.1. Average conductivity data from EIS and Chronopotentiometry (CHR) tests

YSZ	400°C	450°C	500°C	550°C	600°C	650°C	700°C	750°C	800°C
Av. conductivity EIS (S/cm)	0.000004	0.000013	0.000041	0.000107	0.000195	0.000454	0.000948	0.001477	0.002283
Av. Conductivity CHR (S/cm)	0.000004	0.000018	0.000040	0.000102	0.000214	0.000630	0.000822	0.001702	0.002491
GDC									
Av. conductivity EIS (S/cm)	0.000444	0.001113	0.002381	0.004618	0.008144	0.012775	0.019953	0.028877	0.040524
Av. Conductivity CHR (S/cm)	0.001565	0.001576	0.002731	0.004667	0.008144	0.012938	0.019223	0.028485	0.045037
1VDC									
Av. conductivity EIS (S/cm)	0.000003	0.000009	0.000024	0.000049	0.000099	0.000185	0.000342	0.000185	0.001171
Av. Conductivity CHR (S/cm)	0.000006	0.000016	0.000026	0.000048	0.000148	0.000268	0.000406	0.000877	0.001302
2VGDC									
Av. conductivity EIS (S/cm)	0.000001	0.000002	0.000005	0.000017	0.000031	0.000069	0.000141	0.000272	0.000513
Av. Conductivity CHR (S/cm)	0.000001	0.000002	0.000005	0.000013	0.000029	0.000062	0.000124	0.000203	0.000247
5MnGDC									
Av. conductivity EIS (S/cm)	0.000055	0.000138	0.000340	0.000732	0.001415	0.002516	0.004136	0.006431	0.009139
Av. Conductivity CHR (S/cm)	0.000048	0.000137	0.000340	0.000736	0.001487	0.002769	0.004897	0.006836	0.008844
30TiGDC									
Av. conductivity EIS (S/cm)	0.000008	0.00237	0.000049	0.000082	0.000117	0.000124	0.000126	0.000170	0.000302
Av. Conductivity CHR (S/cm)	0.000007	0.00248	0.000050	0.000084	0.000112	0.000090	0.000137	0.000179	0.000279

The data obtained from EIS and chronopotentiometry (CHR) measurements are used to calculate the electrical conductivity of the compounds at different temperatures according to equation 1.19. The average conductivity values of the compounds from EIS and chronopotentiometry (CHR) experiments at different temperatures ranging from 400 ºC to 800 ºC are summarized in Table 3.1. It can be seen that the values obtained from EIS and CHR are very close to each other. Among the synthesized compound 5MnGDC has the highest average conductivity value, hence, it is evaluated as a good candidate for an

anode material. 2VGDC has the lowest electrical conductivity value, so it is considered as an electrolyte material.

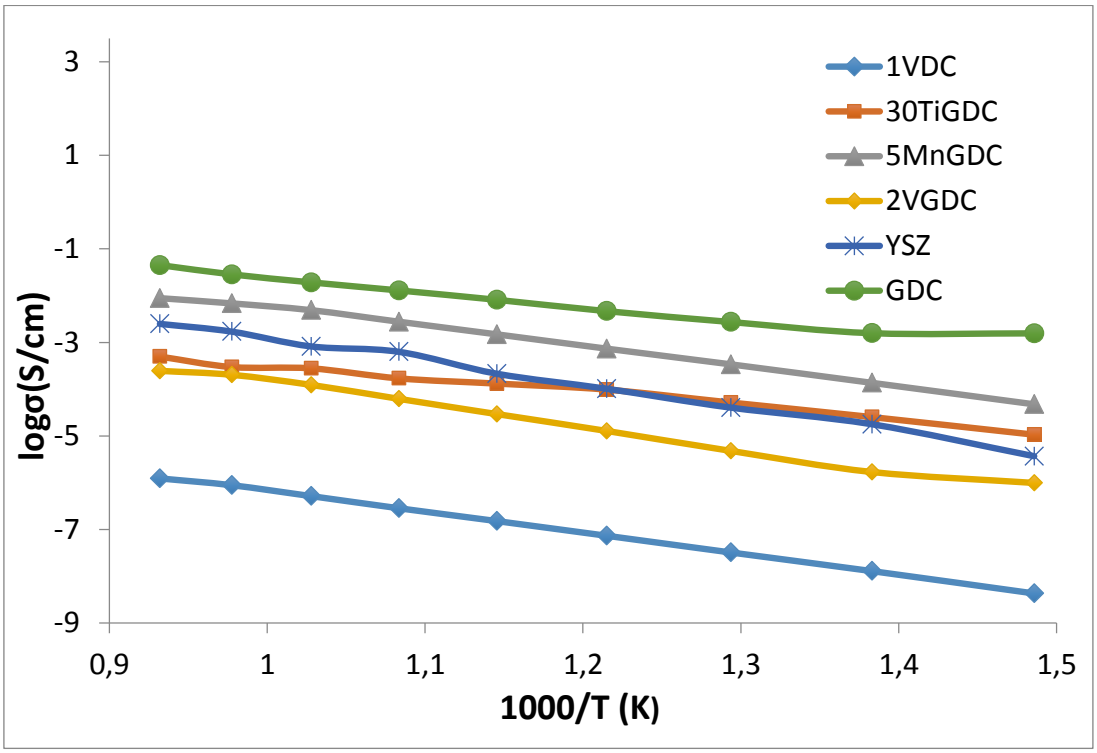

Figure 3.23. Arrhenius plot of 1VDC, 30TiGDC, 5MnGDC, 2VGDC, YSZ, GDC.

The Arrhenius plot of all the materials is illustrated in Figure 3.23. Arrhenius equation (1.20) and common logaritm of conductivity values (1.22) are used to plot this graph. The activation energies are calculated from the slope of the Arrhenius plot and are summarized in Table 3.2. 30TiGDC has the lowest activation energy (0.26eV) among the synthesized materials and its activation energy value is close to GDC (0.25eV). This means that it is electrically conductive and can be used as anode material. 2VGDC has the highest activation energy value (0.40 eV) among the synthesized materials and its activation energy value is close to YSZ (0.44 eV). It can be used as an electrolyte material because of its low electrical conductivity.

Table 3.2. Activation energies obtained from the slope of the Arrhenius plot

	1VDC	2VGDC	30TiGDC	5MnGDC	YSZ	GDC
Slope	-4.31	-4.71	-3.01	-4.19	-5.06	-2.89
Activation Energy (eV)	0.37	0.40	0.26	0.36	0.44	0.25

3.5. Ionic Conductivity Results:

The conductivity results from Four Probe Method measurements reveal that 1VDC and 2VGDC compounds have lower electrical conductivity values than 5MnGDC, 30TiGDC and GDC. Hence, these compounds are evaluated as the potential candidates for an electrolyte material. However, electrical conductivity is not the only criteria for an ideal electrolyte material; it should possess high ionic conductivity in order to transport the oxide ions from cathode to anode side. The oxygen reduction mechanism at the cathode of the SOFC has the following steps [44]:

- Oxygen molecules are adsorbed on the surface of cathode

  $0.5\ O_2\ (g) \rightarrow 0.5\ O_2\ (ad)$

- Adsorbed molecules are dissociated into oxygen atoms

  $0.5\ O_2\ (g) \rightarrow O\ (ad)$

- Oxygen is reduced to oxide (O^{-2}) ions and then incorporates into vacant sites in the oxide lattice

  $O\ (ad) + 2e^{-2} + V_O \rightarrow O_o^{\ x}$

- The overall equation of the reduction of oxygen molecules on the oxide surface followed by incorporation of oxide ions into lattice vacancies:

  $0.5O_2\ (g) + V_O \rightarrow O_o^{\ x} + 2h$

  V_O = Oxygen vacancy

O_O^x = Oxide ions in vacancy

In this section, the ionic conductivity properties of 1VDC and 2VGDC materials are tested by using EIS. Suitability of these electrolyte materials will be addressed by the contribution of these measurements.

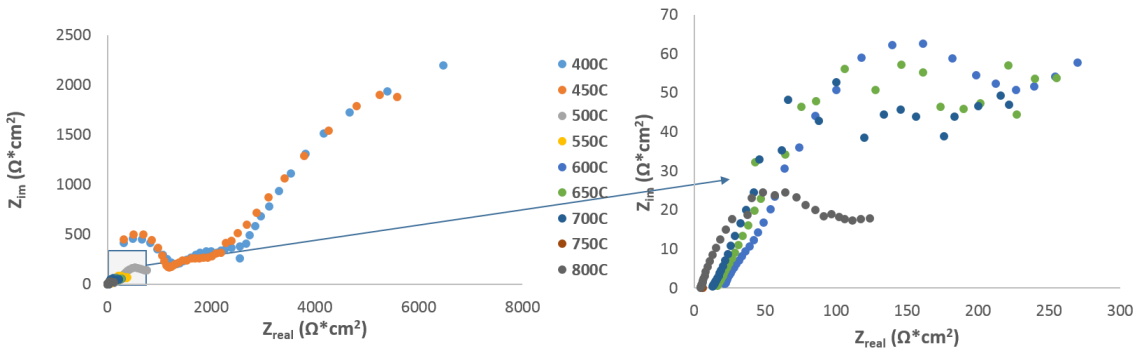

Figure 3.24. Comparison of EIS data: 1VDC fed with O3 at different temperatures between 400°C -800°C.

The EIS measurements of 1VDC symmetric cell fed with %3 Oxygen and %97 Nitrogen (O3) at various temperatures ranging from 400°C to 800°C are demonstrated in Figure 3.24. The first graph contains the EIS data collected at all temperatures and the second graph contains the EIS data collected at higher temperatures (600°C-800°C). It can be seen that the polarization resistance at low frequency range (right side of the graph), which is related to oxygen diffusion and adsorption process, decreases as temperature increases. The electrode impedance responses at low frequency are dependent on the oxygen partial pressure whereas those at high frequencies are not [45]. This is an expected result, because ions receive more thermal energy at higher temperatures, thus, their kinetic energy and mobility increase gradually. In addition, it can be observed that there are three arcs on the graph at 400°C, 450°C and 500°C. The first arc on the left-hand side corresponds to charge transfer reactions at high frequency region. The second arc corresponds to oxide ion transport from the triple phase boundary to the electrolyte at intermediate frequency region. The third arc is related with gas diffusion and adsorption along the cathode surface at low frequency region [46-48]. At temperatures higher than

500°C, two arcs are observed at high frequency. As temperature is increased, oxide ion (O^{-2}) mobility is increased and ion transport is favored. The first arc related to charge transport processes at the interface disappears so that it cannot be distinguished from the second arc after 500°C [49]. Hence, at 550°C, 1VDC is activated for ion transport and it can be used as an electrolyte at this temperature.

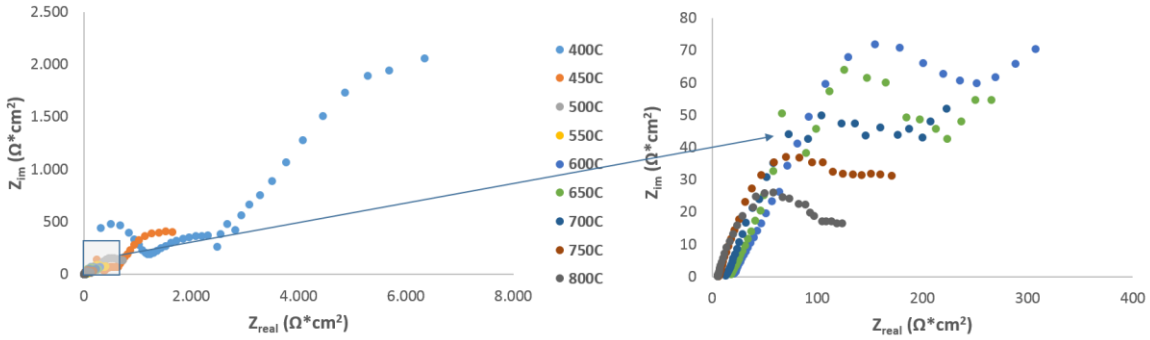

Figure 3.25. Comparison of EIS data: 1VDC fed with O10 at different temperatures between 400°C -800°C.

The EIS measurements of 1VDC symmetric cell fed with %10 Oxygen and %90 Nitrogen (O10) between temperatures 400°C and 800°C is displayed in Figure 3.25. The first graph contains the EIS data collected at all temperatures and the second graph contains the EIS data collected at high temperatures (600°C-800°C). The polarization resistance at low frequency range decreases as temperature is increased because the rate of oxygen diffusion and adsorption processes enhances. It is observed that there are three arcs on the graph at 400°C, 450°C and 500°C. At temperatures higher than 500°C, two arcs are present at high frequency region. As temperature is increased, oxide ion (O^{-2}) mobility is increased and ion transport is favored. The first arc related to charge transfer reactions diminishes after 500°C. Hence, at 550°C, 1VDC is activated for ion transport and it can be used as an electrolyte at this temperature.

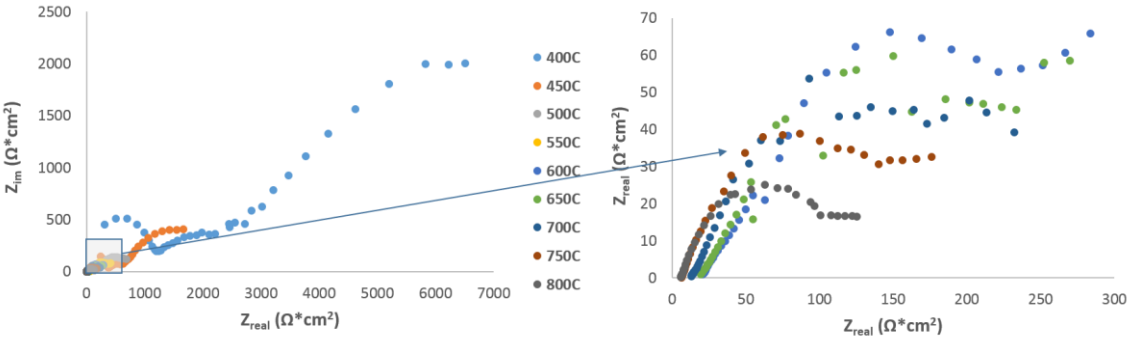

Figure 3.26. Comparison of EIS data: 1VDC fed with O20 at different temperatures between 400°C -800°C.

The EIS measurements of 1VDC symmetric cell fed with %20 Oxygen and %80 Nitrogen (O20) at various temperatures ranging from 400°C to 800°C can be seen in Figure 3.26. The results of EIS measurements at all temperatures are exhibited in the first graph and the EIS data obtained between 600°C and 800°C is present in the second graph. The polarization resistance at low frequency range, which is related to oxygen diffusion and adsorption process, gets smaller as temperature is increased gradually. This occurs due to the increase of kinetic energy of the oxygen and oxide ions (O^{-2}). On the other hand, it is obvious that there are three arcs on the graph at 400°C, 450°C and 500°C. At temperatures higher than 500°C, two arcs are observed at high frequency. As temperature is raised, oxide ion (O^{-2}) mobility is increased thus, ion transport is easier. The first arc related charge transfer reactions gets so small that it cannot be distinguished from the second arc after 500°C. As a result, at 550°C, 1VDC is activated and it can be used as an electrolyte at this temperature.

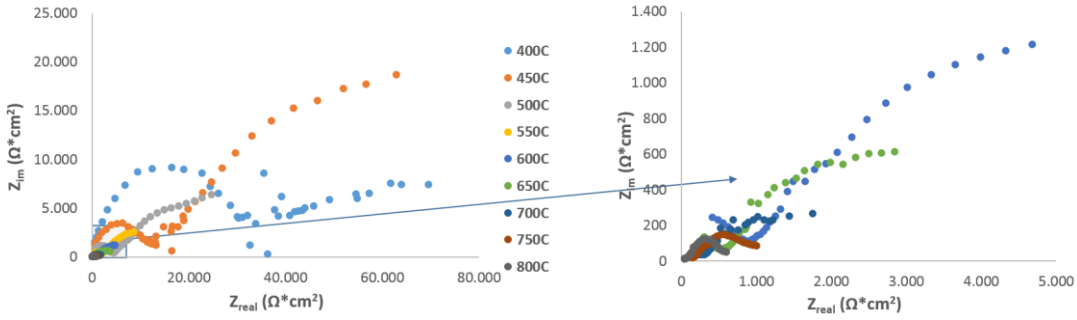

Figure 3.27. Comparison of EIS data: 2VGDC fed with O3 at different temperatures between 400°C -800°C.

The EIS measurements of 2VGDC symmetric cell fed with %3 Oxygen and %97 Nitrogen (O3) at temperatures ranging from 400°C to 800°C is demonstrated in Figure 3.27. The first graph consists of the EIS data collected at all temperatures and the second graph consists of the EIS data collected at high temperatures (600°C-800°C). As demonstrated in 1VDC EIS graphs, polarization resistance at low frequency range, which is related to cathode properties of the cell (adsorption and diffusion of oxygen in the air) gets smaller as temperature is increased. The ions receive more thermal energy at higher temperatures and their mobility is increased. In addition, it can be observed that two arcs appear on the graph between temperatures 400°C to 700°C. First arc is related to the resistance of charge transport reactions. The second arc is related to gas diffusion along the cathode surface at low frequency region. At temperatures higher than 700°C, only one arc is observed at high frequency. As temperature is increased, oxide ion (O^{-2}) mobility and charge transfer reactions rate is increased. Therefore, the first arc related to oxide ion transport and charge transfer gets so small that it cannot be distinguished from the second arc after 700°C. Hence, at 750°C, 2VGDC conducts oxide ions (O^{-2}) efficiently and can be used as an electrolyte at this temperature.

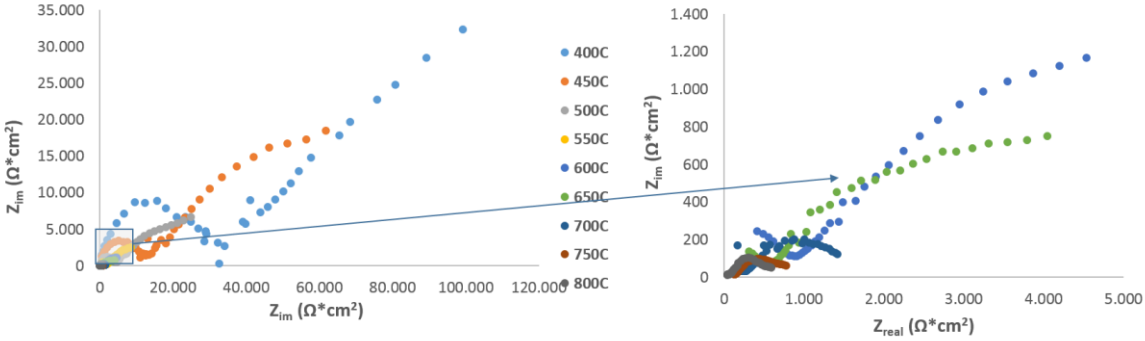

Figure 3.28. Comparison of EIS data: 2VGDC fed with O10 at different temperatures between 400°C -800°C.

The EIS measurements of 2VGDC symmetric cell fed with %10 Oxygen and %90 Nitrogen (O10) at various temperatures ranging from 400°C to 800°C is displayed in Figure 3.28. The first graph contains the EIS data collected at all different temperatures and the second graph contains the EIS data collected at high temperatures (600°C-800°C). The polarization resistance at low frequency range, decreases as temperature is increased as pointed out in the previous examples. In addition, two arcs appear on the graph between

temperatures 400°C and 700°C. At temperatures higher than 700°C, only one arc is observed at high frequency. As temperature is increased, oxide ion (O^{-2}) mobility and charge transfer reaction rate is also increased. Therefore, the first arc related to oxide ion transport and charge transfer reactions gets so small that it cannot be distinguished from the second arc after 700°C. Hence, at 750°C, 2VGDC is suitable material as an electrolyte at this temperature.

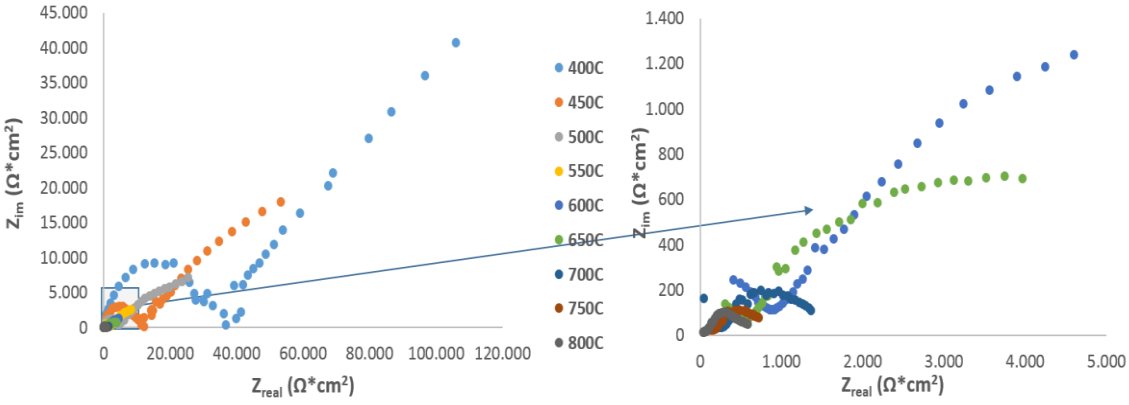

Figure 3.29. Comparison of EIS data: 2VGDC fed with O20 at different temperatures between 400°C -800°C.

The EIS measurements of 2VGDC symmetric cell fed with %20 Oxygen and %80 Nitrogen (O20) at various temperatures between 400°C to 800°C is seen in Figure 3.29. The first graph contains the EIS data collected at all temperatures and the second graph contains the EIS data collected at high temperatures (600°C-800°C). As expected, the polarization resistance at low frequency range decreases as temperature is increased. Two arcs appear on the EIS graph between temperatures 400°C and 700°C. At higher temperatures, only one arc is observed which is present at high frequency region. The first arc at lower temperatures which is related to oxide ion transport and charge transfer reactions gets so small that it cannot be distinguished from the second arc after 700°C. Therefore, at 750°C, 2VGDC is active for ion transport and it can be used as an electrolyte at this temperature.

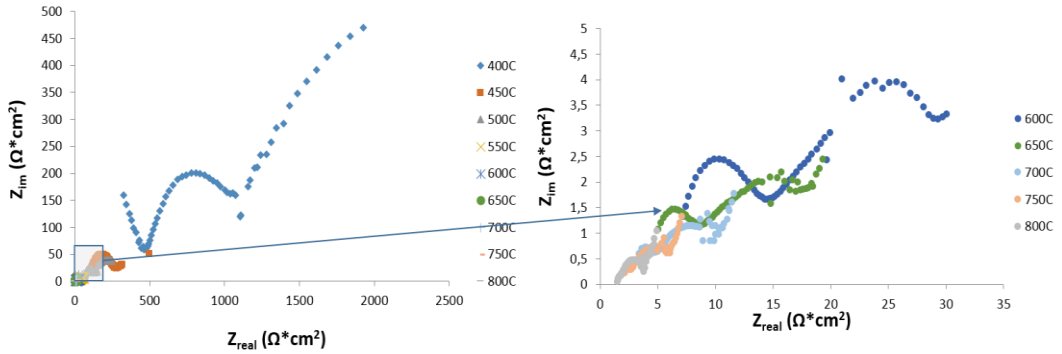

Figure 3.30. Comparison of EIS data: YSZ fed with O3 at different temperatures between 400°C -800°C.

The EIS measurements of YSZ symmetric cell fed with %3 Oxygen and %97 Nitrogen (O3) at various temperatures ranging from 400°C to 800°C is demonstrated in Figure 3.30. The first graph contains the data collected at all temperatures and the second graph contains the data collected at high temperatures (600°C-800°C). It is clear that the polarization resistance at low frequency range, which is related to oxygen diffusion and adsorption process, is reduced as temperature is increased. It is known that ions receive more thermal energy at higher temperatures, so they are driven for transportation through the electrolyte. In addition, it is seen that there are three arcs on the graph at temperatures up to 750°C, however, the third arc is hardly noticeable at 600°C, 650°C, 700°C. The first and second arcs at 750°C and 800°C are not distinguishable and two arcs are observed. As stated previously for 1VDC, the first arc on the left-hand side occurs due to charge transfer reactions at high frequency region. The second arc is related to oxide ion (O^{-2}) transport at intermediate frequency region. The third arc is present due to gas diffusion along the cathode surface at low frequency region. Oxide ion (O^{-2}) mobility is enhanced, ion transport is favored and charge transfer reactions become faster. Therefore, the first arc is combined with the second arc at 750°C and 800°C. YSZ is suitable for ion transport at 750°C and it can be used as an electrolyte at this temperature [50].

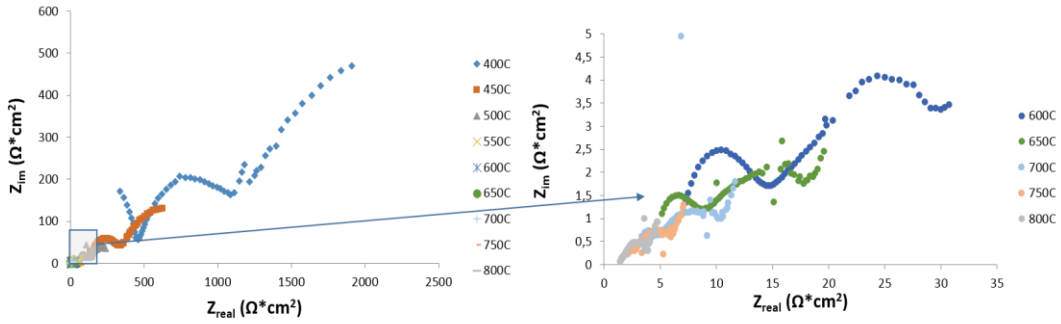

Figure 3.31. Comparison of EIS data: YSZ fed with O10 at different temperatures between 400°C -800°C.

The EIS measurements of YSZ symmetric cell fed with %10 Oxygen and %90 Nitrogen (O10) at various temperatures ranging from 400°C to 800°C is exhibited in Figure 3.31. The first graph demonstrates the EIS data collected at all different temperatures and the second graph demonstrates the EIS data collected at high temperatures (600°C-800°C). It is obvious that the polarization resistance at low frequency range decreases when temperature is increased gradually. This is an expected result, because ions receive more thermal energy at higher temperatures, thus, their kinetic energy and mobility is enhanced. There are mostly three arcs at different temperatures, however, the third arc is hardly noticeable at 600°C, 650°C, 700°C. At 750°C and 800°C, instead of three arcs, two arcs are present on the graph due to the fact that the first and second arcs are combined together. At higher temperatures, the resistance of charge transfer reactions gets smaller and therefore, the first arc is combined with the second arc at 750°C and 800°C. As a result, at 750°C, YSZ is active for ion transport and it can be used as an electrolyte at this temperature.

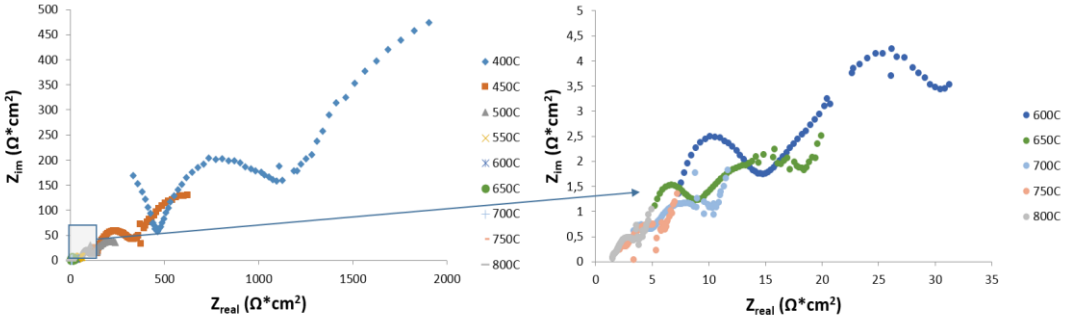

Figure 3.32. Comparison of EIS data: YSZ fed with O20 at different temperatures between 400°C -800°C.

The EIS measurements of YSZ symmetric cell fed with %20 Oxygen and %80 Nitrogen (O20) at various temperatures ranging from 400°C to 800°C is displayed in Figure 3.32. The EIS data collected at all different temperatures is presented in the first graph and the EIS data collected at high temperatures (600°C-800°C) is presented in the second graph. It is clearly seen that the polarization resistance at low frequency range decreases when temperature is increased. In general, three arcs can be seen on the graphs, however, the third arc is hardly noticeable at 600°C, 650°C, 700°C. At 750°C and 800°C, instead of three arcs, two arcs are seen on the graph due to the fact that, the first and second arcs are combined together. At higher temperatures, the first arc related to charge transfer reactions gets smaller and is combines with the second arc at 750°C and 800°C. Hence, at 750°C, YSZ is activated and it can be used as an electrolyte at this temperature.

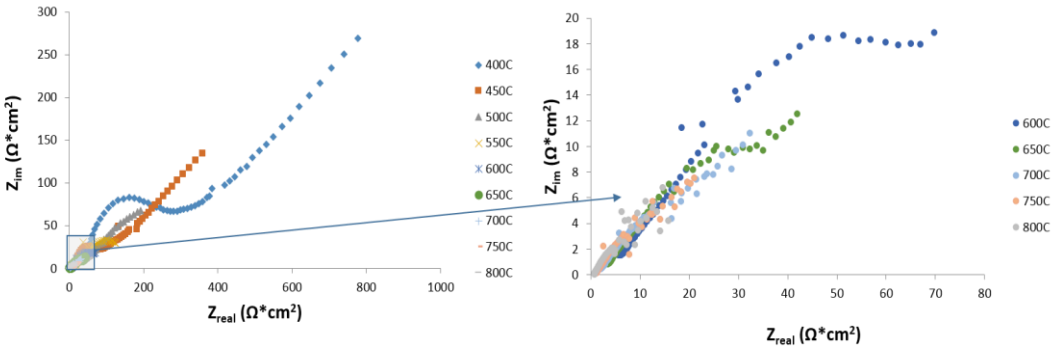

Figure 3.33. Comparison of EIS data: GDC fed with O3 at different temperatures between 400°C -800°C.

The EIS measurements of GDC symmetric cell fed with %3 Oxygen and %97 Nitrogen (O3) at various temperatures ranging from 400°C to 800°C is demonstrated in Figure 3.33. The first graph contains the data collected at all different temperatures and the second graph contains the data collected at high temperatures (600°C-800°C). It is known the polarization resistance at low frequency range is due to oxygen diffusion and

adsorption processes. It decreases as temperature is increased due to increased mobility of the ions. It is seen that two arcs appear on the graph between temperatures 400°C to 650°C. As stated before for 2VGDC, first arc is related to oxide ion (O^{-2}) transport from triple phase boundry to the electrolyte and charge transfer reactions. The second arc is related to gas diffusion and surface exchange reactions on cathode surface at low frequency region. At temperatures higher than 650°C, only one arc is observed at high frequency region. The oxide ion (O^{-2}) mobility and charge transfer reaction rate is enhanced when temperature is increased. Therefore, the first arc cannot be distinguished from the second arc after 650°C. Hence, at 700°C, GDC is conducts oxide ions (O^{-2}) efficiently and it can be used as an electrolyte at this temperature.

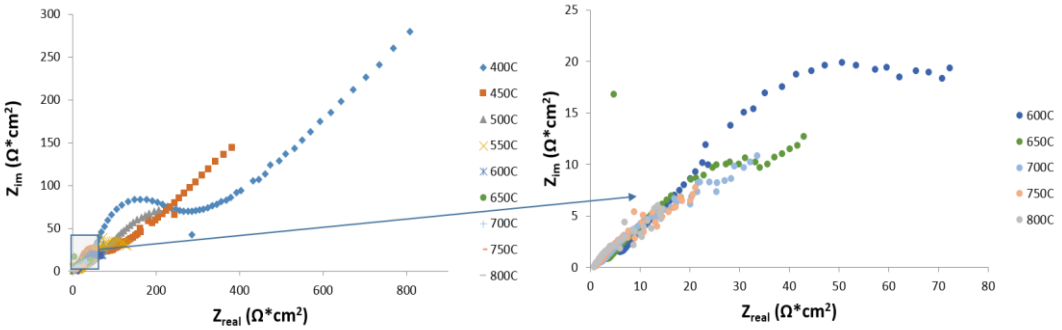

Figure 3.34. Comparison of EIS data: GDC fed with O10 at different temperatures between 400°C -800°C.

The EIS measurements of GDC symmetric cell fed with %10 Oxygen and %90 Nitrogen (O10) at various temperatures ranging from 400°C to 800°C is displayed in Figure 3.34. The first graph consists of EIS data collected at all different temperatures and the second graph consists of EIS data collected at high temperatures (600°C-800°C). The polarization resistance is smaller at high temperatures like the previous examples. Two arcs appear on the graph between temperatures 400°C to 650°C. Above 650°C, only one arc is observed at high frequency. As temperature is increased, oxide ion (O^{-2}) mobility and charge transfer reactions rate is increased. Therefore, the first and second arc combine

above 650°C. Hence, at 700°C, GDC is activated for ion transport and it can be used as an electrolyte at this temperature.

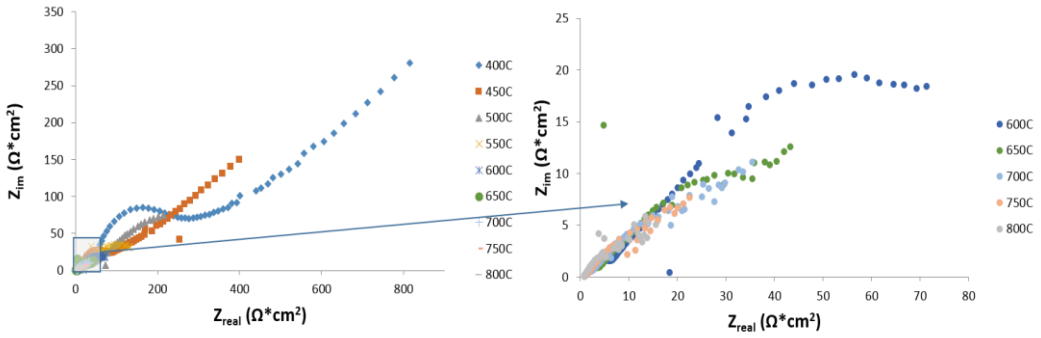

Figure 3.35. Comparison of EIS data: GDC fed with O20 at different temperatures between 400°C -800°C.

The EIS measurements of GDC symmetric cell fed with %20 Oxygen and %80 Nitrogen (O20) at various temperatures ranging from 400°C to 800°C is shown in Figure 3.35. The first graph contains the data collected at all different temperatures and the second graph contains the data collected at high temperatures (600°C-800°C). The polarization resistance is smaller at high temperatures due to the enhancement of ion mobility and charge transfer reactions rate, as stated in the previous examples. Two arcs are seen on the graph between 400°C to 650°C and above 650°C, only one arc is observed at high frequency. The first arc related to oxide ion transport and charge transfer reactions combines with the second arc above 650°C. Hence, at 700°C, GDC is activated and it can be used as an electrolyte at this temperature.

O3, O10, O20 EIS results of 1VDC are compared at 400°C in Figure 3.36. The polarization arc at low frequency region is altered due to different oxygen compositions. At this region, gas diffusion and adsorption processes are dominant instead of charge transfer reactions and ionic conductivity. Thus, the change in low frequency arc (concentration polarization arc) solely depends on cathode characteristics and oxygen partial pressure does not have much impact on this region [51]. It is observed that the arcs at high frequency region and intermediate frequency region are independent of the oxygen partial

pressure but still slight differences occur at this region with different oxygen compositions. It is clear that oxide ion transport mechanism is mainly dominated by cathode surface exchange reactions. In addition, polarization resistance increases when oxygen percent is reduced because the oxygen gas diffusion resistance enhanced. [52-54]. At low frequency, it can be interpreted that O3 has the highest polarization resistance and O20 has the lowest. Since it is obviously seen that the oxygen gas diffusion resistance is higher than YSZ (Figure 3.30, Figure 3.31 and Figure 3.32), 1VDC does not have better oxide ion conductivity than YSZ. These results show that this compound does not supply enough oxide ion around 400°C.

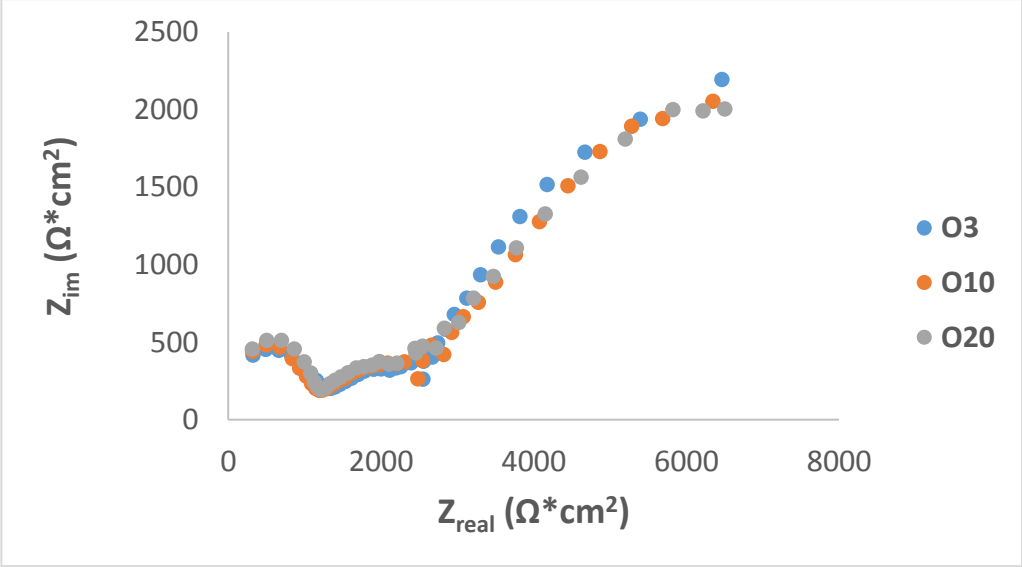

Figure 3.36. Comparison of EIS data: 1VDC fed with O3, O10, O20 at 400 °C.

O3, O10, O20 EIS results of 1VDC are compared at 450°C in Figure 3.37. The polarization arcs at low frequency region are altered due to different oxygen compositions. As stated before, gas diffusion and adsorption processes are dominant at this region and the concentration polarization arc solely depends on cathode characteristics. The arcs at high and intermediate frequency are not affected much under these circumstances. At low frequency, it can be interpreted that O3 has lower polarization resistance than O10 and O20, though, this difference is not very obvious. The oxygen gas diffusion resistance is

reduced a little but still some improvement is required for better oxide conductivity at this temperature.

.

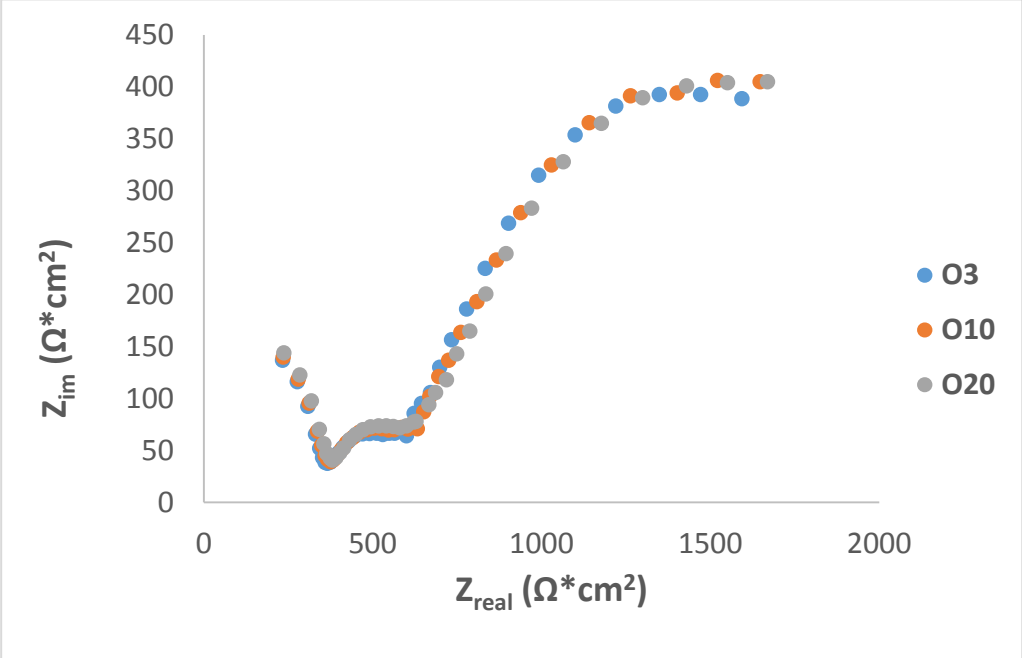

Figure 3.37. Comparison of EIS data: 1VDC fed with O3, O10, O20 at 450 °C.

O3, O10, O20 EIS results of 1VDC are exhibited at 500°C in in Figure 3.38. The concentration polarization arcs are changed due to different oxygen compositions. As stated before, oxygen gas diffusion and adsorption processes occur at this region and the concentration polarization arc solely depends on cathode characteristics. The arcs at high and intermediate frequency change slightly under these circumstances. At low frequency, it can be interpreted that O3 has the highest polarization resistance and O20 has the lowest. Therefore, the gas diffusion resistance is dominant for 1VDC and it does not conduct enough oxide ion at this temperature.

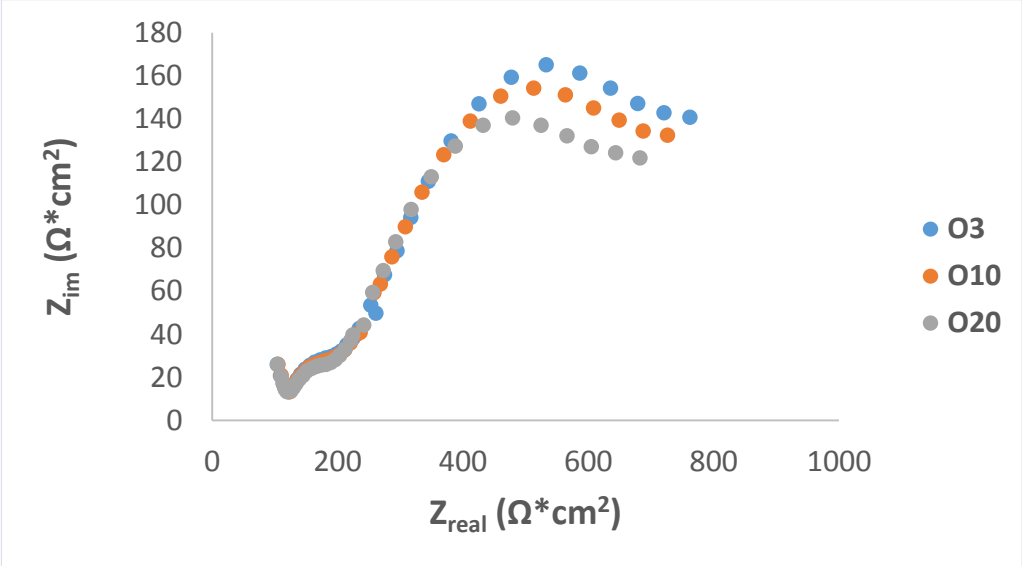

Figure 3.38. Comparison of EIS data: 1VDC fed with O3, O10, O20 at 500 °C.

O3, O10, O20 EIS results of 1VDC are compared at 550°C in Figure 3.39. The concentration arcs are altered due to different oxygen compositions. As stated before, the concentration polarization arc mainly depends on cathode characteristics. It is obvious that the arcs at high and intermediate frequency do not change much due to the fact that electrolyte properties have effect at these regions. At low frequency, it can be seen that O3 has lower polarization resistance than O10 and O20. The oxygen gas diffusion resistance is reduced, hence, 1VDC supplies enough oxygen ion at 550°C.

O3, O10, O20 EIS results of 1VDC are illustrated at 600°C in Figure 3.40. The concentration arcs are altered when oxygen partial pressure is changed. As stated before, cathode properties effect the concentration polarization arc whereas electrolyte properties effect the other regions. At low frequency, it can be seen that O3 has the lowest concentration polarization resistance and O20 has the highest. The oxygen gas diffusion resistance is reduced, hence, 1VDC supplies enough oxygen ion at 600°C.

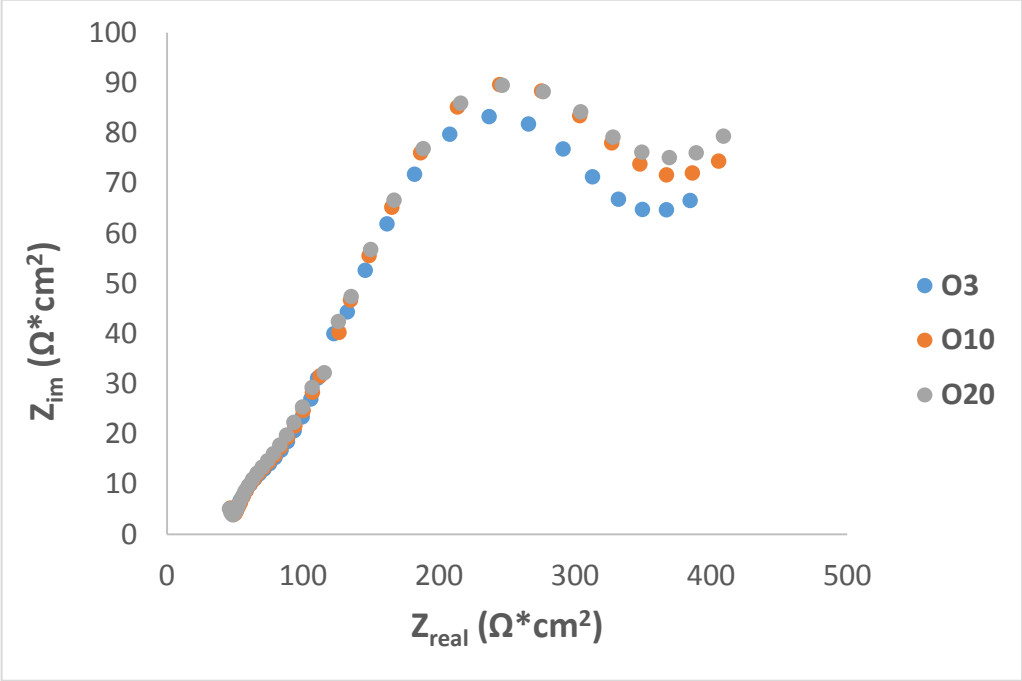

Figure 3.39. Comparison of EIS data: 1VDC fed with O3, O10, O20 at 550 °C.

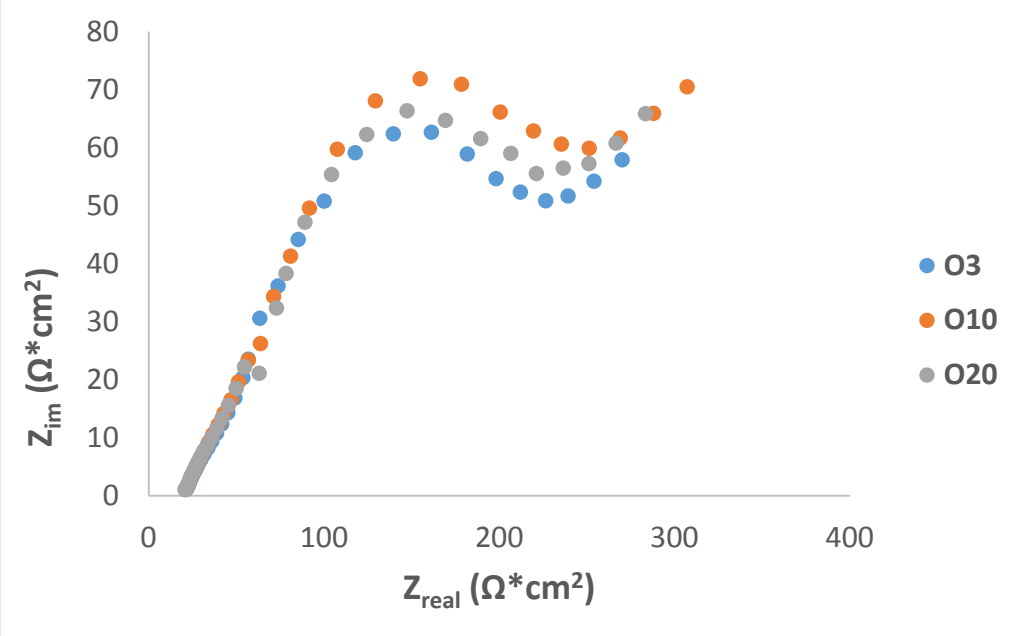

Figure 3.40. Comparison of EIS data: 1VDC fed with O3, O10, O20 at 600 °C.

O3, O10, O20 EIS results of 2VGDC are compared at 400°C in Figure 3.41. The concentration arc is altered due to different oxygen compositions similar to 1VDC. Gas diffusion and adsorption processes on the surface of the cathode are dominant at this region, hence, the concentration polarization arc solely depends on cathode characteristics. The high frequency arc is not changed much at various oxygen partial pressures. At low frequency, it is illustrated that O3 has the lowest polarization resistance and O20 has the highest. Though, the polarization resistance values are very high compared to YSZ and GDC so oxygen permeability is minimum at this temperature.

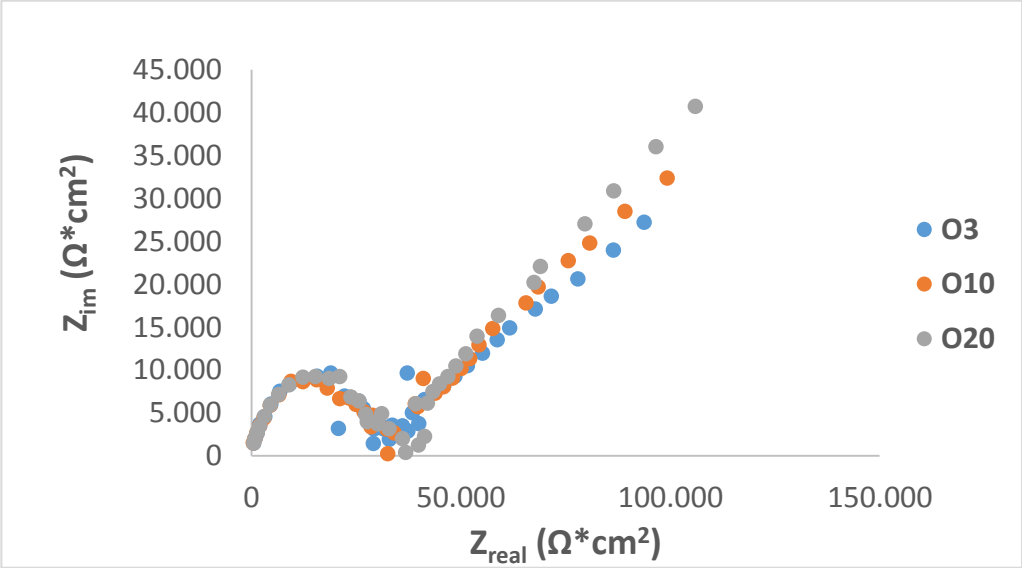

Figure 3.41. Comparison of EIS data: 2VGDC fed with O3, O10, O20 at 400 °C.

O3, O10, O20 EIS results of 2VGDC are exhibited at 450°C in Figure 3.42. In the previous examples, the concentration arcs are affected by different oxygen partial pressures, however, in this experiment, both high frequency and low frequency arcs remain almost the same under these conditions. According to these results, the cathode and electrolyte properties do not change much as oxygen percentage is increased at this temperature.

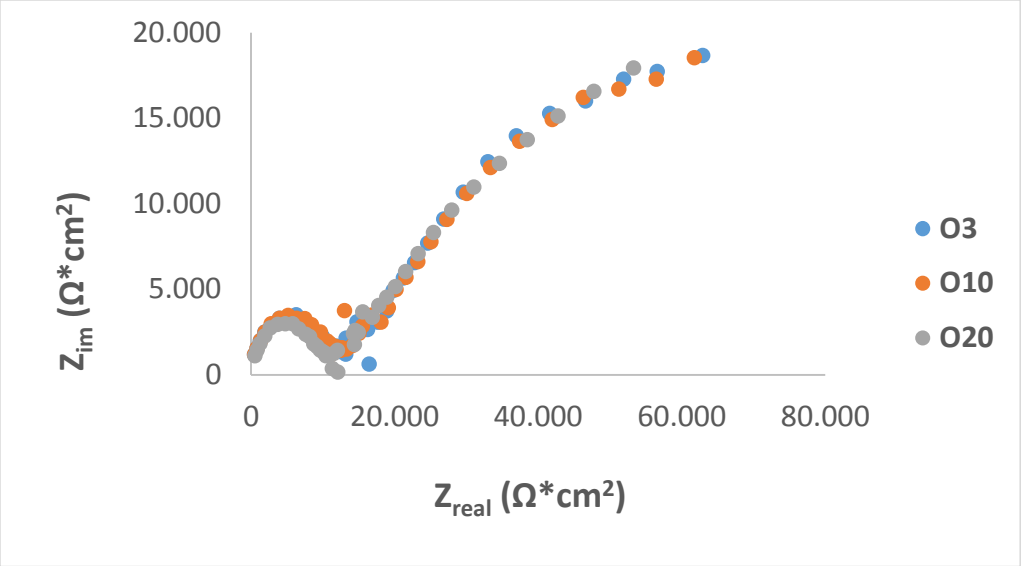

Figure 3.42. Comparison of EIS data: 2VGDC fed with O3, O10, O20 at 450 °C.

O3, O10, O20 EIS results of 2VGDC are compared at 500°C in Figure 3.43. At low frequency, it can be seen that O20 has the highest polarization resistance and O3 has the lowest. This material is resistive to oxide ion conductivity because the polarization resistance goes up when the oxide percent is increased in the feed and the real impedance values are higher compared to the conventional electrolyte materials YSZ and GDC.. These results show that this compound is not active for oxide ion transport at 500°C.

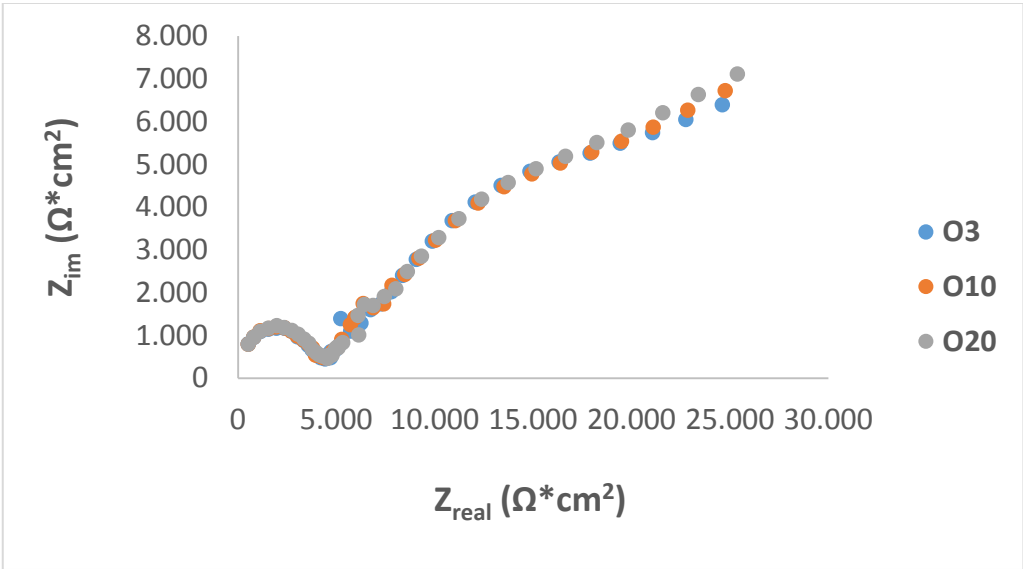

Figure 3.43. Comparison of EIS data: 2VGDC fed with O3, O10, O20 at 500 °C.

O3, O10, O20 EIS results of 2VGDC are shown at 550°C in Figure 3.44. Both high frequency and low frequency arcs remain the same at different oxygen partial pressures. According to these results, the oxygen percentage in the feed does not affect the the cathode and electrolyte properties. The real impedance values are much more lower than the valueas at 450°C and 500°C, therefore ionic conductivity improves at higher temperatures but still it is high compared to YSZ (Figure 3.47.)

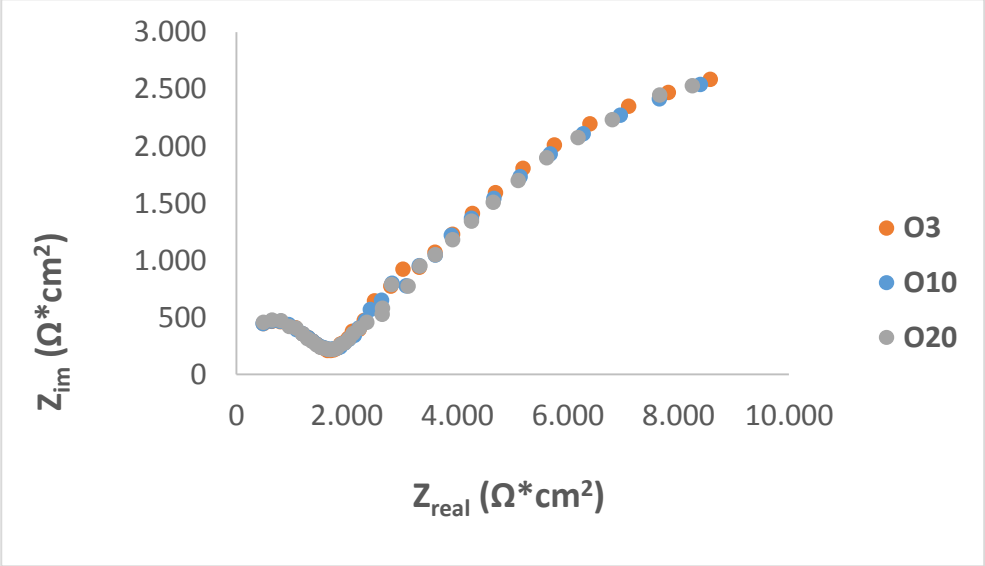

Figure 3.44. Comparison of EIS data: 2VGDC fed with O3, O10, O20 at 550 °C.

O3, O10, O20 EIS results of 2VGDC are illustrated at 600°C In Figure 3.45. Both high frequency and low frequency arcs remain the same at different oxygen partial pressures. According to these results, the oxygen percentage in the feed does not affect the the cathode and electrolyte properties. The real impedance values are high compared to YSZ at this temperature (Figure 3.48.) so ionic conductivity properties may not be sufficient for oxide ion transport at this temperature.

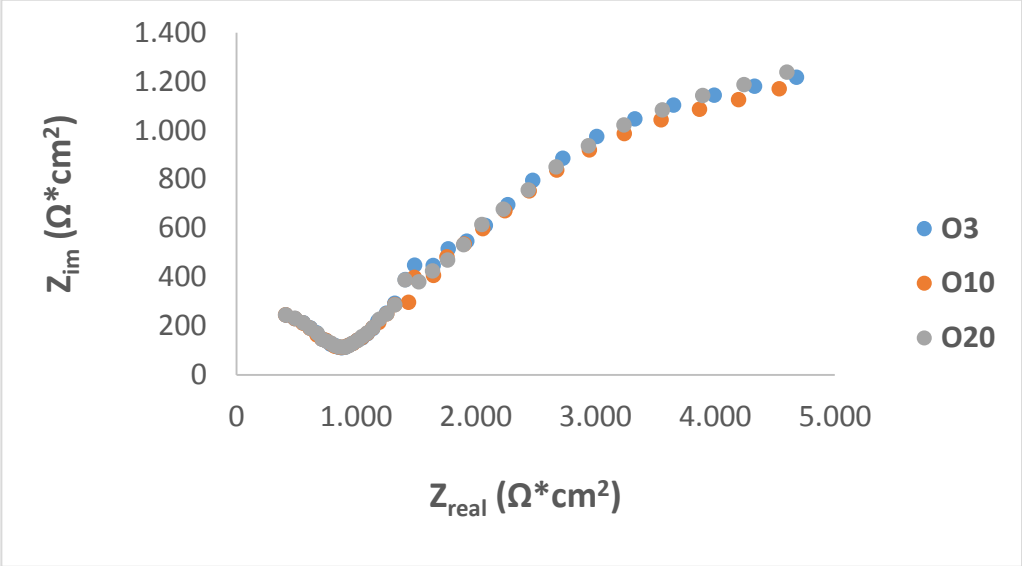

Figure 3.45. Comparison of EIS data: 2VGDC fed with O3, O10, O20 at 600°C.

O3, O10, O20 EIS results of YSZ are illustrated at 500°C in Figure 3.46. Similar to 2VGDC, the concentration arcs are not affected by different oxygen partial pressures and the arcs at high frequency and low frequency remain almost the same under these conditions. According to these results, the cathode and electrolyte properties do not change much as oxygen percentage is increased at 500°C.

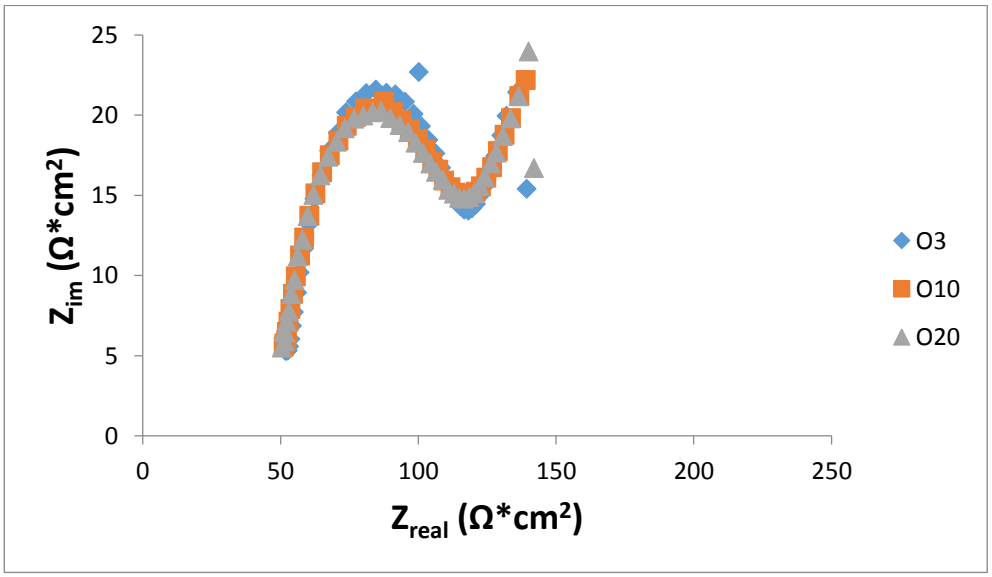

Figure 3.46. Comparison of EIS data: YSZ fed with O3, O10, O20 at 500 °C.

O3, O10, O20 EIS results of YSZ are compared at 550°C in Figure 3.47. The concentration arc is not affected by different oxygen partial pressures and the arcs at high frequency and low frequency remain almost the same under these conditions. According to these results, the cathode and electrolyte properties do not change much as oxygen percentage is increased at this temperature.

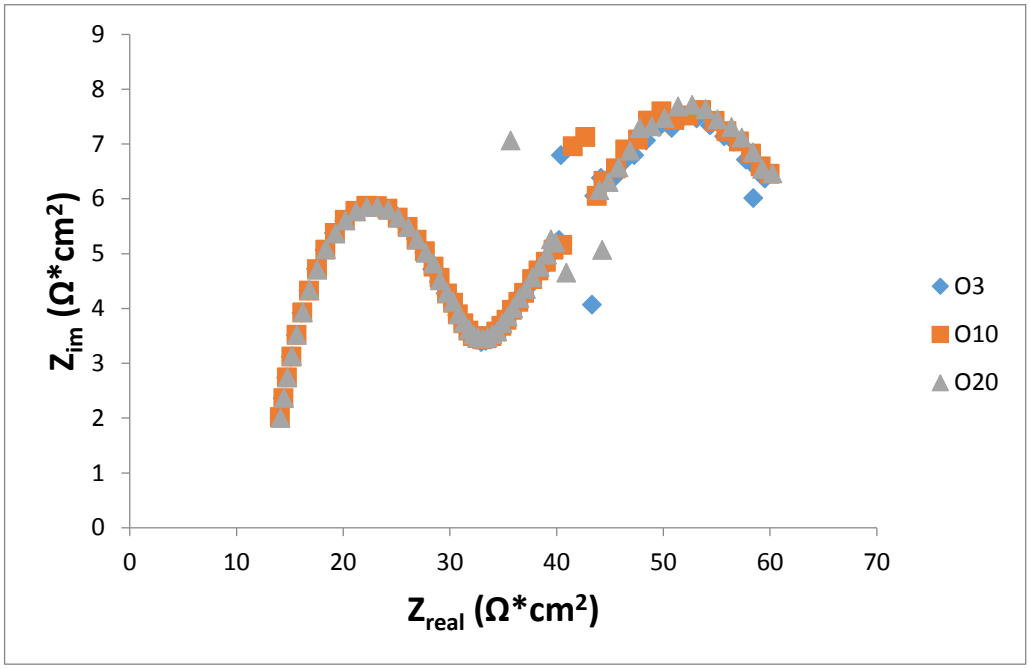

Figure 3.47. Comparison of EIS data: YSZ fed with O3, O10, O20 at 550 °C.

O3, O10, O20 EIS results of YSZ are shown at 600°C in Figure 3.48. The concentration arc is not affected by different oxygen partial pressures and the polarization arcs remain almost the same at this temperature. According to these results, the cathode and electrolyte properties do not change much as oxygen percentage is increased at 600°C.

O3, O10, O20 EIS results of GDC are exhibited and compared at 500°C in Figure 3.49. The concentration arcs are not affected by different oxygen partial pressures and the arcs at high frequency and low frequency remain almost the same under these conditions. The polarization resistance values are similar to YSZ (Figure 3.47). According to these

results, GDC ionic conductivity is similar to YSZ and the cathode and electrolyte properties do not change much as oxygen percentage is changed at this temperature.

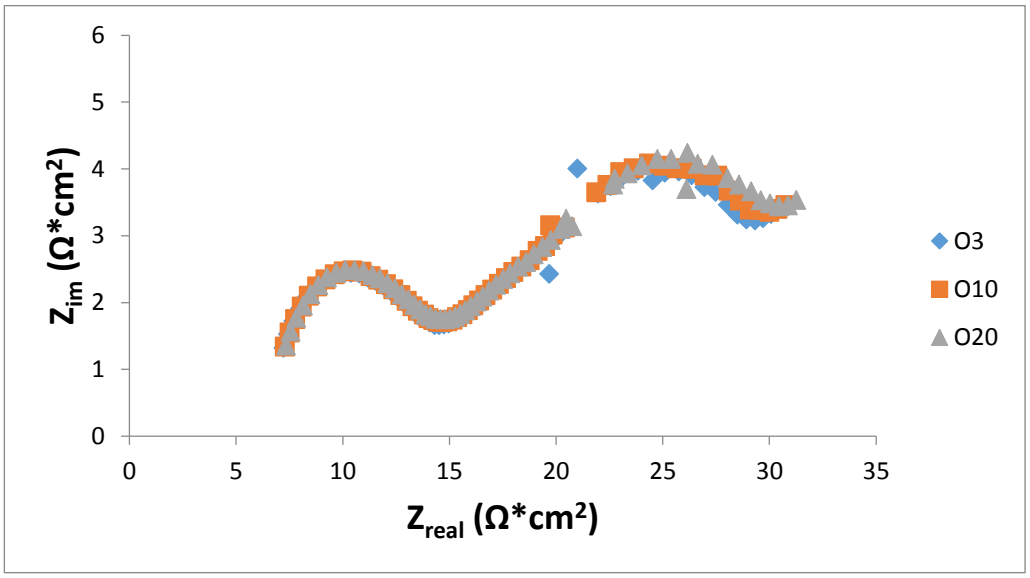

Figure 3.48. Comparison of EIS data: YSZ fed with O3, O10, O20 at 600 °C.

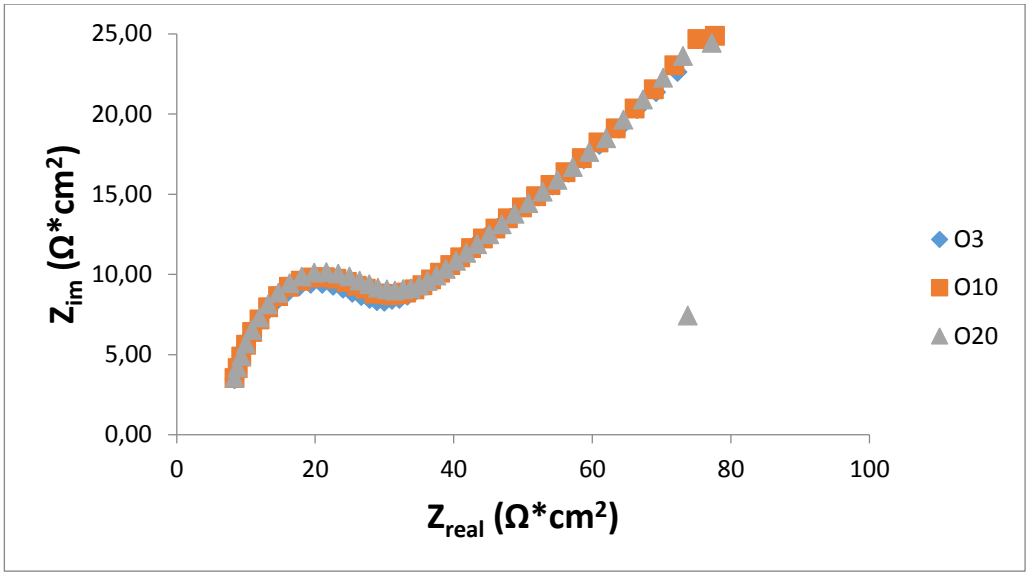

Figure 3.49. Comparison of EIS data: GDC fed with O3, O10, O20 at 500 °C

O3, O10, O20 EIS results of GDC are shown at 550°C in Figure 3.50. The concentration arc is not affected by different oxygen partial pressures and the arcs at high frequency and low frequency remain almost the same under these conditions. The polarization resistance values are similar to YSZ (Figure 3.48). These results show that GDC ionic conductivity is similar to YSZ and the cathode and electrolyte properties do not change much as oxygen percentage is changed at this temperature.

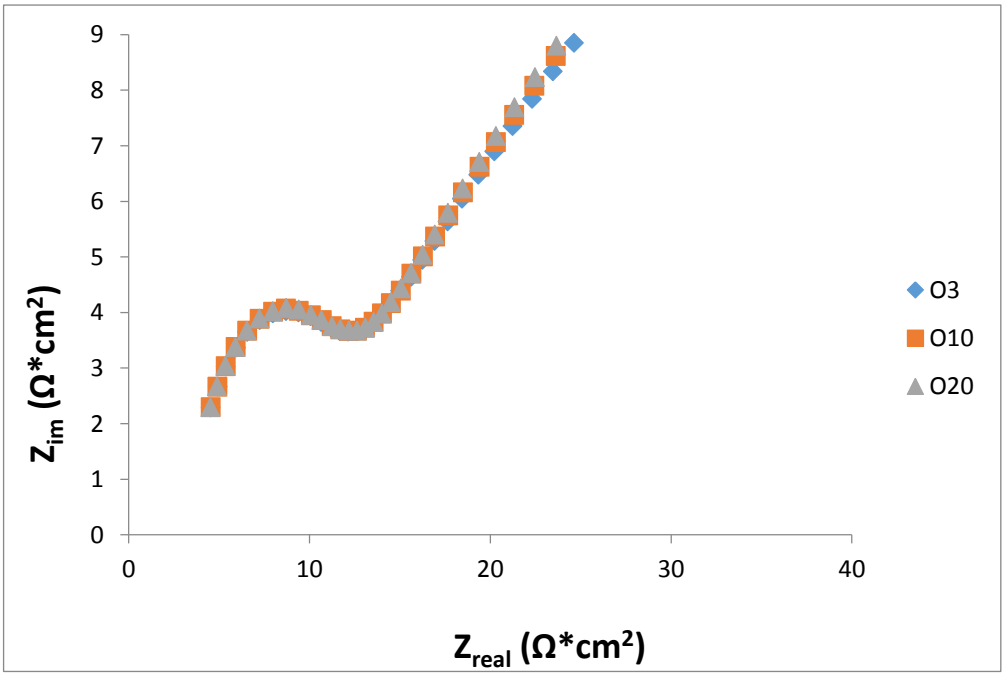

Figure 3.50. of EIS data: GDC fed with O3, O10, O20 at 550 °C.

O3, O10, O20 EIS results of GDC are illustrated at 600°C in Figure 3.51. The concentration arc is not affected by different oxygen partial pressures and the arcs at high frequency and low frequency remain almost the same under these conditions. The polarization resistance values are similar to YSZ (Figure 3.48). It is obvious that GDC's ionic conductivity is similar to YSZ and the cathode and electrolyte properties do not change much as oxygen percentage is altered at this temperature.

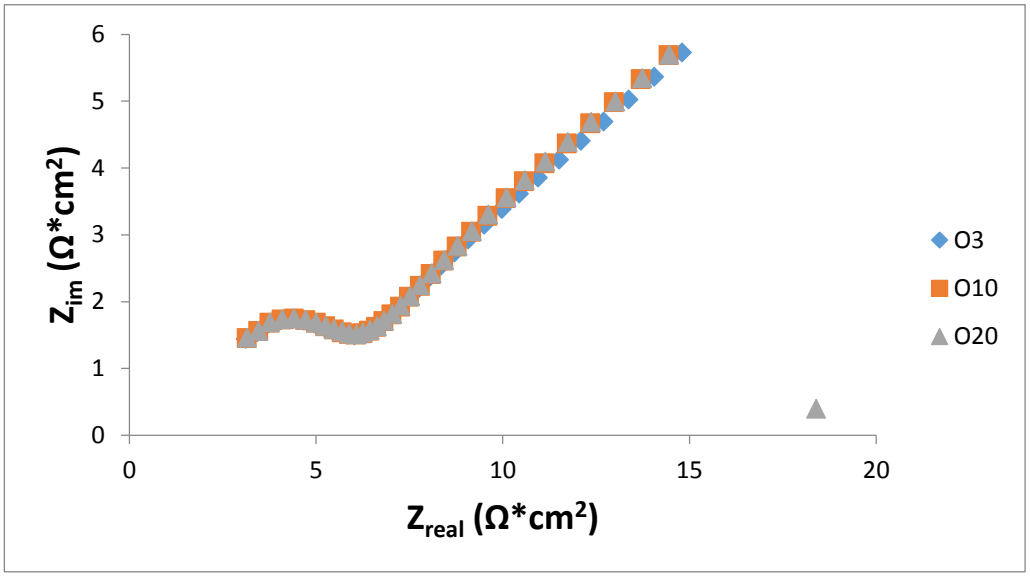

Figure 3.51. of EIS data: GDC fed with O3, O10, O20 at 600 °C.

Ohmic resistances of 1VDC at different temperatures and oxygen percentages are exhibited in Table 3.3. It is clearly seen that as the operating temperature is increased, the ohmic resistance of the compound is decreased. The ohmic resistance is decreased from 321,44 Ω*cm^2 to 4,744 Ω*cm^2 for O3; from 317,44 Ω*cm^2 to 5.28 Ω*cm^2 for O10 and from 315,64 Ω*cm^2 to 5,94 Ω*cm^2 for O20 between 400°C and 800ºC. The kinetic energy and mobility of the ions increase gradually at higher temperatures; thus, the oxide ion (O^{-2}) transport is enhanced and ionic conductivity of the compound as electrolyte is improved. The change in oxygen partial pressure does not have a significant effect on the ohmic resistance.

Table 3.3. Ohmic resistances (Ω*cm^2) of 1VDC at different temperatures and oxygen percentages.

1VDC	400°C	450°C	500°C	550°C	600°C	650°C	700°C	750°C	800°C
O3	321	233	104	46	21	16	13	6	5
O10	317	235	105	47	21	18	13	6	5
O20	316	238	105	46	21	19	13	6	6

Ohmic resistances of 2VGDC at different temperatures and oxygen percentages are demonstrated in Table 3.4. Similar to 1VDC results, as the operating temperature is increased, the ohmic resistance of the compound is decreased. The ohmic resistance is decreased from 506,4 $\Omega*cm^2$ to 39,22 $\Omega*cm^2$ for O3; from 472 $\Omega*cm^2$ to 39,908 $\Omega*cm^2$ for O10 and from 480,8 $\Omega*cm^2$ to 40,04 $\Omega*cm^2$ for O20 between 400°C and 800ºC. The ionic conductivity of the compound is enhanced as temperature is raised because the mobility of oxide ions (O^{-2}) are increased at high temperatures. The increase in oxygen partial pressure does not have much effect on the ohmic resistance. This result fits to the EIS results, oxygen partial pressure is related with the cathode surface exchange reactions, not with electrolyte properties.

Table 3.4. Ohmic resistances ($\Omega*cm^2$) of 2VGDC at different temperatures and oxygen percentages.

2VGDC	**400°C**	**450°C**	**500°C**	**550°C**	**600°C**	**650°C**	**700°C**	**750°C**	**800°C**
O3	506	506	504	490	414	305	190	142	39
O10	472	516	504	486	412	313	170	125	39
O20	480	524	504	492	411	310	175	98	40

Ohmic resistances of YSZ at different temperatures and oxygen percentages are shown in Table 3.5. With increasing operating temperature, the ohmic resistance of the compound drops gradually. The ohmic resistance is decreased from 323,88 $\Omega*cm^2$ to 1,488 $\Omega*cm^2$ for O3; from 333,92 $\Omega*cm^2$ to 1,4656 $\Omega*cm^2$ for O10 and from 331,64 $\Omega*cm^2$ to 1,4816 $\Omega*cm^2$ for O20 between 400°C and 800ºC. When the temperature is increased, the kinetic energy and mobility of the ions increase proportionally and the oxide ion (O^{-2}) transport is enhanced. Therefore, ionic conductivity of the compound and its electrolyte properties are improved. The change in oxygen partial pressure does not have a significant effect on the ohmic resistance.

Table 3.5. Ohmic resistances ($\Omega*cm^2$) of YSZ at different temperatures and oxygen percentages.

YSZ	400°C	450°C	500°C	550°C	600°C	650°C	700°C	750°C	800°C
O3	323	111	61	14	7	5	3	2	1
O10	333	131	51	14	7	5	3	2	1
O20	331	131	50	14	7	5	3	2	1

Ohmic resistances of GDC at different temperatures and oxygen percentages are exhibited in Table 3.6. As shown in the previous examples, as the operating temperature is increased, the ohmic resistance of the compound is decreased. The ohmic resistance is decreased from 41,4 $\Omega*cm^2$ to 0,7852 $\Omega*cm^2$ for O3; from 41,72 $\Omega*cm^2$ to 0,7892 $\Omega*cm^2$ for O10 and from 41,8 $\Omega*cm^2$ to 0,7948 $\Omega*cm^2$ for O20 between 400°C and 800ºC. Oxide ion (O^{-2}) transport of this compound is enhanced due the increase in kinetic energy of the molecules. The change in oxygen partial pressure does not have a significant impact on the ohmic resistance.

Table 3.6. Ohmic resistances ($\Omega*cm^2$) of GDC at different temperatures and oxygen percentages.

GDC	400°C	450°C	500°C	550°C	600°C	650°C	700°C	750°C	800°C
O3	41	17	8	4	3	2	2	1	1
O10	41	17	8	4	3	2	2	1	1
O20	41	17	8	4	3	2	2	1	1

The results of the EIS measurements of 1VDC, 2VGDC, YSZ and GDC at various temperatures and O_2 partial pressures are summarized in Table 3.7. All the compounds have a turning point temperature which means that the number of arcs are changed after a certain temperature. 3 arcs of 1VDC drops to 2 arcs at 550°C, 2 arcs of 2VGDC drops to 1 arc at 750ºC, 3 arcs of YSZ drops to 2 arcs at 750°C and finally 2 arcs of GDC drops to 1 arc at 700ºC. After the turning point, the charge transfer reactions become faster and the cell operates more efficiently.

Table 3.7. Number of EIS arcs of 1VDC, 2VGDC, YSZ and GDC at various temperatures ranging from 400°C to 800ºC.

Symm. Cell electrolytes	**Number of arcs at different temperatures with O3,O10,O20**	**Turning point temperature**	**Number of arcs after turning point temperature**
1VDC	3	550 °C	2
2VGDC	2	750 °C	1
YSZ	3	750 °C	2
GDC	2	700 °C	1

4. FUTURE WORK

Symmetric cells of 5MnGDC, 30TiGDC and GDC will be prepared and EIS tests will be done to determine their oxide (O^{-2}) permeability. It will be determined whether these materials can be used as an anode or electrolyte materials.

Anode and electrolyte supported SOFCs will be prepared with 1VDC. Pellets will be produced with this material and the powders of it will be mixed to the anode and electrolyte materials for maintaining compatibility between the electrolyte and electrode layers. The resulting materials will be dissolved in some solvents like ethylene glycol and pore formers with Carbon will be added to form a porous structure with proper fluidity called slurry. A thin layer (20-30 μm) of the slurries will be applied on the electrolyte pellets by tape casting method. The same procedure is applied for anode supported cells; anode material will be used as pellet and electrolyte and cathode slurries will be applied by tape casting method.

Anode, electrolyte materials based on Cerium oxide and cathode materials that are selected from the analysis, will be used to produce a novel SOFC and the performance tests as well as EIS tests will be done with hydrogen gas and carbon containing fuels ($CO/H_2/CO_2/H_2O$ mixture, CH_4, C_3H_8 ve C_4H_{10}) at different temperatures in intermediate temperature range. In addition, the system will be analyzed with a Raman spectrometer with 532 nm laser while the cell is operated, as a result, the intermediate products formed on anode and cathode and degredation processes at these conditions can be observed.

Lastly, computational modelling of SOFC performance tests will be done starting with the conventional SOFC (Ni-YSZ anode, YSZ electrolyte, LSM-YSZ cathode). EIS tests will be modelled to investigate the effects of reactions at different steps on the performance of the cell by using computer software. The computational data and experimental results will be compared to evaluate the parameters that effect the cell performance and a SOFC with better performance will be obtained.

5. CONCLUSIONS

This study consists of mainly two experimental methods: First one is developing a new electrolyte material by doping Manganese, Vanadium and Titanium to GDC and also by doping Vanadium to Ceria. The electrical and ionic conductivites of these materials are investigated to determine their suitability as an electrolyte material. The second part of the study is impregnation of Vanadium and Manganese metals on the anode side of commercial cells which is composed of Ni-YSZ anode, YSZ electrolyte and LSM cathode. The electrochemical performances of the impregnated cells operating at 800ºC are evaluated.

The synthesis of new electrolyte materials are done with sol-gel method with different proportions of the dopant and sintered at 900 ºC. XRD data of the products is analyzed and the ideal proportion of metal doping for each compound is determined. Next, Raman spectrum of these compounds is analyzed with 532 nm laser and in the future these data will be compared with the Raman in-situ experiments at high temperatures. It is known that an ideal electrolyte should have low electrical conductivity but high ionic conductivity. Hence, these properties are investigated for the selected materials together with GDC and YSZ which are conventional electrolyte materials. The electrical conductivity of these materials is determined by Four Probe measurements. Chronopotentiometry technique is used to determine the electrical conductivity and by using Arrhenius equation, activation energy of each compound is determined. 1VDC and 2VGDC have low electrical conductivity according to these data so ionic conductivity tests are performed for these two compounds with conventional electrolyte materials, YSZ and GDC. Symmetric cells are prepared with 0,3 mm thickness and 5 mm diameter, then EIS tests are conducted with different O_2 partial pressures (%3, %10, %20 proportions of O_2 in the feed) at intermediate temperature range. The change in polarization and ohmic resistances at different conditions are observed.

Another experiment is the study of Vanadium and Manganese impregnated commercial cells. XRD data the impregnated cells is obtained and EIS, LSV tests are carried out at 800 ºC. In the end, power density graphs are plotted and the performance results of the impregnated cells are compared with Ni-YSZ anode commercial cells.

The results of sol-gel synthesis are that doping %5 Manganese (5MnGDC), %30 Titanium (30TiGDC) and %2 Vanadium (2VGDC) to GDC is an ideal composition for this compound because at different proportions, phase seperation occurs which can be observed on XRD graphs. Ceria doped with %1 Vanadium (1VDC) has no phase seperation either so it is selected as a potential electrolyte material. In Raman spectrum, Ceria gives signal at 464 cm^{-1} and this value changes slightly when Ceria is doped with other metals. No other phase separation is observed in Raman graphs. After characterization of the materials, Four Probe measurements are performed and the chronopotentiometry results show that the voltage values decrease with increasing temperature at constant current due to the lower electrical conductivity resistances of the materials at high temperatures. Arrhenius plot is obtained from these results and it is found out that the electrical conductivity of the materials increases in the following order: 1VDC, 2VGDC, YSZ, 30TiGDC, 5MnGDC, YSZ and GDC. 1VDC and 2VGDC have the lowest electrical conductivity according to Arrhenius plot and activation energies so they are potential electrolyte candidates. In addition, doping different metals to GDC has dropped its electrical conductivity, which is a desired result for this study. Ionic conductivity experiments are done with symmetric cells 1VDC, 2VGDC, YSZ, GDC as electrolyte and LSM as cathode. According to EIS results, 3 arcs appear at low temperatures for 1VDC and YSZ whereas 2 arcs are observed for 2VGDC and GDC. In general, first arc on the left side of the graph corresponds to charge transfer reactions, second arc is about oxide ion transport mechanism and third arc is related to oxygen diffusion and surface exchange reactions on cathode side. In other words, at high frequency region, electrolyte properties and reactions that occur during oxide ion (O^{-2}) transport can be observed, at low frequency region oxygen mass transport on the surface of cathode can be detected.

Firstly, the temperature dependence of ohmic and polarization resistances are evaluated. Some arcs at high frequency region disappear as temperature is increased. Each

compound has a turning point temperature where the first arc cannot be distinguished from the second arc. This is due to the increase of the rate of the reactions in the system at high temperatures. 1VDC has a turning point at 550°C, 2VGDC at 750ºC, YSZ at 750°C and GDC at 700ºC. At these temperatures the polarization resistance of the systems drop and the electrolyte works more efficiently. In addition, ohmic resistance (bulk resistance) drops dramatically for each compound at different temperatures. 1VDC has this drop at 550°C, 2VGDC at 700°C, YSZ at 550°C, GDC at 450°C. As a result, 1VDC works best at 550°C and can be used as an electrolyte at this temperature. 2VGDC is activated at 700°C according to the results, thus, it doesn't conduct enough oxide ion (O^{-2}) at intermediate temperature range. YSZ is active for oxide (O^{-2}) ion transport between 550°C and 750°C which correlates with the literature results. According to the results, GDC is active between 450°C and 700°C which is also an expected result.

Oxygen shifts at intermediate temperatures mainly affect the arc at low frequency region, which is only related to cathode properties. 1VDC has larger low frequency arc at low oxygen percentage below 550°C; the low frequency arc becomes smaller as temperature is raised. This is a result of oxygen diffusion resistance drop at high temperatures. For the other compounds, this phenomenon is not very obvious and the low frequency arc does not change when oxygen partial pressure is altered.

The results of Manganese and Vanadium impregnation on conventional cells can be summarized with the following statements: The addition of Vanadium to the anode side of the Ni-YSZ anode cell increases the maximum power density of the cell from 55mW/cm^2 to 68mW/cm^2. This proves that Vanadium enhances the cell efficiency about % 25. Similar process is applied Manganese impregnated cell. The maximum power densities of Ni-YSZ anode cell and Manganese impregnated cell are compared. An increase from 73mW/cm^2 to 179mW/cm^2 is observed after impregnation process. Manganese increases the cell efficiency about % 145, which is a significant improvement in the cell performance. The oxide ions (O^{-2}) are bonded to Manganese easier than Nickel and impregnation increases electrical conductivity of anode. In addition, it may be possible to solve carbon deposition problem for Nickel by impregnating Manganese to the Ni-YSZ anode.

REFERENCES

1. Atkins, P., J. Paula, *Physical Chemistry*, Seventh edition ed. 2002: Oxford University Press.

2. Hoogers G., *Fuel Cell Technology Handbook*, Crc Press, New York 2002.

3. O'Hayre R., S. Cha, W. Colella, F. B. Prinz, *Fuel Cell Fundamentals*, John Wiley & Sons,Inc., New York, NY,USA, 2006.

4. Mench, M. M., C. Y. Wang, S. T. Thynell, "An introduction to fuel cells and related transport phenomena", *International Journal of Transport Phenomena*, Vol. 3, pp 151-176, 2001.

5. Fabbri, E., D. Pergolesi, E. Traversa, "Electrode materials: a challenge for the exploitation of protonic solid oxide fuel cells", *Science and Technology of Advanced Materials*, 11, pp 44301-44309, 2010.

6. Lee, T. S., J.N. Chung, Y. C. Chen, "Design and optimization of a combined fuel reforming and solid oxide fuel", *Energy Conversion and Managment*, Vol. 52, pp 3214-3226, 2011.

7. Song, C., "Fuel processing for low-temperature and high-temperature fuel cells Challenges, and opportunities for sustainable development in the 21st century", *Catalysis Today*, Vol. 77, pp 17-49, 2002.

8. McIntosh, S., J.M. Vohs, and R.J. Gorte, "Role of hydrocarbon deposits in the enhanced performance of direct-oxidation SOFCs", *Journal Of The Electrochemical Society*, Vol. 150, pp A470-A476, 2003.

9. Haile, S., "Fuel cell materials and components", *Acta Materialia*, Vol. 51, pp 5981-6000, 2003.

10. Steele, B.C.H., “Materials for IT-SOFC stacks: 35 years R&D: the inevitability of gradualness?” , *Solid State Ionics*, Vol. 134, pp 3-20, 2000.

11. Singhal, S.C., “Advances in solid oxide fuel cell technology”, *Solid State Ionics*, Vol. 135, pp 305-313, 2000.

12. Singh, T., A. Kumar, “Fuel Cell Market: A Review”, *International Journal of Engineering Research*, Volume No.2, pp : 152-155, 2013.

13. H.P., J.M. Hill, “Carbon deposition on Ni/YSZ composites exposed to humidified methane.” *Applied Catalysis A-General*, Vol. 317, pp 284-292, 2007.

14. Costa-Nunes, O., R.J. Gorte, and J.M. Vohs, “Comparison of the performance of Cu-CeO2-YSZ and Ni-YSZ composite SOFC anodes with H-2, CO, and syngas”, *Journal Of Power Sources*, Vol. 141, pp 241-249, 2005.

15. Hua, B., W. Zhang, M. Li, X. Wang, B. Chi, J. Pu, J. Li, “Improved microstructure and performance of Ni-based anode for intermediate temperature solid oxide fuel cells”, *Journal of Power Sources*, 247, pp 170–177, 2014.

16. Zha, S., Z. Cheng, M. Liu, “Sulfur Poisoning and Regeneration of Ni-Based Anodes in Solid Oxide Fuel Cells”, *Journal of The Electrochemical Society*, Vol. 154, pp 201-206, 2007.

17. Cheng, J., Q. Jiang, H. He, J. Yang, Y. Wang, J. Gao, “Preparation and characterization of Y2O3–Sm2O3 co-doped ceria electrolyte for IT-SOFCs”, *Materials Chemistry and Physics*, Vol. 125, 2011.

18. Steele, B.C.H., "Appraisal of Ce_{1-y} Gd_y $O_{2-y/2}$ electrolytes for IT-SOFC operation at 500^{o}C", *Solid State Ionics*, Vol.129, pp 95–110, 2000.

19. Mogensen, M., N.M. Sammes,G.A.Tompsett, "Physical, chemical and electrochemical properties of pure and doped ceria", SolidStateIonics, Vol. 129, pp 63-94, 2000.

20. Lin, Y.B., S.A. Barnett, "Co-firing of anode-supported SOFCs with thin $La_{0.9}Sr_{0.1}Ga_{0.8}Mg_{0.2}O_3$-delta electrolytes*", Electrochemical And Solid State Letters*, Vol. 9, pp 285-288, 2006.

21. Yang, R. J., M. C. Lee, J. C. Chang, T. N. Lin, Y. C. Chang, W. X. Kao, L. S. Lee, S. W. Cheng, "Fabrication and characterization of a $Sm_{0.2}Ce_{0.8}O_{1.9}$ electrolyte film by the spin-coating method for a low-temperature anode-supported solid oxide fuel cells", *Journal of Power Sources*, 206, pp 111-118, 2012.

22. Lashtabeg, A., S.J.Skinner, "Solid oxide fuel cells—a challenge for materials chemists?", *Journal of Materials Chemistry*, Vol. 16, pp 3161-3170, 2006.

23. Lu, J.B., Z.T. Zhang, and Z.L. Tang, "Review on the development of solid oxide fuel cells" *Rare Metal Materials And Engineering*, Vol. 34, pp 1177-1180, 2005.

24. Tsipis, E.V., V.V. Kharton, "Electrode materials and reaction mechanisms in solid oxide fuel cells: a brief review. III. Recent trends and selected methodological aspects", *Solid State Electrochem*, Vol. 15, pp 1007-1040, 2011.

25. Zha, S.W., "GDC-based low-temperature SOFCs powered by hydrocarbon fuels", *Journal Of The Electrochemical Society*, Vol. 151, pp 1128-1133, 2004.

26. Kaur, G., S. Basu, "Performance studies of coppereiron/ceriaeyttria stabilized zirconia anode for electro-oxidation of butane in solid oxide fuel cells", *Journal of Power Sources* , Vol.241, pp 783-790, 2013.

27. Kim, H., C. Lu, WL Worrell, JM Vohs, RJ Gorte, “Cu-Ni cermet anodes for direct oxidation of methane in solid-oxide fuel cells”, *Journal of the Electrochemical Society*, Vol.149, pp 247-250, 2002.

28. Kim, H., C. Lu, WL Worrell, JM Vohs, RJ Gorte, “Cu-Ni cermet anodes for direct oxidation of methane in solid-oxide fuel cells”, *Journal of the Electrochemical Society*, Vol.149, pp 247-250, 2002.

29. Kaur, G., S. Basu, “Study of Carbon Deposition Behavior on Cu–Co/CeO_2–YSZ Anodes for Direct Butane Solid Oxide Fuel Cells”, *Fuel Cells*, Vol. 10, pp 1-8, 2014.

30. Lay, E., G. Gauthier, S. R. Cristian, S. J. T.S. Irvine, “Ce-substituted LSCM as new anode material for SOFC operating in dry methane”, Vol. 179, pp 1562-1566, 2008.

31. Maguire, E., B. Gharbage, F.M.B Marques, J.A Labrincha, “Cathode materials for intermediate temperature SOFCs”, *Solid State Ionics*, Vol. 127, pp 329-335, 2000

32. Jørgensen , M.J., S. Primdahl, C. Bagger, M. Mogensen, “Effect of sintering temperature on microstructure and performance of LSM–YSZ composite cathodes”, *Solid State Ionics*, Vol. 139, pp 1-11, 2001.

33. Sun, C., R. Hui, J. Roller “ Cathode materials for solid oxide fuel cells: a review”, *Solid State Electrochem* , Vol. 14, pp 1125-1144, 2010.

34. Xia, C., W. Rauch, F. Chen, M. Liu, "$Sm_{0.5}$ $Sr_{0.5}CoO_3$ cathodes for low-temperature SOFCs", *Solid State Ionics*, Vol. 149, pp 11-19, 2002.

35. Sun, X., S. Li, J. Sun, X. Liu, B. Zhu, "Electrochemical performances of BSCF cathode materials for ceria-composite electrolyte low temperature solid oxide fuel cells", *International Journal of Electrochemical Science*, Vol. 2, pp 462 – 468, 2007.

36. Liu, Q. L., K. A. Khor, S. H. Chan, "Short communication High-performance low-temperature solid oxide fuel cell with novel BSCF cathode", *Journal of Power Sources*, 161, pp 123-128, 2006.

37. Park, S., S. Choi, J. Schin, G. Kim, "Electrochemical investigation of strontium doping effect on high performance Pr1−xSrxCoO3−ı (x = 0.1, 0.3, 0.5, and 0.7) cathode for intermediate-temperature solid oxide fuel cells" , *Journal of Power Source*, Vol. 210, pp 172-177, 2012.

38. Wana, Y., W. Zhaoa, Y. Tanga, L. Li, H. Wanga, Y. Cui, "Ni-Mn bi-metal oxide catalysts for the low temperature SCR removal of NO with NH_3, *Applied Catalysis B: Environmental*, Vol. 148-149, pp 114-122, 2014.

39. Fraccari, E.P., O. D'Alessandro, J. Sambeth, G. Baronetti, F. Mariño, "Ce–Mn mixed oxides as supports of copper- and nickel-based catalysts for water–gas shift reaction", *Fuel Processing Technology*, Vol. 119, pp 67-73, 2014.

40. Zhang, F., Chan, S., J.E. Spanier, E. Apak, Q. Jin, R. Robinson, I. P. Herman "Cerium oxide nanoparticles: Size-selective formation and structure analysis" , *Applied Physics Letters*, Vol. 80, pp 127-129, 2002.

41. Maher, R.C., L.F. Cohen, P. Lohsoontorn, D. J. L. Brett, and N. P. Brandon, "Raman Spectroscopy as a Probe of Temperature and Oxidation State for

Gadolinium-Doped Ceria Used in Solid Oxide Fuel Cells", *Journal of Physical Chemistry*, Vol. 112, pp 1497-1501, 2008.

42. Lughi, V., D. R. Clarke, "Temperature Dependence of the Yttria-Stabilized Zirconia Raman Spectrum", *Journal of Applied Physics,* Vol. 101, pp 50-56, 2007.

43. Cai, J., C. Raptis, Y.S. Raptis, E. Anastassakis, "Temperature dependence of Raman scattering in stabilized cubic zirconia", "Physical Review B", Vol.51, pp 201-209, 1995.

44. Istomin, S.Y., E.V. Antipov, "Cathode materials based on perovskite-like transition metal oxides for intermediate temperature solid oxide fuel cells", *Russian Chemical Reviews*, Vol. 82, pp 686-700, 2013.

45. Cao, X., G., S. P. Jiang, "Identification of oxygen reduction processes at (La,Sr)MnO3 electrode/La9.5Si6O26.25 apatite electrolyte interface of solid oxide fuel cells", *International Journal of Hydrogen Energy,* Vol. 38, pp 2421-2431, 2013.

46. Hjelm, J., M. Søgaard, M. Wandel, M. Menon, M. Mogensen, and A. Hagen, " Electrochemical Impedance Studies of SOFC Cathodes", *ECS Transactions,* Vol. 7, pp 1261-1270, 2007.

47. Adler, S.B., "Factors Governing Oxygen Reduction in Solid Oxide Fuel Cell Cathodes", *Chem. Reviews*, Vol. 104, pp 4791-4843, 2004.

48. Mauvy, F., C. Lalanne, J.M. Bassat , J.C. Grenier , H. Zhao, P. Dordor, Ph. Stevens, "Oxygen reduction on porous Ln2NiO4+δ electrodes", *Journal of the European Ceramic Society,* Vol. 25, pp 2669–2672, 2005.

49. Kim, J.D., G.D. Kim, J.W. Moon, Y. Park, W.H. Lee, K. Kobayashi, M. Nagai, C.E. Kim, “Characterization of LSM–YSZ composite electrode by ac impedance spectroscopy”, *Solid State Ionics,* Vol. 143, pp 379–389, 2001.

50. Liu, J., W. Liu, Z. Lu, L. Pei, L. Jia, L. He, W. Su, “Study on the properties of YSZ electrolyte made by plaster casting method and the applications in solid oxide fuel cells”, *Solid State Ionics,* Vol. 118, pp 67–72, 1999.

51. Kim, J.D., G.D. Kim, J.W. Moon, Y. Park, W.H. Lee, K. Kobayashi, M. Nagai, C.E. Kim, “Characterization of LSM–YSZ composite electrode by ac impedance spectroscopy”, *Solid State Ionics,* Vol. 143, pp 379–389, 2001.

52. Escudero, M.J., A. Aguadero, J.A. Alonso, L. Daza, “A kinetic study of oxygen reduction reaction on La2NiO4 cathodes by means of impedance spectroscopy”, *Journal of Electroanalytical Chemistry,* Vol. 611, pp 107–116, 2007.

53. Fleig, J., H.R. Kim, J. Jamnik, J. Maier, “Oxygen Reduction Kinetics of Lanthanum Manganite (LSM) Model Cathodes: Partial Pressure Dependence and Rate-Limiting Steps”, *Fuel Cells,* Vol. 5, pp 330-337, 2008.

54. Mauvy, F., J.-M. Bassat, E. Boehm, J.-P. Manaud, P. Dordor, J.-C. Grenier, “Oxygen electrode reaction on Nd2NiO4+y cathode materials: impedance spectroscopy study”, *Solid State Ionics,* Vol. 158, pp 17– 28, 2003.